Department of Precision and Microsystems Engineering

Topology Optimization for Manufacturable Thermoelastic Metamaterials

M.J.F. van den Ouden

Report no : 2021.026
Coach : Ir. S. Koppen
Professor : Dr. ir. M. Langelaar
Specialisation : Structural Optimization and Mechanics (SOM)
Type of report : Master thesis
Date : April 14, 2021

TU Delft Delft University of Technology

Challenge the future

Topology Optimization for Manufacturable Thermoelastic Metamaterials

Master of Science Thesis

For the degree of Master of Science in Mechanical Engineering at Delft University of Technology

M.J.F. van den Ouden

April 14, 2021

Student number:	4351940	
Thesis committee:	Dr. ir. M. Langelaar	TU Delft, supervisor
	Ir. S. Koppen	TU Delft, supervisor
	Dr. ir. M. Tichem	TU Delft
	Dr. ir. C. Zonnevylle	RAITH Group

Acknowledgements

The thesis presented to you is the final work for the completion of my Master's Degree in Mechanical Engineering at Delft University of Technology, which is the result of over a year of tackling numerous challenges, perseverance and excellent guidance. A paper has been written in cooperation with Dr. ir. Matthijs Langelaar and Ir. Stijn Koppen based on this thesis project, titled "Topology Optimization for Manufacturable Thermoelastic Metamaterials with Tailored Unidirectional Thermal Expansion", which will be submitted to the *11th Int. Conference on Coupled Problems in Science and Engineering (COUPLED 2021)*.

I would like to express my gratitude towards my supervisors, Matthijs Langelaar and Stijn Koppen, for their dedication to the project, explanations on challenging topics and their useful remarks and suggestions, which have been a tremendous help throughout this thesis project. Furthermore, I would like to thank Jo Spronck, who helped me with the many challenges I faced during the experimental work through his helpfulness and expertise.

Last but not least, I would like to thank Roos, my parents, family and friends for their unconditional support and welcome distraction during this period.

Delft, University of Technology
April 14, 2021

M.J.F. van den Ouden

Table of Contents

TO	Topology Optimization
AM	Additive Manufacturing
DED	Direct Energy Deposition
UAM	Ultrasonic Additive Manufacturing
DOFs	Degrees of Freedom
BC	Boundary Condition
CTE	Coefficient of Thermal Expansion
NTE	Negative Thermal Expansion
PTE	Positive Thermal Expansion
ZTE	Zero Thermal Expansion
DMD	Direct Metal Deposition
CNC	Computer Nummerical Control
WEDM	Wire Electronic Discharge Machining
FE	Finite Element
FEM	Finite Element Method
MMA	Method of Moving Asymptotes
FIB	Focused Ion Beam
FEA	Finite Element Analysis
FEAs	Finite Element Analyses
MSE	Mean Square Error

Abstract

The concept of thermoelastic metamaterials has been around for over two decades and their possible applications, in which extremely positive, zero and negative thermal expansion is desired, are plentiful. Nevertheless they are rarely applied, due to their poor manufacturability. Recent developments in multi-material additive manufacturing are however promising. To enhance their applicability, a topology optimization framework is proposed and verified, able to generate manufacturable thermoelastic metamaterials with tailored unidirectional thermal expansion, manufacturable through automated multi-material additive manufacturing methods.

The superelement method is utilized to optimize for thermoelastic metamaterials of finite size, connected to solid strips allowing easy mounting. Opposed to the commonly used homogenization method, a clear separation between of macro- and microscopic length scales is not required. The robust formulation is used combined with a filter domain extension approach, to obtain manufacturing tolerant, black and white solutions and minimum length scale control. Uniform material layers are enforced in the design, such that fabrication using ultrasonic additive manufacturing is possible.

Numerical validation highlights the advantage of the superelement method, for the optimization of small thermoelastic metamaterial unit cell arrays, compared to the commonly used homogenization method. A 3D finite element analysis of the post-processed design furthermore shows that a thermoelastic metamaterial design is obtained, with a unidirectional thermal expansion significantly lower than that of its constituents.

A sample has been fabricated using a low-tech production process, inspired by a multi-material ultrasonic additive manufacturing process, with a unidirectional thermal expansion of $(-4 \pm 8)\,\mu\text{m}/(\text{m}^\circ\text{C})$. With this sample, the numerical predictions have been validated experimentally, confirming the capability of the proposed design approach to generate performant and realizable thermoelastic metamaterials.

Chapter 1

Introduction

1-1 Motivation

1-1-1 Background

Until recently, materials available to engineers had merely conventional properties known from nature. The introduction of metamaterials allows for materials with tailored unconventional properties, enabling engineers to generate innovative and efficient designs utilizing these tailored material properties. Opposed to conventional materials, metamaterials attain their physical properties not primarily from the intrinsic properties of their constituents, but rather from their internal, specific structures [1]. Metamaterials can be generated by patterning a characteristic unit cell periodically in space [2]. The material properties of metamaterials can thus be controlled by geometries at multiple length scales and not only by the chemical composition of the conventional materials used [3]. This allows for the design of novel materials with unconventional and extreme material properties. Unconventional properties such as negative Poisson's ratio [4], negative thermal expansion [5] and negative stiffness [6] can be achieved by using metamaterials. Additionally, metamaterials allow for ultra-light, high stiffness and high strength materials [7, 8]. Examples of metamaterials are presented in Figure 1-1.

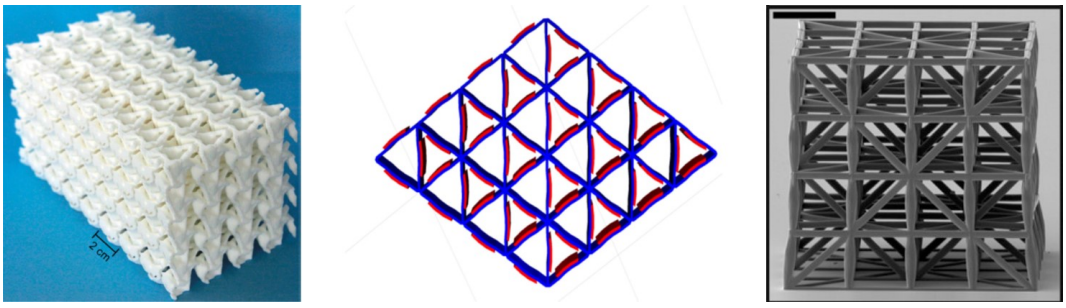

Figure 1-1: Examples of metamaterials from literature for negative Poisson's ratio [9], tuneable thermal expansion [10] and high strength [8], respectively.

The focus of this thesis will be on thermoelastic metamaterials with a tailored Coefficient of Thermal Expansion (CTE). These metamaterials are typically composed of multiple conventional materials with different but positive CTE and locations without material. Upon heating, the difference in CTE of the used materials causes deformation of the metamaterial structure utilizing the voids. This allows thermoelastic metamaterials to exhibit a tailored CTE, different to the CTE of the conventional materials used in its structure.

1-1-2 Applications

Thermoelastic metamaterials with tailored CTE can be used for numerous applications. Metamaterials with large Positive Thermal Expansion (PTE) can for example be used as thermal actuators [5] and Negative Thermal Expansion (NTE) metamaterials can be used in high precision devices to cancel thermal expansion [11]. Furthermore, thin films with large PTE and NTE can be combined to obtain sensitive temperature sensors [12]. In this thesis we will focus on metamaterials with Zero Thermal Expansion (ZTE), which have numerous applications as well. These metamaterials can be used in structures that are subjected to large temperature changes such as bridges, which might be subjected to big structural changes due to temperature changes between day, night, summer and winter [5]. Furthermore, ZTE metamaterials are useful in engineering applications were high precision and stability under varying thermal conditions is to be achieved, such as in optical components, precision instruments and nanofabrication systems which include Focused Ion Beam (FIB) systems [13]. An example of a thermoelastic metamaterial is given in Figure 1-2, which has near ZTE in vertical direction.

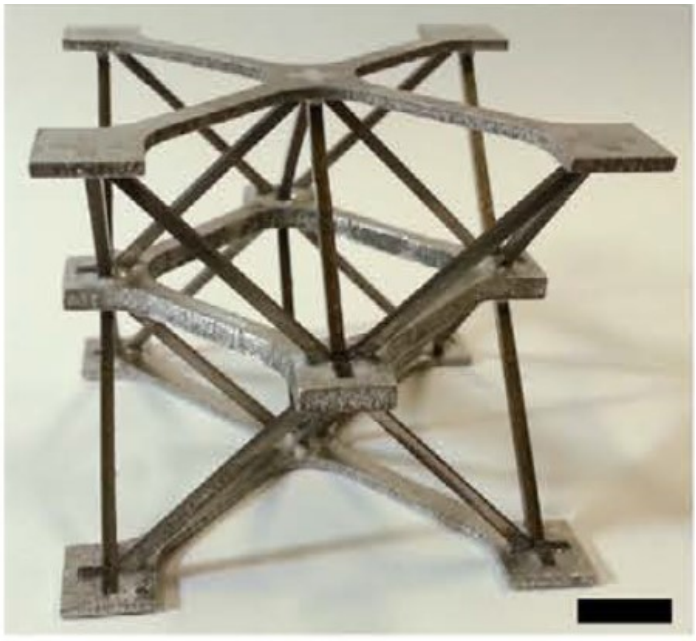

Figure 1-2: Example of a manufactured thermoelastic metamaterial structure with unidirectional near ZTE, composed of aluminium and titanium [14].

1-1-3 Scope for improvement

Metamaterials thus have a great potential for engineering applications. Unfortunately, the design and especially the fabrication of metamaterials remains difficult [15]. Fabrication of thermoelastic metamaterials is especially challenging, since this requires the use of multiple materials within a single metamaterial structure. To facilitate their application, an efficient design methodology for metamaterials is thus necessary, which allows for optimized thermoelastic metamaterial designs with tailored CTE, that satisfy manufacturing restrictions imposed by suitable manufacturing techniques. Although multi-material Additive Manufacturing (AM) is still in an early stage of development and faces many technical challenges, it potentially allows the production of virtually all metamaterial structures [15]. Furthermore, Topology Optimization (TO), a versatile computational design method to generate functional structures, could achieve the generation of optimized new metamaterial structures [16] and already is capable of incorporating certain limitations imposed by AM [17]. This research is aimed at the development of a design methodology utilizing TO, which is able to generate optimized thermoelastic metamaterials for a tailored CTE, that are manufacturable through suitable AM techniques without extensive post-processing of the optimized design.

The scope of this thesis is limited to thermoelastic metamaterials subjected to a uniform temperature distribution and with periodically repeated unit cells. Design cases will be studied specifically for thermoelastic metamaterials applicable to nanofabrication systems, in which ZTE materials can be used to ensure sufficient precision and stability. Therefore thermoelastic metamaterial designs will be generated for ZTE. Metallic constituents of the metamaterial are required, since they are thermally and electrically conductive, which helps in avoiding heat build-up in the metamaterial and furthermore prevents build-up of static charge. Nanofabrication systems, more specifically FIB systems, namely use ion beams to manufacture the desired product. Build-up of static charge can therefore occur in these machines if non-conductive materials are used, resulting in undesired events such as the origination of sparks. Note that the design methodology presented in this thesis is however very general and can be used for the design of thermoelastic metamaterials with any specific CTE. Furthermore, the design methodology does not require the constituents of the thermoelastic metamaterial to be metallic.

1-1-4 Chapter outline

First, Section 1-2 discusses synthesis methods, thermoelastic properties, the state-of-the-art and manufacturing techniques of thermoelastic metamaterials. Then, in Section 1-3, a literature gap is presented and the scope of this research is given. Finally, Section 1-4 presents the outline of this thesis.

1-2 Thermoelastic metamaterials

1-2-1 Working principle

The microstructure of three-phase composites can be designed such, that the effective CTE of the composite is smaller or larger than the CTE of the constituents used in the composite. This is done by combining a low CTE material phase, high CTE material phase and voids in the microstructural design of the composite [18]. The difference in the CTE of the material phases causes deformation of the microstructure when subjected to temperature changes. The voids introduced in the microstructure provide empty space, utilized for the deformation of the microstructure.

The microstructural design presented in Figure 1-2 for example consists of a specific configuration of triangles, which have one member with a higher CTE than the other two members. The difference in the CTE of the members results in the deformation of the triangular shape when subjected to heat. When heated, the angle between the members changes, causing the triangle to contract along a line perpendicular to the high CTE member, intersecting the joint between the two low CTE members. Therefore, the thermal expansion of the composite presented in Figure 1-2 in the vertical direction is smaller, than the thermal expansion of the two material phases used in the composite. The same working principle applies to composites with microstructures designed for isotropic extreme thermal expansion.

1-2-2 Synthesis methods

Overview

For thermoelastic metamaterials, the working principle is based on the deformation of members of its microstructural architecture due to temperature changes and certainly not exclusively on the relative motion between rigid links and joints. Therefore, thermoelastic metamaterials belong to a class of compliant mechanisms. An overview of the design approaches for metamaterials including thermoelastic metamaterials edited from Blokland [19], which is based on Gallego and Herder [20], is given in Figure 1-3.

Kinematics-based approaches focus on desired motion to generate designs. A rigid body mechanism satisfying the desired kinematics can be converted to a compliant mechanism or a compliant mechanism can be generated by identifying the desired motion and finding flexure topologies from a library that constrain the remaining motion. Alternatively, building block approaches combine multiple compliant mechanisms performing simple functions, to create compliant mechanisms able to perform more complex functions. Finally, structural optimization approaches such as size, shape or topology optimization can be used to design metamaterials for a given objective function satisfying imposed constraints. In size optimization, given a certain topology and shape, size variables are optimized. Shape optimization optimizes the contour or surface and in TO the topology, defined as the connectivity of small elements describing an object, is additionally optimized. Structural optimization can be used to design metamaterials with optimal performance. TO is the most powerful structural optimization method, since the design space bounding the optimal solution is large compared to size and shape optimization.

Conclusions

TO is identified to be the most promising synthesis method for thermoelastic metamaterials. Using TO optimal performance can be established and in comparison with other synthesis methods, including shape and size optimization, the design freedom obtained with TO is very large. Using TO thermoelastic metamaterials can furthermore be designed for certain specific functionalities, such as a specific desired CTE or a minimum bulk modulus, by changing the objective function or constraints used for the optimization. Additionally, TO is very suitable for the implementation of manufacturing constraints on the design, as shown for example in Langelaar [17], without drastically decreasing the design space.

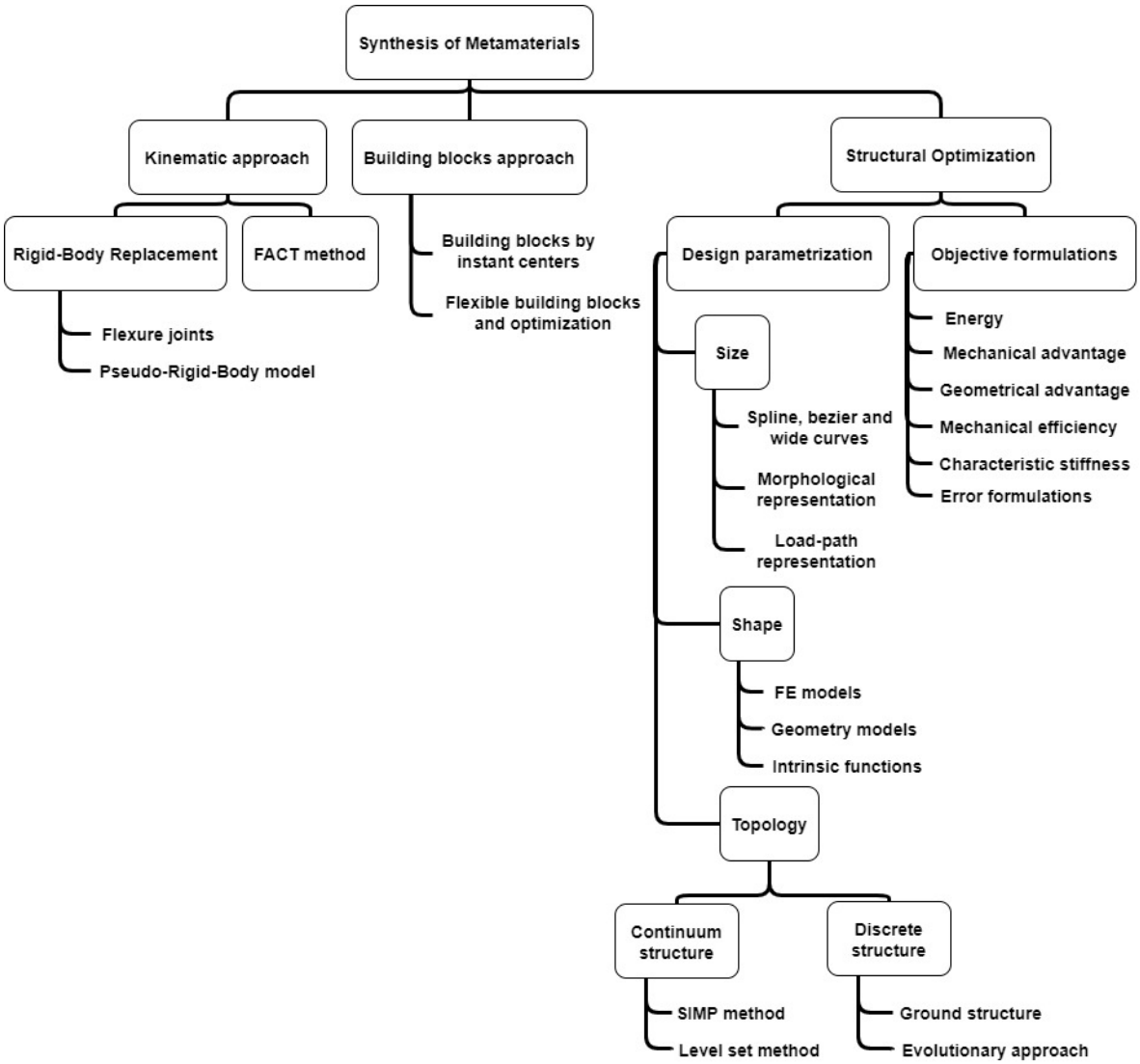

Figure 1-3: Overview of synthesis methods for metamaterials edited from Blokland [19] based on Gallego and Herder [20].

1-2-3 Bounds on Thermoelastic Properties

Stiffness is an important consideration for materials, including metamaterials, used in many practical engineering applications. Therefore, the stiffness of thermoelastic metamaterials is often maximized, whilst satisfying a tailored CTE. The achievable stiffness for a given CTE is however bounded. Schapery [21] and Rosen and Hashin [22] found bounds for isotropic three-phase materials on the thermal expansion coefficient in terms of the stiffness tensor. These bounds were later updated by Gibiansky and Torquato [23] based on the results of Sigmund and Torquato [5]. As has been shown by Watts and Tortorelli [24], these bounds are also valid in 3D. A visualization of the bounds for a specific design case is given in Figure 1-4. It can be seen that the maximum effective bulk modulus for the presented design case is only 25% of the bulk modulus for the solid material phase 1. Furthermore, it can be seen that more extreme effective thermal expansion coefficients, result in lower effective bulk moduli.

As later elaborated in Chapter 3, anisotropic three-phase thermoelastic metamaterial will be optimized in the current work, for which these bounds are not valid. Nevertheless, the trade-off between the thermal expansion coefficients and the stiffness for three-phase thermoelastic metamaterials remains. In the optimization formulation, it should therefore be addressed that the achievable maximum stiffness is limited by the required effective CTE.

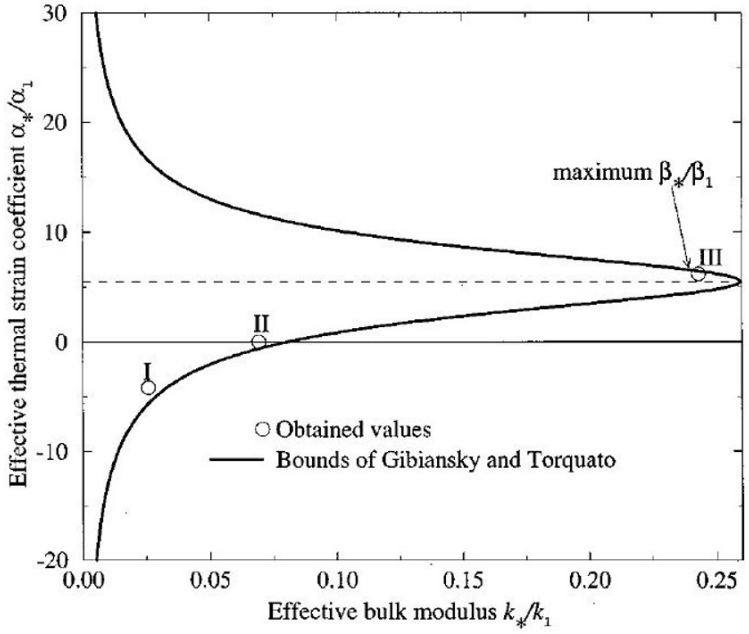

Figure 1-4: Normalized thermoelastic bounds for the effective thermal strain coefficient on the effective bulk modulus for an isotropic three-phase composite design example. Bounds are formulated by Gibiansky and Torquato [23] based on optimized thermoelastic metamaterials obtained using TO, indicated with I, II and III. For optimization case III, the normalized isotropic thermal stress coefficient (β_*/β_1) is optimized. The material properties for the solid material phases used for the TO are $E_1/E_2 = 1$, $\nu_1 = \nu_2 = 0.3$ and $\alpha_1/\alpha_2 = 10$. Volume fractions of 0.25 are enforced on the solid phases. Normalization is performed with respect to solid phase 1. [25]

1-2-4 State-of-the-art

Overview

Since the introduction of lattice structures with extreme CTE by Lakes [18], there has been extensive research into designs of metamaterials for NTE, ZTE and extreme PTE. Thermoelastic metamaterials have been designed both with [11, 24–31] and without [10, 14, 18, 31–69] TO. As discussed earlier, TO is identified to be the most powerful tool for the design of thermoelastic metamaterials, since it can utilize a large design space and allows the optimization of thermoelastic metamaterials with a specific CTE and maximized stiffness. The large design space utilized by TO also has a drawback, since optimized designs might not be manufacturable. In this section we will discuss thermoelastic metamaterial designs generated using TO. We will discuss if and how manufacturability of the design is obtained. Furthermore, the validation of the designs will be discussed.

Sigmund and Torquato [25] were the first to design planar periodic thermoelastic metamaterials using TO. The effective material properties of the thermoelastic metamaterial were computed using the homogenization theory [70, 71], that assumes an infinite repetition of the unit cells. In Figure 1-5, two design interpretations are visualized designed for NTE and ZTE. Sigmund and Torquato [25] did not include manufacturability considerations in the optimization. They state that the obtained designs may be manufacturable. The designs are however not manufactured and have not been verified numerically or experimentally.

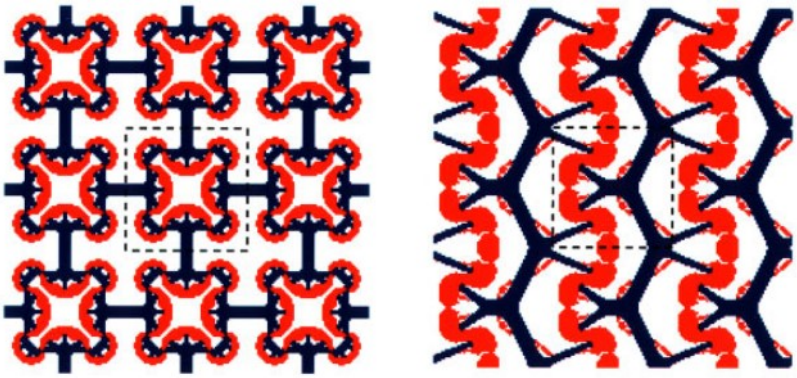

Figure 1-5: Optimal microstructures composed of hypothetical phases designed by Sigmund and Torquato [25] (red is high expansion phase, blue is low expansion phase and white is void). Left: Minimization of thermal expansion; Right: Maximization of stiffness for ZTE. [25]

Chen et al. [26] performed a similar research and designed thermoelastic metamaterials for a specific CTE. The design by Chen et al. [26] for negative thermal strain is very similar to the unit cell found by Sigmund and Torquato [25], but is shifted half of a unit cell in horizontal direction [26]. A 3x3 array of this unit cell is visualized in Figure 1-6.

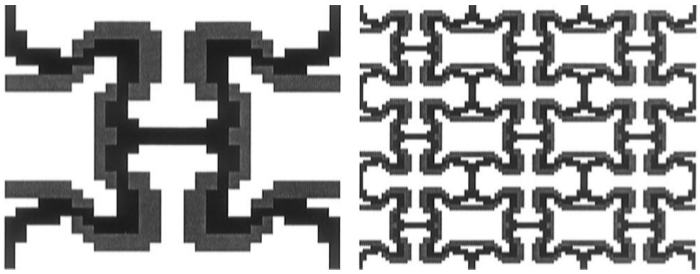

Figure 1-6: Negative thermal strain metamaterial designed by Chen et al. [26] with horizontal and vertical symmetries (black is chromium and gray is nickel). Left: Periodic unit cell; Right: 3x3 array of periodic unit cell. [26]

An interpretation of the design, obtained through post-processing of the optimization results, is manufactured using Direct Metal Deposition (DMD) and is experimentally tested by Oruganti et al. [72]. A CTE of -3.9 µm/(m°C), close to the design target of -4.0 µm/(m°C), is obtained only during the very initial contraction phase. Negative thermal expansion is obtained in both x and y direction during a small contraction phase and is about -3.0 µm/(m°C). Contraction in both directions however occurs in different temperature ranges, whilst the design is intended to have isotropic thermal expansion. Note furthermore that the sample consisted of 5 x 5 unit cells, whilst again the homogenization theory is used for the computation of the effective material properties, which assumes an infinite repetition of the unit cells.

Qi and Halloran [73] also made an engineering interpretation of the periodic unit cell with NTE presented in Chen et al. [26], by strengthening weak structures in the design and by smoothing the material distribution. The predicted CTE of the engineering interpretation was however higher than for the original design. A CTE of only -3.2 µm/(m°C), higher than the target CTE of -4.0 µm/(m°C), was predicted for the engineering interpretation. A bulk sample of the revised design was manufactured using a combination of coextrusion and warm bonding, followed by sintering. Visualizations of the revised unit cell and of the final bulk sample are given in Figure 1-7. The experimentally measured CTE of the fabricated thermoelastic metamaterials was -3.07 µm/(m°C), which is again higher than the predicted CTE of -3.2 µm/(m°C).

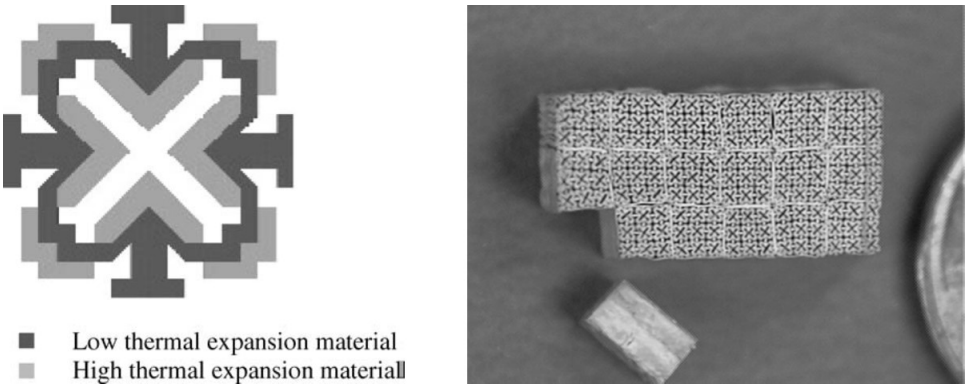

Figure 1-7: Left: Engineering interpretation by Qi and Halloran [73] of NTE metamaterial designed by Chen et al. [26]. Right: Produced NTE metamaterial by Qi and Halloran [73] using coextrusion and warm bonding. [73]

In Takezawa et al. [27] manufacturability restrictions were not included in the optimization of isotropic NTE metamaterials, but rather the design was post-processed to be producible with photopolymer AM. A test piece, visualized in Figure 1-8, was fabricated and experimentally verified. Takezawa and Kobashi [11] extended this research for thermoelastic metamaterials with anisotropic NTE and large isotropic and anisotropic PTE, which are visualized in Figure 1-9. In both Takezawa et al. [27] and Takezawa and Kobashi [11] it is stated that exact control of the effective CTE of the structures remained difficult, which was explained primarily by the strongly temperature-dependent and variable physical properties of the photopolymer used. In both studies the produced samples were again very small and consisted only of 4 x 2 unit cells.

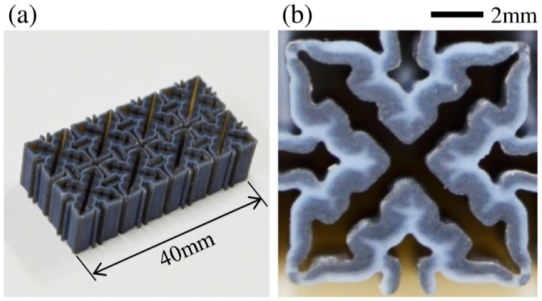

Figure 1-8: Manufactured thermoelastic metamaterial by Takezawa et al. [27], for isotropic NTE. Left (a): Outline view; Right (b): Close-up view of a single periodic unit cell. [27]

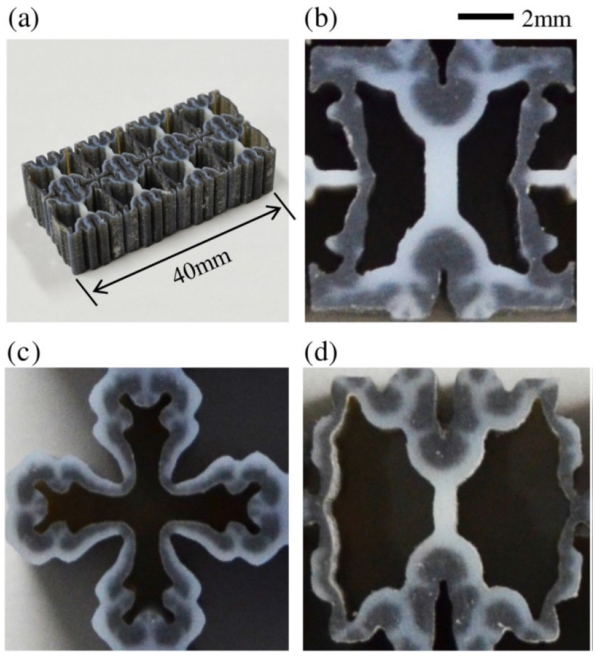

Figure 1-9: Manufactured thermoelastic metamaterials by Takezawa and Kobashi [11]. Top left (a): Outline view for anisotropic PTE metamaterial; (b-d): Close up views of single periodic unit cells. Top right (b): Anisotropic NTE; Bottom left (c): Isotropic PTE; Bottom right (d): Anisotropic PTE. [11]

Furthermore, multiple other papers present TO frameworks for the design of thermoelastic metamaterials, in which no validation has been performed numerically or experimentally [28–31]. In Andreassen et al. [28] materials were however used in the optimization compatible with cheap hobby printers and additionally a robust formulation is implemented [74], which increases the robustness of the design towards manufacturing uncertainties. Hirota and Kanno [31] used TO of frame structures to prevent hinges and thin members in the design, using predetermined candidates for the members and a ground structure. This however tremendously decreases the design space. Manufacturability is not validated in Hirota and Kanno [31]. Assumptions on manufacturability are however made, such as perfect bonding of the members at the nodes of the frame structure. In both studies the homogenization theory is used for the prediction of the effective material properties.

Conclusions

From the presented literature, it can be seen that in TO frameworks for thermoelastic metamaterials for which a sample has been manufactured, manufacturability is not included in the optimization framework. Instead, obtained optimized designs are post-processed to obtain manufacturable designs. Discrepancies between numerical and experimental values of the CTE of the optimized thermoelastic metamaterials are obtained for all manufactured samples. In Andreassen et al. [28] and Hirota and Kanno [31] manufacturability is addressed in the optimization framework, but no numerical or experimental validation of the framework is performed. Finally, it should be noted that all presented TO frameworks use the homogenization theory to compute the effective material properties of the metamaterial, which assumes an infinite repetition of the periodic unit cell. Only in Qi and Halloran [73] however a bulk sample has been made, which somehow approaches this assumption made in the homogenization theory.

1-2-5 Manufacturing

For the production of metallic thermoelastic metamaterials, a manufacturing technique is required able to produce bi-material structures from metallic constituents. AM techniques suitable for the production of bi-material metallic structures are Direct Energy Deposition (DED), Co-extrusion, Ultrasonic Additive Manufacturing (UAM) combined with a substractive manufacturing technique and a combination of photolithography, electron-beam evaporation and metal lift-off processes as presented in Yamamoto et al. [68]. The latter method has been used for the production of a thin film and is believed to be too complex and expensive for the fabrication of large blocks of metamaterial. Furthermore co-extrusion, in the authors opinion, is and will not become suitable for the realization of relatively small microstructures.

Direct Energy Deposition

In DED feeded material in either wire or powder form is melted by a laser or electron beam, after which it solidifies on a substrate [75]. A large range of metallic materials can be used for this techniques, although materials with high thermal conductivity and reflectively are harder to process [76]. Figure 1-10 shows a visualization of a wire fed direct deposition machine.

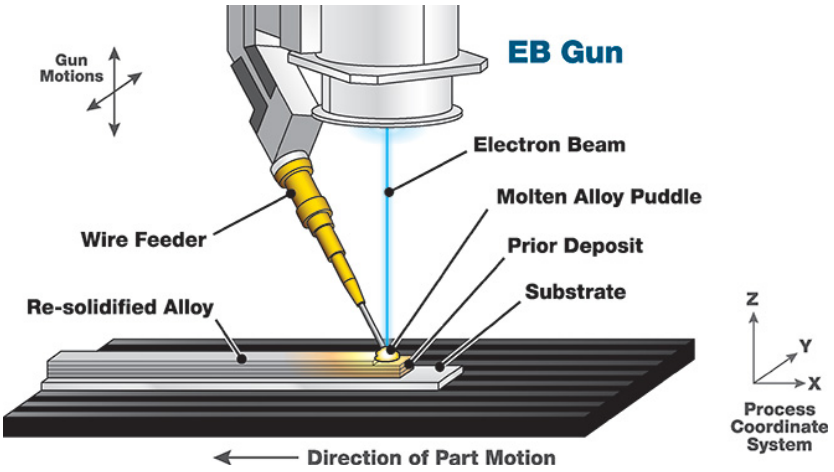

Figure 1-10: Schematic visualization of a wire fed direct deposition machine. [77]

Since heat is used to melt the material, thermal stresses are introduced which might lead to undesired deformations and bonding issues. A gradient change in material properties can be established by changing the powder input, using for example mixtures of the individual powders, which can improve the bonding quality between different materials [75].

From Table 1-1 it can be seen that using powder material, the manufacturing process is slightly slower, but superior feature size and surface roughness can be obtained compared to wire material.

Table 1-1: Achievable specifications for DED and UAM.

	DED (powder)	DED (wire)	UAM	
Feature size	0.5 mm - 1.0 mm	1.0 mm - 1.5 mm	-	[78]
Layer thickness	-	-	100 µm - 200 µm	[79]
Surface roughness	4 µm - 10 µm	8 µm - 15 µm	-	[78]
Production rate	0.1 g/s - 1.0 g/s	0.1 g/s - 2.0 g/s	25 cm/s	[78, 80]
Building volume	200 cm × 150 cm × 75 cm		182 cm × 182 cm × 91 cm	[78, 80]

Ultrasonic Additive Manufacturing

In UAM, a 3D object is formed using metallic sheets as feedstock, which are bonded using ultrasonic welding [81]. In the absence of atmosphere, metals will fuse to other metals due to shared electrons. For metals on earth, a layer of oxide however interferes with these electrons, preventing bonding between metals. In ultrasonic welding, high frequency sounds waves are used to remove the oxide layers, causing bonding of the metal foils without melting the material [82]. A wide varyity of metals can be bonded using this process [81]. A visualization of UAM is given in Figure 1-11.

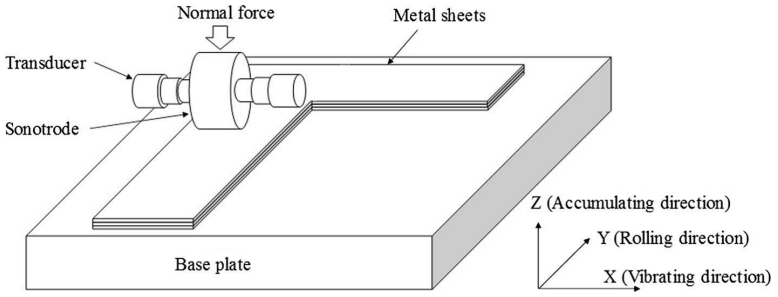

Figure 1-11: Schematic visualization of Ultrasonic Additive Manufacturing. [83]

With UAM a solid block of metal can be produced, which contains layers of different metals. An additional substractive manufacturing step, using for example Computer Nummerical Control (CNC) or Wire Electronic Discharge Machining (WEDM), allows for the creation of void spaces in the solid metal block. It should be noted that in this fashion only planar designs can be produced, with layers of just one constituent and void space. The specifications for UAM are given in Table 1-1. Note that the specifications for the final product are however also influenced by the chosen substractive manufacturing technique, which can be chosen according to the requirements drafted.

Conclusions

Both presented manufacturing techniques seem to be suitable for the production of thermoelastic metamaterials. Using DED fabrication of 3D designs is possible, whilst a combination of UAM and a substractive technique can only produce planar designs with uniform material layers. Based on the chosen substractive techniques, higher dimensional accuracy and production speed might however be obtained using UAM. Furthermore, since UAM does not use heat to bond the metals, very little thermal stresses are introduced in UAM.

1-3 Problem Statement

1-3-1 Literature gap

Thermoelastic metamaterials with ZTE have a great potential for numerous engineering applications. As elaborated in Section 1-2-2, TO is identified to be the most promising method for the design of these materials. The usage of TO for the design of thermoelastic metamaterials is not new, but existing TO frameworks lack the incorporation of manufacturability in the optimization and therefore require a post-processing step, which could compromise the optimality of the design. The following shortcomings with respect to manufacturability are often observed in these TO frameworks:

- The homogenization theory, which assumes an infinite repetition of the unit cells, is used for the computation of the effective material properties. In practice however, only unit cell arrays of finite size can be manufactured, resulting in an unavoidable difference between numerical and physical performance of the design.

- No length scale control is performed, resulting in non-manufacturable features in the optimized designs. The optimized designs need to be post-processed in order to be manufacturable, which could compromise the optimality of the designs. In existing TO frameworks for thermoelastic metamaterials, small features are for example removed in the optimized design and complex shapes are simplified.
- Manufacturing uncertainties, more specifically uncertainty on the actual feature thickness obtained during manufacturing, is rarely incorporated in the TO formulation.
- Restrictions imposed by suitable manufacturing methods for multi-material metallic parts, such as minimum feature size, uniform material layers and overhang-free topologies, are not incorporated in existing TO frameworks.

A TO framework is thus desired for the design of thermoelastic metamaterials, which incorporates manufacturability in the optimization formulation and which addresses the shortcomings of existing frameworks presented in the bullet points above. This will allow for manufacturable optimized thermoelastic metamaterials, which require limited post-processing after optimization.

1-3-2 Research aim and scope

Based on the identified literature gap we have formulated the following research aim:

> **The development and validation of a TO framework for the design of (metallic) thermoelastic metamaterials with tuneable thermal expansion, manufacturable by automated manufacturing methods, without the need for extensive post-processing of the optimized design.**

The following tasks are defined to fulfill this research aim:

> **Task 1.** Realize a TO framework for the design of manufacturable (metallic) thermoelastic metamaterials and structures of finite size;
> **Task 2.** Validate the optimized design by performing numerical experiments;
> **Task 3.** Manufacture a physical sample of the optimized design;
> **Task 4.** Validate the optimized design by performing physical experiments.

The scope of this thesis is defined as follows:

- Only 2D structures are optimized. This allows for faster development of the TO framework and furthermore results in less expensive optimizations and a better understanding of the working principle of an optimized design. After the effectiveness of the 2D TO framework has been proven, an extension towards a 3D TO framework can be made.
- Only manufacturing restrictions specific to UAM will be considered. DMD has the potential to manufacture 3D thermoelastic metamaterial designs, but the scope of this thesis is limited to 2D. The extension of the framework to incorporate DMD requires 3D compatibility, the need to prevent overhangs in the optimized designs and length scale control on the individual material phases.
- Linear elastic material behaviour and small deflections are assumed, which reduces the overall complexity of the TO framework.

- Thermoelastic metamaterial designs are optimized for uniform temperature fields. If the TO framework proves effective, extensions to linear gradients in the temperature field can be considered.
- The optimization of thermoelastic metamaterials with periodically repeated unit cells is studied, since this can reduce the computational costs considerably, which will be explained in Section 2-1-2.
- Thermoelastic metamaterials for near ZTE will be designed. This thesis originated from the need for thermoelastic metamaterials applicable to nanofabrication systems, in which ZTE materials can be used to ensure sufficient precision and stability. The TO framework is however intended to allow a tuneable CTE, including NTE and PTE.
- Since we do not have access to UAM facilities, an alternative fabrication method will be used similar to UAM, but with adhesive instead of diffused material bonds. In this fashion, the designed TO framework can still be experimentally validated. The modelling of the adhesive bonds will however not be incorporated in the TO framework, but their influence will be studied for the optimized topology only.

1-4 Outline

The TO formulation specific to manufacturable thermoelastic metamaterials will be presented in Chapter 2. Subsequently, Chapter 3 presents chosen case studies, their numerical implementation and the obtained results from the optimization. Next, in Chapter 4, numerical validation of the optimized designs is performed. The fabrication and experimental validation of the design is presented in Chapter 5. Finally, conclusions are drawn in Chapter 6 and recommendations for future work are presented.

Chapter 2

Topology Optimization for Manufacturable Thermoelastic Metamaterials

Existing TO frameworks for thermoelastic metamaterials result in optimized designs exhibiting shortcomings with respect to manufacturability, as has been addressed in Section 1-3-1. In order to improve their manufacturability, changes to the existing TO frameworks for thermoelastic metamaterials therefore are needed. In this chapter TO formulations will be presented, which are implemented in the newly proposed TO framework to improve the manufacturability of optimized thermoelastic metamaterial designs. First, in Section 2-1, the commonly used homogenization theory and the superelement method used in the new TO framework are explained, which both can be used to determine the effective material properties of a periodic metamaterial. Subsequently, in Section 2-2, a method to implement solid strips adjacent to a unit cell array is presented. Next, Section 2-3 discusses the robust formulation and how it can be used to obtain minimum length scale control. Finally, Section 2-4 explains how uniform material layers are implemented in the TO formulation.

2-1 Effective Material Properties

As introduced in Section 1-3-1, existing TO frameworks for thermoelastic metamaterials assume a metamaterial structure with infinitely repeated unit cells for the computation of the effective material properties of the metamaterial, whilst in practise obviously only finite arrays of unit cells can be manufactured. First, the homogenization theory will be presented. Subsequently, the superelement method will be explained, which will be used in the new TO framework to efficiently determine the effective material properties of a finite array of unit cells. The superelement method is already successfully implemented by Qiu [84], in a TO of cellular solids for global stiffness maximization. Qiu [84] showed the dependency of the optimal solution on the unit cell size and furthermore verified that the computational efficiency can greatly be improved using the superelement method.

2-1-1 Homogenization Theory

In order to determine the macroscopic material properties of a metamaterial from its periodic microstructure, the homogenization theory developed by Bensoussan et al. [70] and Sánchez-Palencia [71] can be used. A single unit cell is analysed in order to determine the average or homogenized material properties of an infinite array of this unit cell. The computational costs remain limited, since only one repetitive unit cell instead of an array of unit cells needs to be analysed. In order for the homogenization theory to be valid, the following conditions have to be met [85]:

1. Length scales where the theory of elasticity can be applied are considered.
2. Perfect bonding between the different materials is established.
3. The microstructure is periodically patterned in the macrostructure.
4. There is a clear separation between macro- and microscopic length scales.

A clear separation between macro- and microscopic length scales allows for an asymptotic expansion of the governing equations of a periodic composite, which is used to obtain an expressions for the effective material properties of the composite. The following expression for the macroscopic elasticity tensor is obtained from the homogenization theory [85]:

$$E^H_{ijkl} = \frac{1}{|V|}\int_V E_{pqrs}\left(\varepsilon^{0(ij)}_{pq} - \varepsilon^{(ij)}_{pq}\right)\left(\varepsilon^{0(kl)}_{rs} - \varepsilon^{(kl)}_{rs}\right)\mathrm{d}V, \tag{2-1}$$

in which $|V|$ is the unit cell volume, E_{pqrs} the locally varying stiffness tensor and $\varepsilon^{0(ij)}_{pq}$ are prescribed linearly independent macroscopic strain fields. The locally varying strain fields $\varepsilon^{(ij)}_{pq}$ are determined from the displacement fields χ^{kl} obtained by solving the following elasticity equations for the prescribed macroscopic strain fields:

$$\int_V E_{ijpq}\varepsilon_{ij}(\upsilon)\varepsilon_{pq}(\chi^{kl})\mathrm{d}V = \int_V E_{ijpq}\varepsilon_{ij}(\upsilon)\varepsilon^{0(kl)}_{pq}\mathrm{d}V\,, \qquad \forall\upsilon \in V\,, \tag{2-2}$$

which can be done numerically using the Finite Element Method (FEM). The locally varying strain fields $\varepsilon^{(ij)}_{pq}$ are computed from the displacement fields χ^{kl} according to:

$$\varepsilon^{(ij)}_{pq} = \varepsilon_{pq}(\chi^{ij}) = \frac{1}{2}\left(\chi^{ij}_{p,q} + \chi^{ij}_{q,p}\right). \tag{2-3}$$

In a similar fashion, the effective thermal stress tensor is given by [85]:

$$\beta^H_{ij} = \frac{1}{|V|}\int_V E_{pqrs}\left(\alpha_{pq} - \varepsilon^{\alpha}_{pq}\right)\left(\varepsilon^{0(ij)}_{rs} - \varepsilon^{(ij)}_{rs}\right)\mathrm{d}V, \tag{2-4}$$

in which α_{pq} is the thermal expansion tensor corresponding to a unit strain for a unit thermal load. The locally varying strain field $\varepsilon^{\alpha}_{pq}$ is again obtained from Eq. (2-3), but for the displacement field Γ found by solving:

$$\int_V \varepsilon_{ij}(\upsilon)E_{ijpq}\varepsilon_{pq}(\Gamma)\mathrm{d}V = \int_V \varepsilon_{ij}(\upsilon)E_{ijpq}\alpha_{pq}\mathrm{d}V\,, \qquad \forall\upsilon \in V\,, \tag{2-5}$$

for the unit thermal load α_{pq}, which again can be done numerically using FEM. Finally, the effective thermal strain tensor α^H is given as the solution to the discretized governing equations [85]:

$$\mathbf{E}^H\boldsymbol{\alpha}^H = \boldsymbol{\beta}^H. \tag{2-6}$$

2-1-2 Superelement method

In the homogenization theory an infinite repetition of the unit cells is assumed, since a clear separation between macro- and microscopic length scales needs to be established. In practise however, only finite arrays of unit cells can be realized. Accurately analyzing an entire unit cell array using Finite Elements (FEs) can be a computationally overwhelming task. Since our unit cell is periodically patterned in the unit cell array, we can however utilize static condensation [86] to drastically reduce the computational costs.

Assume we study a boundary value problem of a unit cell array as visualized in Figure 2-1. We can partition the Degrees of Freedom (DOFs) of a single unit cell into a set of retained DOFs and a set of condensed DOFs, which in the remainder of this section will be indicated using subscripts r and c, respectively. As visualized in Figure 2-1, the interface DOFs of our unit cells belong to the set of retained DOFs, whilst the internal DOFs of the unit cell are assigned to the set of condensed DOFs.

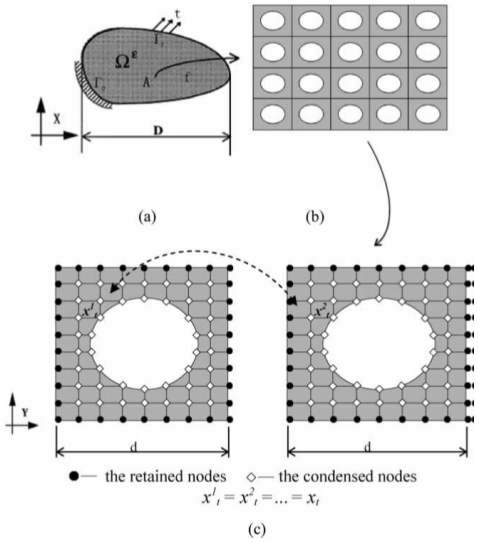

Figure 2-1: (a) Boundary value problem for which an optimal periodic cellular structure is to be found; (b) Cellular structure; (c) Two unit cells modelled using superelements with retained and condensed nodes and linked design variables. [84]

The classical FE equations can be rewritten in terms of retained and condensed DOFs:

$$\begin{bmatrix} \mathbf{K}_{\mathrm{cc}} & \mathbf{K}_{\mathrm{cr}} \\ \mathbf{K}_{\mathrm{rc}} & \mathbf{K}_{\mathrm{rr}} \end{bmatrix} \begin{bmatrix} \mathbf{u}_{\mathrm{c}} \\ \mathbf{u}_{\mathrm{r}} \end{bmatrix} = \begin{bmatrix} \mathbf{f}_{\mathrm{c}} \\ \mathbf{f}_{\mathrm{r}} \end{bmatrix}, \tag{2-7}$$

in which $\mathbf{f}_{\mathrm{r}}$ and $\mathbf{f}_{\mathrm{c}}$ are the equivalent force vectors applied on the retained and condensed DOFs, respectively. The partial stiffness matrices of the retained and condensed DOFs are indicated with $\mathbf{K}_{\mathrm{rr}}$ and $\mathbf{K}_{\mathrm{cc}}$, respectively. From the first line of Eq. (2-7) we obtain:

$$\mathbf{u}_{\mathrm{c}} = \mathbf{K}_{\mathrm{cc}}^{-1} \left(\mathbf{f}_{\mathrm{c}} - \mathbf{K}_{\mathrm{cr}} \mathbf{u}_{\mathrm{r}} \right) . \tag{2-8}$$

Substitution of Eq. (2-8) in Eq. (2-7) yields the following reduced system of equations that exactly represents the system behaviour in terms of the retained DOFs:

$$\left(\mathbf{K}_{\mathrm{rr}} - \mathbf{K}_{\mathrm{rc}} \mathbf{K}_{\mathrm{cc}}^{-1} \mathbf{K}_{\mathrm{cr}} \right) \mathbf{u}_{\mathrm{r}} = \mathbf{f}_{\mathrm{r}} - \mathbf{K}_{\mathrm{rc}} \mathbf{K}_{\mathrm{cc}}^{-1} \mathbf{f}_{\mathrm{c}}. \tag{2-9}$$

The displacements of the retained DOFs are obtained by solving the system of equations given in Eq. (2-9). The displacements for the condensed DOFs can be obtained by substitution of the displacements for the retained DOFs into Eq. (2-8).

Note that the generation of the reduced system of equations also requires computational effort. The considered unit cell array is however periodic, hence all unit cells share the same topology. Therefore, the static condensation procedure only has to be performed once every iteration to obtain a superelement representing a single unit cell. After static condensation of a single unit cell has been performed, an assembly operation of the superelements is performed similar to the assembly operation of individual elements as used in the standard FEM for eight-node quadrilateral elements. The node and superelement numbering used in the assembly operation of the condensed unit cells is visualized in Figure 2-2.

The stiffness matrix and force vector for the entire unit cell array are now obtained, expressed only in terms of the retained DOFs. For the unit cell array displayed in Figure 2-2, in which each superelement in modelled using a 3 x 3 element mesh, the reduction of the number of DOFs of the system of equations that needs to be solved is larger than a factor 1.5. For larger unit cell arrays, especially when the unit cells are modelled using a finer mesh, the reduction of the number of DOFs for the reduced system of equations is much larger.

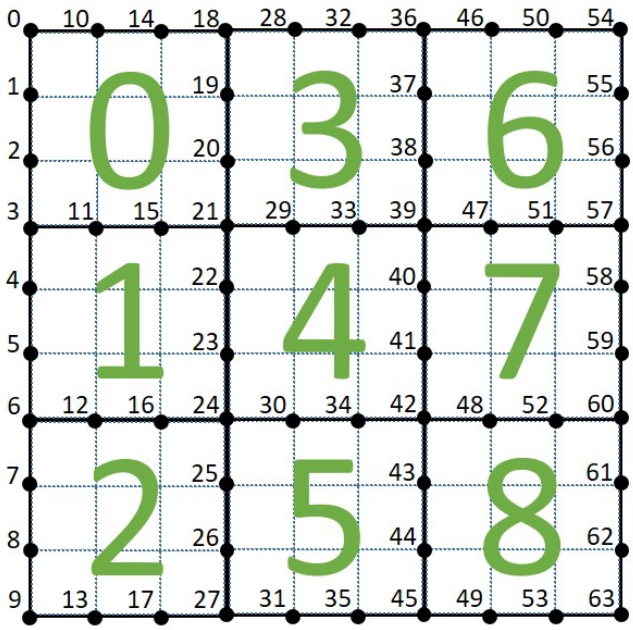

Figure 2-2: Node (black) and superelement (green) numbering used in the assembly operation of the superelements, assuming each super element is obtained by static condensation of a 3 x 3 element mesh.

Using static condensation we can thus obtain a reduced system of equations which exactly describes the behaviour of the unit cell array, expressed only in terms of the retained DOFs. Solving the reduced system of equations will require far less computational effort compared to solving the full system of equations, especially for large unit cell arrays in which each unit cell is modelled using a fine mesh.

2-2 Solid strips

In order to obtain a practically usable thermoelastic metamaterial structure, which can be mounted to other components, strips of solid material are connected to the metamaterial structure. The addition of these solid strips will however influence the behaviour of the structure, since it can no longer move freely at its boundary. In order to account for this influence, the solid strips should be incorporated in the analyses of the thermoelastic metamaterial structure performed during the optimization procedure. Opposed to the homogenization method, the static condensation approach allows the implementation of the solid strips in the analysis of the thermoelastic metamaterial structure.

A uniform solid topology is assigned to the upper and lower row of unit cells. The topology of the solid strips is excluded from the density variables used in the optimization and is not altered in the optimization procedure. Before the optimization procedure is started, static condensation is performed of a single unit cell having this solid single-material topology, in order to obtain its reduced stiffness matrix and force vector. Since these unit cells are excluded from the TO, their topology does not change and hence their reduced stiffness matrix and force vector do not change either. The solid strips therefore do not have to be included in the sensitivity analysis performed in the optimization procedure. The reduced stiffness matrix and force vector are now used in the assembly operation of the superelements, for the upper and lower row of unit cells. The upper and lower row of unit cells therefore now form solid strips of a single material. In Figure 2-2, superelements 0, 2, 3, 5, 6 & 8 would be solid and composed of a single material when using the presented concept of solid strips.

2-3 Robust Formulation

The robust formulation is an extension of the standard TO formulation, that accounts for uncertainties during fabrication of the topology [87]. In robust TO, we optimize for the worst case of an eroded, intermediate and dilated topology. The manufacturing error bounds on both the solid and void phases are therefore defined by the difference between the eroded, intermediate and dilated designs. The eroded, intermediate and dilated topologies are obtained by applying a traditional density filter and subsequently, applying a smooth threshold projection on the filtered density field for different threshold values. In this section, it is first explained how the density filter is applied and how a filter domain extension is implemented, used to obtain minimum length scale control at the boundaries of the unit cells. Next, it is explained how the smooth threshold projection is performed and how minimum length scale control can be established using the robust formulation. Finally, an example of a robust TO formulation is presented for a simple two-phase minimum compliance TO problem.

2-3-1 Filtering

Density filter

The eroded, intermediate and dilated topologies are obtained by first applying a density filter as introduced by Bruns and Tortorelli [88], defining the filtered density of an element as [87]:

$$\tilde{x}_1 = \frac{\sum\limits_{i \in N} w\left(\boldsymbol{s}^i\right) v^i {x_1}^i}{\sum\limits_{i \in N} w\left(\boldsymbol{s}^i\right) v^i}, \tag{2-10}$$

in which v^i and ${x_1}^i$ denote the volume and density of an element i, respectively, belonging to a set of neighborhood elements that have centers within a given filter radius R of the center of the considered element. The neighborhood N is defined by [87]:

$$N = \left\{ i \mid \left\| \boldsymbol{s}^i - \boldsymbol{s}^{\mathrm{c}} \right\| \leq R \right\}, \tag{2-11}$$

where $\boldsymbol{s}^i$ and $\boldsymbol{s}^{\mathrm{c}}$ refer to the spatial coordinates of elements i and the element for which the neighbourhood N is determined, respectively. In Eq. (2-10), $w\left(\boldsymbol{s}^i\right)$ is a weighting function given by the linearly decaying (cone-shape) function [87]:

$$w\left(\boldsymbol{s}^i\right) = R - \left\| \boldsymbol{s}^i - \boldsymbol{s}^{\mathrm{c}} \right\|. \tag{2-12}$$

Filter domain extension

The design variables used in the proposed TO formulation only describe the topology of a single unit cell, since periodic unit cell structures are considered and the topology for the solid strips is non-variable. All the unit cells of the unit cell array should be exactly the same, such that the superelement method described in Section 2-1-2 can be utilized, to limit the computational costs of the analyses. The density filter described above, is therefore only applied to the density field describing the topology of a single unit cell.

Using the robust formulation, minimum length scale control can be established at the interior of the considered density field, which for the proposed formulation thus is the interior of a single unit cell. The interior is defined as the density field which is at least a filter radius away from the boundary. Minimum length scale control is not guaranteed at the boundaries of the considered density field. If minimum length scale control is not established at the boundaries of the unit cell topology, small non-manufacturable features can occur at the interfaces between the different unit cells of the optimized finite unit cell array.

In order to preserve minimum length scale control at the interfaces between the different unit cells, a filter domain extension approach is utilized as visualized in Figure 2-3. The filter domain is extended with at least the filter radius used in the density filter. The density field constructed for the filter domain extension assumes that unit cells are adjacent to the considered unit cell which share the same topology, since a periodic unit cell array is optimized. After the filter domain is extended and the filtering operation is performed, the filtered density field is again reduced to the field for the single unit cell, which is enclosed with red lines in Figure 2-3.

The boundary of the considered density field, at which minimum length scale is not guaranteed, now lies outside the density field describing the unit cell topology. The density field for the considered unit cell lies within the interior of the considered density field, where minimum length scale control is obtained, assuming that the extended filter domain is valid.

It should be emphasised that using the proposed filter domain extension approach, minimum length scale control is only obtained at the boundaries where the used filter extension is valid. The top boundary of the top layer of unit cells for example, adjoin the solid strip and not another unit cell having the same topology. At the top boundary of the top layer of unit cells, minimum length scale control is therefore not obtained. Similarly, minimum length scale control is not guaranteed at the bottom boundary of the bottom layer of unit cells, the left boundary of the left column of unit cells and the right boundary of the right column of unit cells, since for these boundaries the considered filter domain extension is not valid.

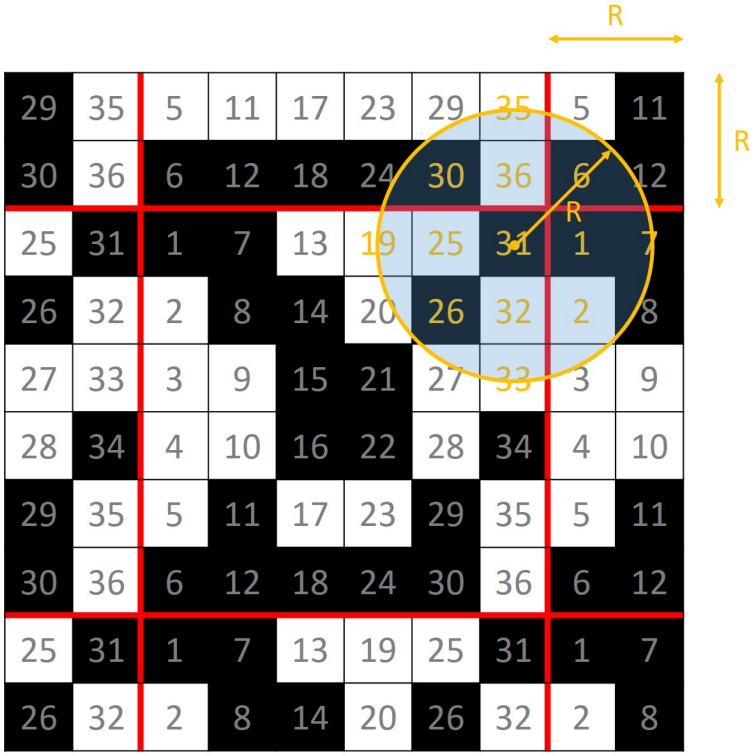

Figure 2-3: Visualization of the filter domain extension approach, for a unit cell discretized using 6 x 6 elements (enclosed by the red lines) and a filter radius of R = 2.

2-3-2 Threshold projection

Subsequently, a threshold projection is performed in which the filtered densities are projected onto a 0/1 solution. The threshold projection for an element is given by [74]:

$$\bar{\tilde{x}}_1 = \frac{\tanh(\beta\eta) + \tanh\left(\beta\left(\tilde{x}_1 - \eta\right)\right)}{\tanh(\beta\eta) + \tanh(\beta(1-\eta))}, \tag{2-13}$$

which is a smooth function that projects filtered densities below a threshold η towards 0 and filtered densities above a threshold η towards 1. The sharpness of the smooth projection is controlled by the projection parameter β. Dilated, intermediate and eroded designs can be formulated using the threshold projection with the threshold value η chosen as $\delta, 0.5$ and $1-\delta$,respectively, where $\delta \leq 0.5 \leq 1-\delta$. The smooth threshold projection steers the optimization towards 0/1 solutions.

2-3-3 Length scale control

For a robust TO formulation, the intermediate design is used as a blue-pint for the optimized topology. The minimum length scale on the intermediate design can be controlled by selecting a specific combination of filter radius R and the parameter δ, which is used to define the threshold parameter η for the eroded and dilated topology. The used projection parameter β for the threshold projection should furthermore be sufficiently large. The relation between the minimum length scale b, filter radius R and the parameter δ is provided by Wang et al. [74] and is visualized in Figure 2-4. The minimum length scale in 2D is defined by a circle dot with diameter b. This relation however only holds when the eroded, intermediate and dilated designs share the same topology. Minimum length scale control is furthermore not established for the individual solid phases, since the eroded and dilated design used in the robust formulation are only with respect to the density field.

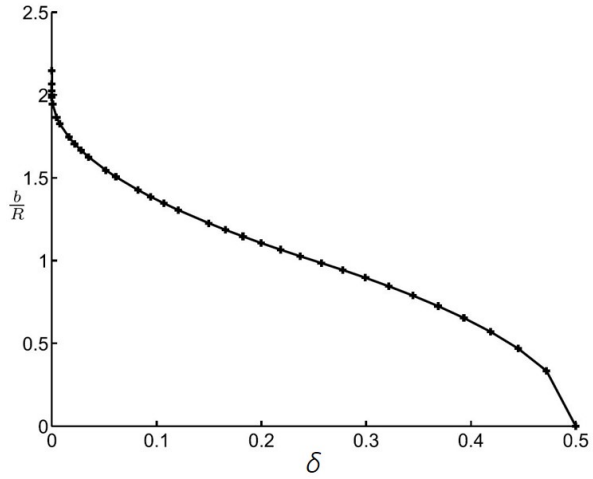

Figure 2-4: Normalized length scale on the intermediate design as a function of δ, for a threshold value for the intermediate topology of $\eta_i = 0.5$. The parameter δ is used to describe the threshold of the dilated and eroded topology, which are $\eta_d = \delta$ and $\eta_e = 1 - \delta$ with $\delta \leq 0.5 \leq 1 - \delta$, respectively. Presented relation is derived in [74] and presented in [89].

2-3-4 Robust optimization formulation

The robust TO formulation is dependent on the optimization problem considered. The robust TO formulation for a simple two-phase compliance minimization problem is given by:

$$\begin{aligned} \min_{\mathbf{x}_1} &: \max\left(\mathbf{f}_{\mathrm{e}}^T\mathbf{u}_{\mathrm{e}}, \mathbf{f}_{\mathrm{i}}^T\mathbf{u}_{\mathrm{i}}, \mathbf{f}_{\mathrm{d}}^T\mathbf{u}_{\mathrm{d}}\right) \\ \text{s.t.} &: V_{\mathrm{e}}/V^* - 1 \leq 0, \\ &: V_{\mathrm{i}}/V^* - 1 \leq 0, \\ &: V_{\mathrm{d}}/V^* - 1 \leq 0, \\ &: \mathbf{0} \leq \mathbf{x}_1^{\min} \leq \mathbf{x}_1 \leq \mathbf{1}, \end{aligned} \tag{2-14}$$

in which $\mathbf{f}$ and $\mathbf{u}$ are the nodal force and displacement vectors, respectively. V is the material volume fraction. The subscripts e, i and d refer to the eroded, intermediate and dilated topologies, respectively. Furthermore, V^* is the prescribed maximum material volume fraction and $\mathbf{x}_1^{\min}$ is a vector of minimum density values.

In general, the robust formulation is more expensive than the standard TO formulation, since two additional Finite Element Analyses (FEAs) are required to obtain the solutions for the eroded and dilated topologies. For the simple compliance minimization problem given in Eq. (2-14), the compliance of the eroded topology is however always larger than the compliance for the intermediate and dilated topologies. Therefore, two FEAs can be saved which are used to solve for the displacement vectors of the intermediate and dilated topologies. The volume of the dilated topology is furthermore always larger than the volume of the eroded and intermediate topologies. Therefore, only the volume constraint on the dilated topology needs to be enforced. The robust TO formulation for a three-phase thermoelastic metamaterial is described in Chapter 3.

2-4 Uniform Material Layers

Manufacturability of thermoelastic metamaterials using UAM is considered in this work. Therefore, it is required that optimized designs contain layers consisting of just one of the material phases and void space. First, we will present the material interpolation scheme used in the TO framework. This material interpolation scheme can be utilized to enforce uniform material layers, as will be explained subsequently.

2-4-1 Multi-material interpolation scheme

Since the working principle of thermoelastic metamaterials is based on the difference in CTE of the materials used in its structure, a multi-material interpolation scheme is implemented in the TO formulation. Similar to Sigmund and Torquato [5], a three-phase mixture scheme is used to describe the local stiffness and thermal strain coefficient tensors in an element as:

$$C_{ijkl}(x_1, x_2) = (x_1)^{\mathrm{p}}[(1 - x_2)C_{ijkl}^{(1)} + x_2 C_{ijkl}^{(2)}], \tag{2-15}$$

$$\alpha_{ij}(x_2) = (1 - x_2)\alpha_{ij}^{(1)} + x_2\alpha_{ij}^{(2)}, \tag{2-16}$$

where x_1 is a local density variable and x_2 is a local mixture coefficient. The mixture coefficient x_2 is used to distinguish between the different solid phases. $x_2 = 0$ results in an element purely consisting of phase 1 and $x_2 = 1$ results in an element purely consisting of phase 2. Intermediate values of x_2 indicate a mixture of the two phases. Furthermore, a penalization parameter p is included, which for values larger than 1 makes intermediate densities uneconomical and therefore steers the optimization towards a 0/1 solution for compliance minimization problems with volume constraints. It should be noted that the implementation as used in the new TO formulation requires the Poisson's ratio of both material phases to be equal.

2-4-2 Fixed mixture coefficients

The usage of the three-phase mixture scheme allows for a distinction between the different solid phases using the mixture coefficient x_2. Therefore, uniform material layers can very easily be implemented, by taking the the mixture coefficient x_2 constant and assigning the same value, either 0 or 1, to every element within a single material layers. A visualization of this concept is presented in Figure 2-5. Note that in the implementation as used in the proposed TO formulation, the position and thicknesses of the uniform material layers are fixed.

0	0	0	0	0	0	0	0
1	1	1	1	1	1	1	1
0	0	0	0	0	0	0	0
1	1	1	1	1	1	1	1

Figure 2-5: Visualization of a mixture coefficient field for a 8 x 4 mesh, in which the mixture coefficients are fixed to enforce uniform material layers.

Fixed material constants for each material layer could also have been used instead of the three-phase mixture scheme with fixed mixture coefficients. Using the three-phase mixture scheme, the TO framework can however more easily be extended, such that the position and thickness of the material layers can additionally be optimized in future work.

Chapter 3

Numerical Implementation

The numerical implementation and results of the optimization problem for a stiff thermoelastic metamaterial with ZTE will be discussed in this chapter. First, in Section 3-1, the individual components of the formulation for the optimization problem as used in the new TO framework will be discussed. Next, in Section 3-2, an overview is given of the cases which are studied using the TO framework. Finally, the results for these cases are presented in Section 3-3.

3-1 Formulation of the Optimization Problem

The individual components of the optimization problem for a stiff thermoelastic metamaterial with ZTE will be discussed in the remainder of this section. Furthermore, the resulting final optimization formulation is given.

3-1-1 Objective function

In order to obtain a stiff thermoelastic metamaterial, the objective function which is minimized during the optimization describes the compliance of the unit cell array for a load case as visualized in Figure 3-1, in which a unit distributed load is applied to the top boundary of the unit cell array. Since we are using the robust formulation, we are optimizing for the worst performing topology of the eroded, intermediate and dilated topologies. The compliance of the eroded topology will always be larger than the compliance of the intermediate and dilated topology, hence we use the following expression for the objective function:

$$f = \mathbf{f}_{\mathrm{e}}^T \mathbf{u}_{\mathrm{e}} \tag{3-1}$$

in which $\mathbf{u}_{\mathrm{e}}$ and $\mathbf{f}_{\mathrm{e}}$ are the nodal displacement vector and load vector for the eroded topology, respectively, for the load case as visualized in Figure 3-1.

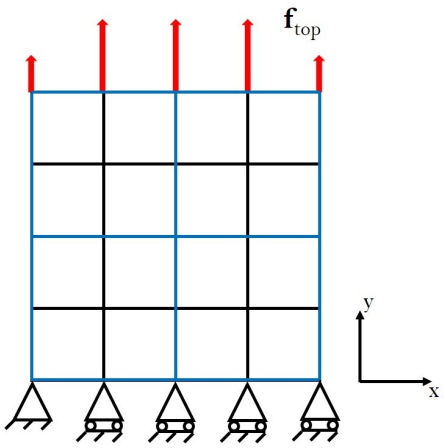

Figure 3-1: Example load case for a 2 x 2 unit cell array used to compute the compliance described in the objective function. In this presented example, each unit cell consists of a 2 x 2 element mesh and a unit load per unit cell array width $\mathbf{f}_{top}$, visualized using red arrows, is applied on the top boundary of the unit cell array.

3-1-2 Design variables, mixture assumption and symmetry

As already presented in Section 2-4-1, a three-phase mixture scheme is used to describe the local stiffness and thermal strain coefficient tensors. This mixture scheme uses a density variable and a mixture coefficient for every element. It should be noted however that we are optimizing a periodic unit cell array, hence all unit cells should share the same topology. The density variable and mixture coefficients therefore only have to describe the topology of a single unit cell. Using geometrical symmetry conditions, the size of the density vector describing the topology can be even further reduced. In the presented TO a vertical symmetry axis is enforced, since symmetric topologies are expected for the applied load cases. Enforcing geometrical symmetry helps to prevent unsymmetrical topologies due to small numerical errors and furthermore allows for further reduction of the design variable vector. In the presented formulation, the left half of the unit cell topology is described in the design variable vector. The total unit cell topology is obtained by applying a simple mirror operation.

3-1-3 Constraints on volume fractions

Volume constraints are enforced on the topology of a single unit cell, in order to steer the optimization towards 0/1 solutions, as elaborated in Section 2-4. Since we additionally use a robust formulation, the volume constraints are however not essential to obtain 0/1 solution. Nevertheless, they will help to limit the maximum weight of the thermoelastic unit cell array. Since the volume of the solid phases for the dilated topology will always be the largest, the volume constraints will only have to be applied to the dilated topology. The TO framework uses a structured mesh in which all elements have the same size. The volume fractions for the dilated topology of the three material phases can therefore be expressed as:

$$V_{\mathrm{d}}^{(1)} = \sum_{N} (\overline{\overline{x}}_1)_{\mathrm{d}} (1 - x_2), \qquad V_{\mathrm{d}}^{(2)} = \sum_{N} (\overline{\overline{x}}_1)_{\mathrm{d}} (x_2), \qquad V_{\mathrm{d}}^{(0)} = 1 - V_{\mathrm{d}}^{(1)} - V_{\mathrm{d}}^{(2)}, \tag{3-2}$$

in which N is the number of FEs used to discretize the unit cell. $(\overline{\tilde{x}}_1)_\mathrm{d}$ is the element density variable for the dilated topology, which has been filtered and for which a threshold projection has been performed as described in Section 2-3. An upper bound constraint is formulated for both solid material phases, according to:

$$g_{V1} = \frac{V_\mathrm{d}^{(1)}}{V_\mathrm{max}^{(1)}} - 1 \leq 0, \qquad g_{V2} = \frac{V_\mathrm{d}^{(2)}}{V_\mathrm{max}^{(2)}} - 1 \leq 0, \tag{3-3}$$

with $V_\mathrm{max}^{(1)}$ and $V_\mathrm{max}^{(2)}$ being the upper bounds for solid phases 1 and 2, respectively.

3-1-4 Unidirectional thermal expansion constraint

The Mean Square Error (MSE) of the top-node displacements of the topology, resulting from a thermal loadcase as visualized in Figure 3-2, is constrained in order to obtain a tailored unidirectional thermal expansion for the thermoelastic metamaterial structure. The nodal forces for the thermal loadcase, which model the thermal expansion of the unit cell array for $\Delta T = 1\,^\circ\mathrm{C}$, are computed according to:

$$\mathbf{f}_\mathrm{t} = \sum_N A\mathbf{B}^T\mathbf{D}\boldsymbol{\varepsilon}_\mathrm{t}, \tag{3-4}$$

with $\sum$ denoting an assembly operator of all FEs N, A is the element surface, $\mathbf{B}$ the element strain-displacement matrix, $\mathbf{D}$ the element stress-strain relation matrix and $\boldsymbol{\varepsilon}_\mathrm{t}$ the element thermal strain vector, which for plane-stress conditions is given by:

$$\boldsymbol{\varepsilon}_\mathrm{t} = \begin{pmatrix} \alpha\Delta T \\ \alpha\Delta T \\ 0 \end{pmatrix} \tag{3-5}$$

An MSE constraint is used to simultaneously constrain both the average value and variation of the vertical thermal displacements of the unit cell array's top nodes and is given by:

$$\sum_{i=1}^{N_\mathrm{top}} (u_\mathrm{y}^i - u_0)^2 \leq c_\mathrm{MSE} \tag{3-6}$$

in which u_y^i is the vertical thermal displacement for a node i belonging to the set of top nodes of the unit cell array, resulting from the thermal loadcase which models the thermal expansion of the unit cell array for $\Delta T = 1\,^\circ\mathrm{C}$. u_0 is the intended average value for the displacements of the top nodes, which for a ZTE thermoelastic metamaterial has to be chosen zero. The parameter c_MSE is the upper bound for the constraint, which determines the measure in which the vertical thermal top displacements are allowed to vary from their intended average value. In order to prevent small values for the sensitivities obtained for the constraint given in (3-6), the constraint is transformed using a logarithmic function. The transformed constraint is given by:

$$g_\mathrm{MSE} = \log_{10}\left(\sum_{i=1}^{N_\mathrm{top}} (u_\mathrm{y}^i - u_0)^2\right) - \log_{10}\left(c_\mathrm{MSE}\right) \leq 0, \tag{3-7}$$

which can be enforced on the eroded, intermediate and dilated topologies by inserting the thermal top node displacements u_{y}^{i} of the corresponding topology. The constraint is enforced on the eroded, intermediate and dilated topology, in order to ensure robustness of the design towards its unidirectional thermal expansion.

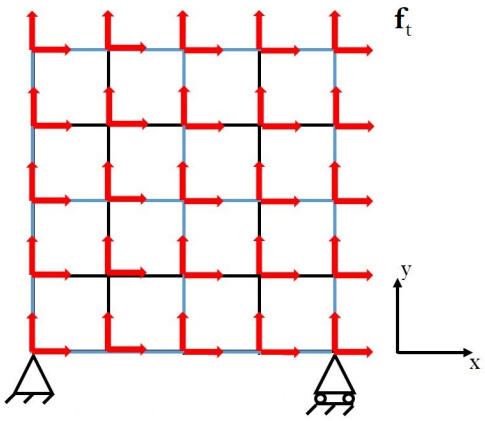

Figure 3-2: Example thermal load case for a 2 x 2 unit cell array, with each unit cell having a 2 x 2 element mesh, used to compute the thermal top displacements used in the MSE constraint. A unit thermal load for $\Delta T = 1\,^{\circ}\mathrm{C}$, visualized using red arrows, is applied to the nodes. The magnitude of the thermal load in each node is dependent on the material phases of the surrounding elements.

3-1-5 Lower bound constraint on design variables

In order to prevent singularity of the stiffness matrix in the FE formulation, a lower bound constraint on the density variables is enforced, which is given by:

$$\mathbf{0} \leq \mathbf{x}_1^{\min} \leq \mathbf{x}_1 \leq \mathbf{1}, \tag{3-8}$$

in which $\mathbf{x}_1^{\min}$ is a vector containing the same minimum density value $x_1^{\min}$ for each element.

3-1-6 Final optimization problem

The final optimization problem can now be summarized as:

$$\begin{aligned}
\min_{\mathbf{x}_1} :\ & \mathbf{f}_{\mathrm{e}}^{T}\mathbf{u}_{\mathrm{e}}, \\
\text{s.t.} :\ & (g_{\mathrm{MSE}})_H \leq 0 \qquad \text{for} \qquad H = \{\mathrm{e},\mathrm{i},\mathrm{d}\}, \\
& g_{V1} \leq 0, \\
& g_{V2} \leq 0, \\
& \mathbf{0} \leq \mathbf{x}_1^{\min} \leq \mathbf{x}_1 \leq \mathbf{1}, \\
& \text{Vertical line symmetry.}
\end{aligned} \tag{3-9}$$

Note that the element mixture coefficients $\mathbf{x}_2$ are fixed, resulting in a two-phase TO problem.

3-1-7 Optimization algorithm

The final optimization problem will be optimized using the Method of Moving Asymptotes (MMA) [90]. MMA is commonly used in TO and is a versatile gradient-based optimization algorithm that is well suited for large scale TO problems.

3-2 Cases

In this section, the verification cases for the newly proposed TO framework are presented. The overall optimization problem is elaborated and relevant parameter setting are presented. An overview of the relevant parameters and their chosen values is presented in Appendix B.

3-2-1 Layout and materials

The topology of a finite 2D unit cell array will be optimized using the TO framework. Solid strips attached to the top and bottom of the unit cell array are considered in the optimization. The unit cell array is defined by the parameters presented in Table 3-1. The number of superelements in y-direction, include two superelements used to model the solid strips, as can be seen in Figure 3-3. The dimensions of the unit cell array are equally distributed over the unit cells, hence all superelements have the same size.

Table 3-1: Finite unit cell array parameters used for the optimization cases.

Parameter	Value	Description
s_{x}	2	Number of superelements in x-direction
s_{y}	5	Number of superelements in y-direction
l_{x}	0.15	Total width unit cell array in meters
l_{y}	0.15	Total height unit cell array in meters

The parameters used to describe the unit cells and their discretization are presented in Table 3-2. The unit cells are discretized using square elements and the arrangement and properties of each material layer is fixed.

Table 3-2: Unit cell parameters used for the optimization cases.

Parameter	Value	Description
n_{x}	150	Number of FE in x-direction for unit cell discretization
n_{y}	60	Number of FE in y-direction for unit cell discretization
z_{nr}	2	Number of uniform material layers per unit cell
z_{seq}	Aluminium + Steel	Top to bottom sequence of uniform material layers

The properties of the solid phases used in the optimization of the unit cell topology are presented in Table 3-3. Both aluminium and steel are used in the optimization. These metals are commonly available and have the same Poisson's ratio but different CTE, which can be utilized in the optimization to obtain ZTE.

Table 3-3: Material properties of materials used for the optimization cases.

Material	Parameter	Value	Description
Aluminium	E	69	Young's modulus in GPa
	α	23.6	CTE in µm/(m°C)
	v	0.33	Poisson's ratio
Steel	E	210	Young's modulus in GPa
	α	12.0	CTE in µm/(m°C)
	v	0.33	Poisson's ratio

A visual representation of the optimization case is presented in Figure 3-3. Note that the solid strips remain solid during the optimization. The topology of the design domain is optimized and due to the specified periodicity, all unit cells in the design domain share the same topology. The location of the steel and aluminium material cannot be changed as previously explained in Section 2-4, due to the specified fixed mixture coefficient.

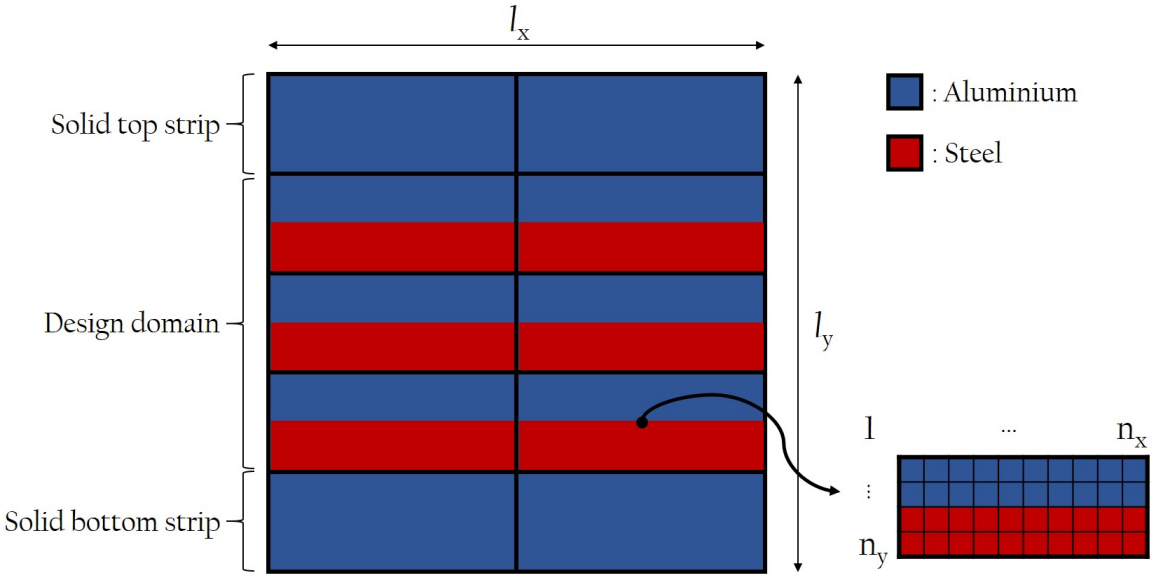

Figure 3-3: Visual representation of the optimization case performed to verify the new TO framework, with s_x x s_y equal to 2 x 5. The superelements in the design domain each represent one unit cell of the unit cell array. The location of the aluminium and steel material is fixed throughout the optimization.

3-2-2 Constraint bounds

The specified bounds for the constraints introduced in Section 3-1 are given in Table 3-4. The upper bounds for the volume constraints are chosen such, that sufficient material is available to obtain an optimized topology, whilst limiting the maximum weight of the design.

Table 3-4: Bounds for the constraints used in the optimization cases.

Parameter	Value	Description
$V_{\max}^{(1)}$	0.40	Maximum volume fraction aluminium phase
$V_{\max}^{(2)}$	0.25	Maximum volume fraction steel phase
c_{MSE}	2.43×10^{-10}	MSE constraint value vertical thermal top displacements

The upper bounds for the MSE constraint presented in Eq. (3-7), is specified in Table 3-4 and is determined using the following expression:

$$c_{\text{MSE}} = \frac{1}{10}(s_{\text{x}} n_{\text{x}} + 1)(l_{\text{y}} \alpha_{\text{steel}})^2 \tag{3-10}$$

This expression allows a slight variation in the vertical thermal displacements of the unit cell array's top nodes. The upper bound is chosen such, that the MSE of the vertical thermal displacements of the top nodes is smaller than one tenth of the MSE expected for a solid steel block of similar size, computed using a zero target average displacement. This allows a slight variation in the vertical thermal displacements of the top nodes of the unit cell array, that allows the optimizer to find a feasible solution. It however prevents large vertical thermal displacements and ensures that the unidirectional thermal expansion of the unit cell array is considerably smaller than for steel. Exact ZTE over the entire width of the unit cell array is however not guaranteed and will likely not be obtained.

3-2-3 Robust formulation parameters

The parameters related to the robust formulation are presented in Table 3-5 and are chosen such, that a minimum length scale of 2 mm is obtained, which is larger than the waterjet diameter of approximately 1 mm, that is used for the fabrication of the sample as later elaborated in Section 5-2. A combination of R and δ is chosen using the relation presented in Figure 2-4, such that a minimum length scale b of 2 mm is obtained. A continuation strategy is used for the projection parameter β. In the first iteration, the projection parameter is set to β_{init}. For every consecutive iteration, the projection parameter is multiplied by a growth factor f_β, until a value of is $\beta_{\max}$ obtained. The projection parameter is gradually increased by specifying a low growth factor, to prevent numerical problems [87].

Table 3-5: Robust formulation parameters used for the optimization cases.

Parameter	Value	Description
R	5.33	Filter radius expressed in elements
β_{init}	1.0	Initial projection parameter
f_β	1.05	Growth factor projection parameter
$\beta_{\max}$	20.0	Maximum projection parameter
η_{i}	0.50	Threshold parameter intermediate topology
$\eta_{\text{d}} = \delta$	0.35	Threshold parameter dilated topology
$\eta_{\text{e}} = 1 - \delta$	0.65	Threshold parameter eroded topology

3-2-4 Optimization setting

The optimization parameters are presented in Table 3-6. In accordance with common practise, the solution is said to be converged when the change of the design variables is smaller than x_{tol}. Additionally, the solution is said to be converged when the change of the objective in smaller than ob_{tol} for $ob_{\max}$ consecutive iterations, to prevent excessive iterations.

Furthermore, note that the objective is scaled such that a value of O_{scale} is obtained in the first iteration. The value of O_{scale} has been determined empirically and ensures that the objective for the majority of the iterations has a value between 1 and 100, which is preferred for the MMA algorithm [91].

Table 3-6: Optimization parameters used for the optimization cases.

Parameter	Value	Description
$it_{\max}$	250	Maximum number of iteration
x_{tol}	1×10^{-4}	Minimum change design variables
$ob_{\max}$	3	Maximum number of consecutive iterations meeting ob_{Tol}
ob_{tol}	0.01	Minimum change objective in percent
$x_{\min}$	1×10^{-10}	Minimum value density variables
O_{scale}	0.1	Scaling factor objective

Initial density field

The TO is initialized using a uniform density distribution, which is considered common practise [92], with initial density values x_0 of 0.25, 0.50 and 0.75.

3-3 Results

The results of the verification cases are summarized in Table 3-7. The density fields for a single unit cell are given in Table 3-8 and the topologies for the optimized unit cell arrays are presented in Table 3-9. The vertical thermal displacements of the top nodes of the unit cell arrays are plotted in Figure 3-4. Convergence plots are presented in Appendix C.

The eroded, intermediate and dilated topologies are the same for the verification case initialized using $x_0 = 0.25$. The topologies however vary locally for the verification cases initialized using $x_0 = 0.50$ and $x_0 = 0.75$. For all verification cases, the vertical thermal displacement of the top boundary is small compared to the displacement expected for a steel topology of similar size, which is 1.8×10^{-6} m. Further discussion of the results is presented in Chapter 4 and Chapter 5.

Table 3-7: Summary of the results from the optimization cases.

	$x_0 = 0.25$	$x_0 = 0.50$	$x_0 = 0.75$
Compliance [J]	1.83×10^{-9}	2.19×10^{-9}	1.37×10^{-9}
Converged	No	No	Yes
Constraints satisfied	Yes	No	Yes

Table 3-8: Projected density fields for a single unit cell.

	$x_0 = 0.25$	$x_0 = 0.50$	$x_0 = 0.75$
Eroded		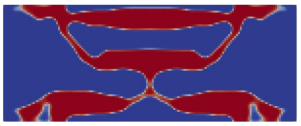	
Intermediate			
Dilated			

Table 3-9: Topologies of the finite unit cell arrays, visualized by using a threshold of 0.5 on the projected density fields.

	$x_0 = 0.25$	$x_0 = 0.50$	$x_0 = 0.75$
Eroded	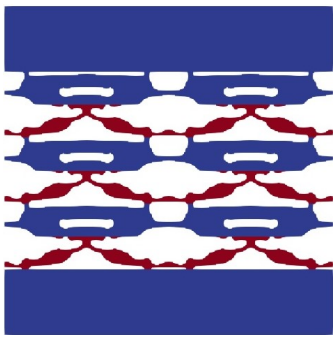	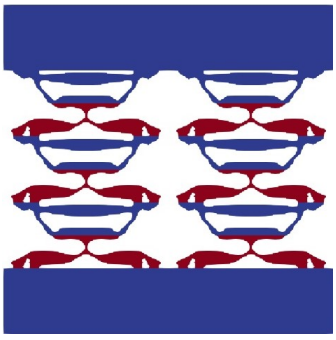	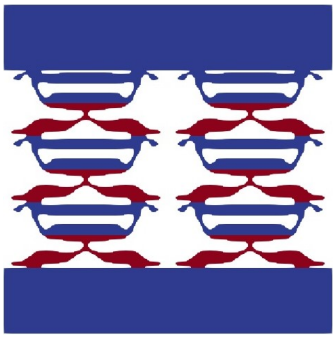
Intermediate	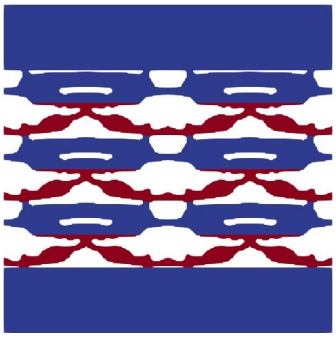	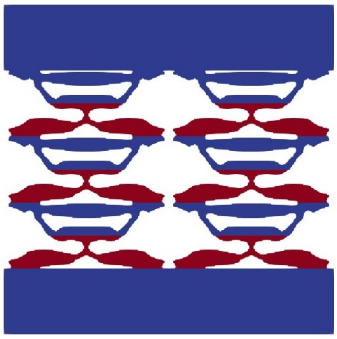	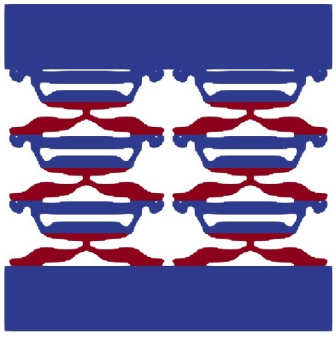
Dilated	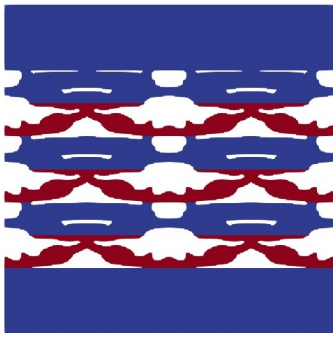	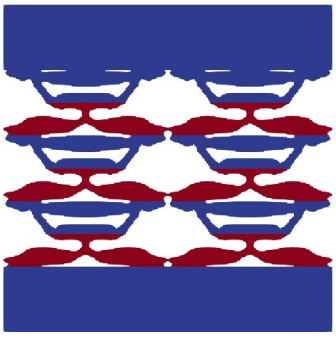	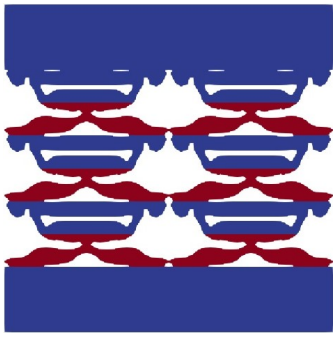

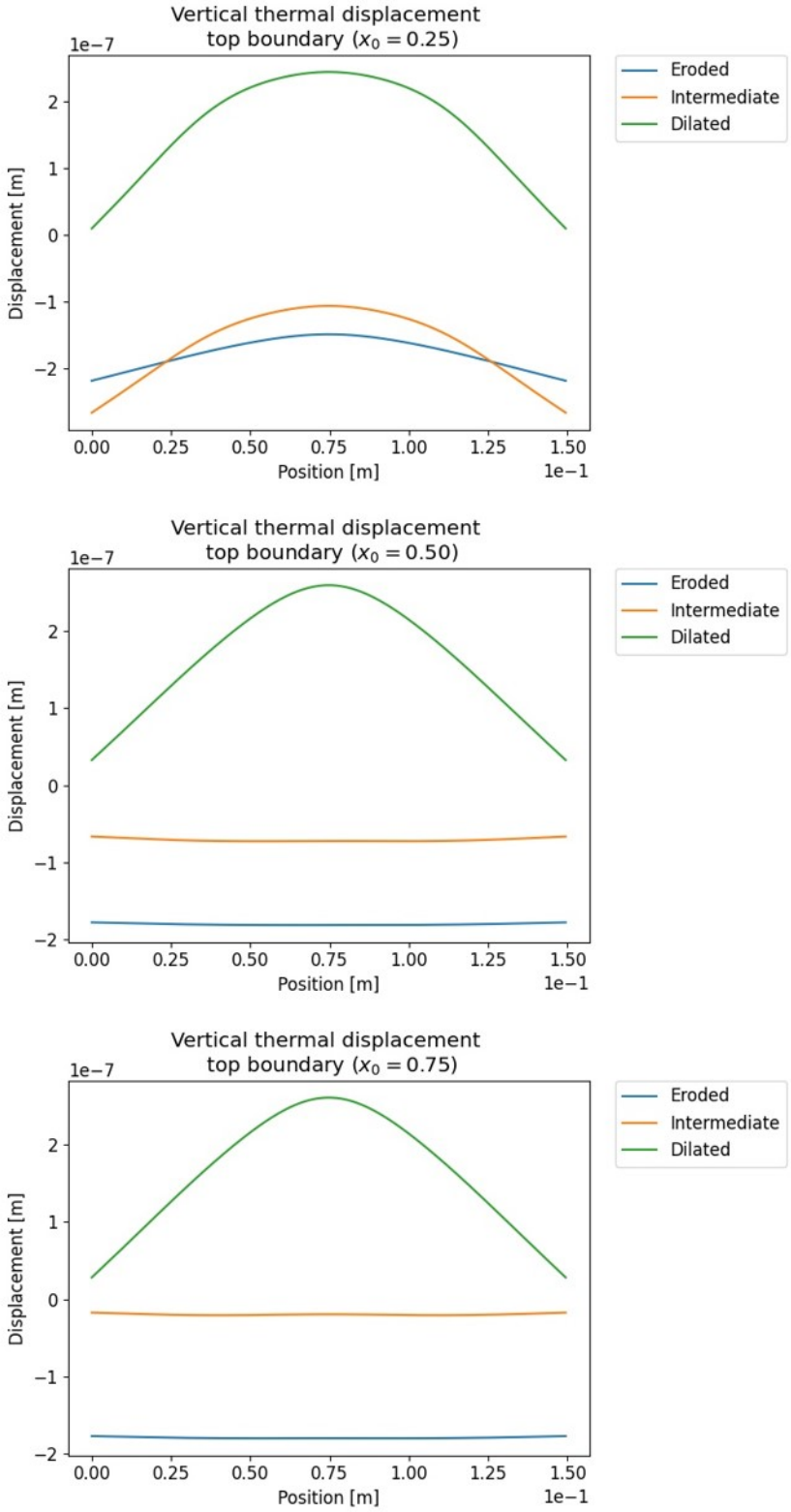

Figure 3-4: Vertical thermal displacements of the top nodes of the unit cell array, for the verification cases initialized using $x_0 = 0.25$, $x_0 = 0.50$ and $x_0 = 0.75$.

Chapter 4

Numerical Validation

Chapter 4 presents the numerical validation of the proposed TO framework. First, the considered research questions are presented in Section 4-1, which will be chronologically treated in Sections 4-2 till 4-4. Finally, conclusions based on the numerical validation are presented in Section 4-5.

4-1 Motivation

The new TO framework should address the optimization of thermoelastic metamaterials and structures of finite size, as has been discussed in Section 1-3. In the TO framework, the analysis of finite thermoelastic metamaterial structures is done using the superelement method. Opposed to the homogenization method, the superelement method allows for the analysis of finite unit cell arrays without assuming an infinite repetition of the unit cells. Qiu et al. (2009) [84] already demonstrated that the optimal topology of a periodic unit cell design with maximum structural rigidity, obtained using a TO formulation in which a finite unit cell array is analysed using the superelement method, is dependent on the number of unit cells of the periodic structure. The question that remains is how the thermal response of a thermoelastic metamaterial structure is influenced by the number of unit cells of the structure and whether a superelement approach is more appropriate than the commonly used homogenization method. Hence, the following research question arises:

RQ1. How does the thermal behaviour of a finite thermoelastic unit cell array relate to the number of periodic unit cells used in the thermoelastic structure?

In order to obtain black and white solutions with a minimum length scale and which are manufacturing tolerant, the robust formulation [74] has been implemented in the new TO framework. The effectiveness of the robust formulation for these purposes has already been shown in Wang et al. [74]. In order to verify the effectiveness of the robust formulation in the TO framework for thermomechanical metamaterial structures, the following research questions should be answered:

RQ2. Are black and white solutions obtained in the newly proposed TO framework?
RQ3. Is minimum length scale control obtained in the newly proposed TO framework?
RQ4. Are manufacturing tolerant designs obtained in the newly proposed TO framework?

Finally, for the purpose of experimental validation, the behaviour of a 3D sample of the optimized design manufactured using available manufacturing techniques should be studied numerically. Although we have tried to limit the differences between the optimized design and the manufacturable design, certain discrepancies will remain. These discrepancies are a result of the 2D simplification and the simplified material layer bonding used in the optimization procedure. Furthermore, the impact of the post-processing step for the optimized design is decreased in the proposed TO framework, but not fully eliminated. Thesholding densities and interpolating curves remains necessary, although their influence most likely is less prominent due to the implementation of the robust formulation. The following research question arises that should be answered before conducting the physical experiment:

RQ5. What behaviour is expected for a manufactured 3D sample, given the available manufacturing techniques?

4-2 Array size effects on thermoelastic response

4-2-1 Method

The homogenization theory used in existing TO frameworks for thermoelastic metamaterials assumes an infinite repetition of the periodic unit cell in the thermoelastic metamaterial. In practise only finite unit cell arrays can logically be realized. Due to the assumption of infinitely repeating unit cells, the homogenization theory might not give realistic results for the optimization of finite unit cell arrays, especially if the number of unit cells in the metamaterial structure is small. In order to answer **RQ1** the thermal behaviour of the optimized unit cell array resulting from the verification cases initialized using $x_0 = 0.75$ is studied, both using the homogenization theory and using the superelement method. This topology is selected for the experimental validation, as will be further discussed in Section 4-4. It should be noted that the superelement method produces exactly the same results as a full Finite Element Analysis (FEA) and is used only in order to reduce the computational costs. The following steps are performed for the comparison of both methods:

1. The effective material properties of the optimized thermoelastic metamaterial are determined using the homogenization theory.
2. The vertical thermal displacement of the top boundary of the unit cell array is computed for the homogenized material properties in a full FEA. The solid top and bottom strips are included in the analysis. The unit cell topologies are substituted by a solid material having the material properties obtained using the homogenization theory.
3. The vertical thermal displacement of the top boundary of the optimized unit cell array is computed using the superelement method. The solid top and bottom strips are included in the analysis. The number of unit cells is equal to number of unit cells used in the optimization.

4. The vertical thermal displacement of the top boundary of the unit cell array is computed using the superelement method, for a larger number of unit cells. The overall dimensions of the unit cell array and the solid strips are unchanged. Furthermore, the topology of the optimized unit cell is unchanged. Only the number of unit cells of the unit cell array is increased.

4-2-2 Results

The results of the analysis, performed on the topology resulting from the verification case initialized using $x_0 = 0.75$, are presented in Figure 4-1. It can be seen that the vertical thermal top displacement obtained using both methods differ significantly, especially for a small unit cell array size. The percent differences between both methods for the vertical thermal displacement of the top boundary of the unit cell, are presented in Table 4-1. In the presented verification case, a unit cell array of 2 x 3 unit cells was optimized. The difference between both methods, for the vertical thermal displacement of the top boundary for this unit cell array size, is larger than 100 %.

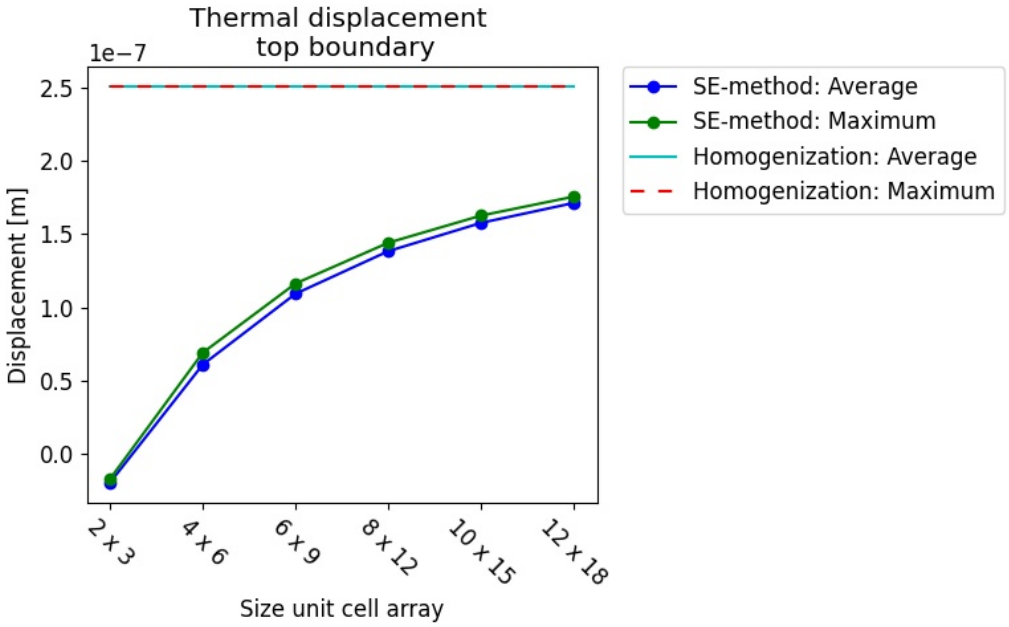

Figure 4-1: Average and maximum vertical thermal displacement of the top boundary of the unit cell array, computed using the homogenization theory and the superelement method. Unit cell array size refers to the number of periodically repeated unit cells, so excluding the solid strips.

Table 4-1: Percent difference of the vertical thermal displacement of the top boundary of the unit cell, for the superelement method compared to the homogenization theory.

Array size	2 x 3	4 x 6	6 x 9	8 x 12	10 x 15	12 x 18
Average	-108.0%	-75.8%	-56.5%	-44.9%	-37.1%	-31.7%
Maximum	-107.0%	-72.6%	-53.7%	-42.6%	-35.2%	-30.0%

It can be seen that for a larger number of unit cells, the vertical thermal expansion of the top boundary computed using the superelement method moves towards the vertical thermal expansion of the top boundary computed using the homogenization theory. A rational polynomial fit is applied to the results obtained using the superelement method, presented in Figure 4-1. Extrapolation of the fitted curve shows that the difference between the superelement method and the homogenization method is smaller than 5 %, for a unit cell array size of 98 x 147 and 120 x 180, for the average and maximum displacement values, respectively.

The homogenization theory is commonly used in existing TO frameworks for thermoelastic metamaterials. Small thermoelastic unit cell arrays are however most often manufactured, since the fabrication of large unit cell arrays remains difficult. The superelement method accounts for the size of the unit cell array and gives a significantly different and more realistic thermoelastic response for small unit cell arrays, compared to the commonly used homogenization theory, whilst still maintaining acceptable computational costs.

4-3 Manufacturable designs

4-3-1 Method

In order answer research questions **RQ2**, **RQ3** and **RQ4** the results of the verification cases presented in Section 3-3 are studied. Both **RQ2** and **RQ3** can be answered by visually inspecting the results of the verification cases in more detail. In Wang et al. [74], it is already shown that manufacturing tolerant designs are obtained using the robust formulation, if the same topology is obtained for the eroded, intermediate and dilated designs. Research question **RQ4** can thus be answered by comparing the eroded, intermediate and dilated designs, which should have the same topology in order to ensure that the design is manufacturing tolerant.

4-3-2 Results

Black and white solutions

The projected density fields of the intermediate topologies for the verification cases, should be used as blue-prints for the final designs [74]. These topologies show only a very small gray transition region between the solid and void phases, as can be seen in Table 4-2. For the verification cases initialized using $x_0 = 0.50$ and $x_0 = 0.75$, small gray areas are however observed at the location where the eroded, intermediate and dilated designs differ locally. Near black and white solutions are thus obtained, with only very small transition regions between the solid and void phases and small gray areas at the location where the eroded, intermediate and dilated topologies vary locally.

Table 4-2: Intermediate projected density fields for the final topologies of the verification cases.

	Projected density field intermediate topology $(\widetilde{\bar{x}}_1)_{\mathrm{i}}$
$x_0 = 0.25$	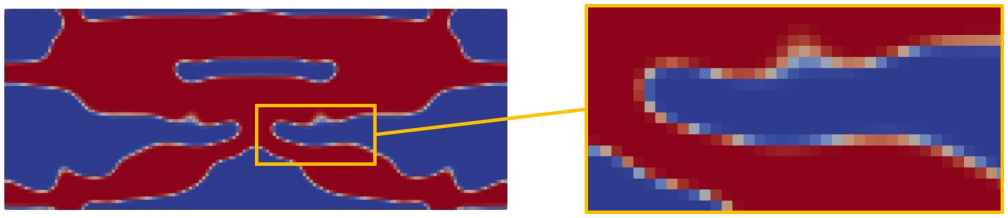
$x_0 = 0.50$	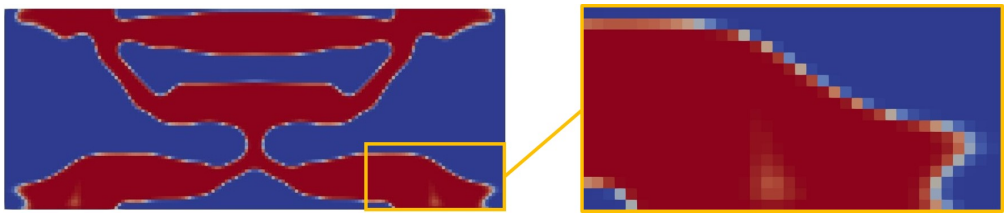
$x_0 = 0.75$	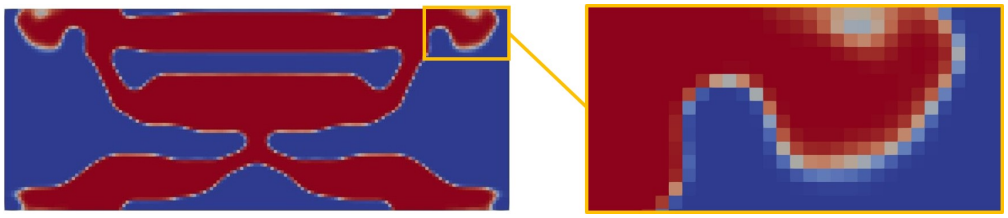

Length scale control

The parameters related to the robust formulation, presented in Table 3-5, are chosen such that a minimum length scale of 2 mm is to be obtained for the optimized topology. Using the filter domain extension approach, presented in Section 2-3-1, minimum length scale control should also be established at the interface between different unit cells. Since the filter domain extension used is not valid for the outer boundary of the unit cell array, where the unit cells do not adjoin to other unit cells having the same topology, minimum length scale control is not obtained at these boundaries. The outer boundary of the unit cell array, where the filter approach is not valid, is indicated with a green dashed line in Figures 4-2, 4-3 & 4-4.

The minimum length scale control for the optimized topologies resulting from the verification cases, is discussed using Figures 4-2, 4-3 and 4-4. For the verification case initialized using $x_0 = 0.25$, it was observed that the eroded, intermediate and dilated topologies are the same. Studying the optimized topology of the unit cell array presented in Figure 4-2, it can be seen that a minimum length scale of 2 mm is indeed established for the interior of the unit cell array on both the solid and void phase. Along the outer boundary of the unit cell array, minimum length scale control is not established. For the top and bottom of the outer boundary, where the unit cell array adjoins to the solid strips, it can be seen that void regions are obtained with a length scale smaller than 2 mm. For the left and right side of the outer boundary, minimum length scale control is not obtained for the solid phase, since the edges of the solid phase are not rounded. This does however not compromise the manufacturability of the optimized unit cell array.

The eroded, intermediate and dilated designs of the verification cases initialized using $x_0 = 0.50$ and $x_0 = 0.75$ vary locally, as can be seen in Table 3-8, which could compromise the minimum length scale control. In Figure 4-3, it can however be seen that minimum length scale control is still obtained for the interior of the unit cell array initialized using $x_0 = 0.50$. For the verification case initialized using $x_0 = 0.75$, it can be seen that a minimum length scale of 2 mm is also satisfied for the interior of the unit cell array, except for the locations where the eroded, intermediate and dilated topologies differ. For both cases, minimum length scale control on the void phase is again not obtained at the top and bottom of the outer boundary of the unit cell array, which adjoins to the solid strips. Both designs have no solid material near the left and right side of the outer boundary. The minimum length scale control near the left and right side of the outer boundary is therefore not compromised.

In conclusion, it is observed that minimum length scale control is obtained for the proposed TO formulation, using the robust formulation combined with a filter domain extension approach. Along the outer boundary of the unit cell array, where the used filter domain extension approach is not valid, minimum length scale control is however not guaranteed. Differing eroded, intermediate and dilated topologies for the robust formulation can furthermore compromise the minimum length scale control, as observed for the verification case initialized using $x_0 = 0.75$.

Manufacturing tolerant designs

A condition presented in Wang et al. [74], which is to be satisfied to obtain topologies robust towards constant erosion and dilation over the entire topology, is that the eroded, intermediate and dilated designs share the same topology. When the topologies are the same, manufacturing error bounds are obtained which are defined by the difference between the topologies. For the verification case initialized using $x_0 = 0.25$ the eroded, intermediate and dilated topologies are indeed the same, as can be seen in Table 3-8. Therefore, the topology initialized using $x_0 = 0.25$ is robust towards manufacturing uncertainties. This is however not true for the topologies initialized using $x_0 = 0.50$ and $x_0 = 0.75$, for which the eroded, intermediate and dilated topologies differ locally. Robustness towards constant erosion or dilation over the entire topology can thus be obtained for the new TO framework. Robustness is however not guaranteed, when the eroded, intermediate and dilated topologies differ.

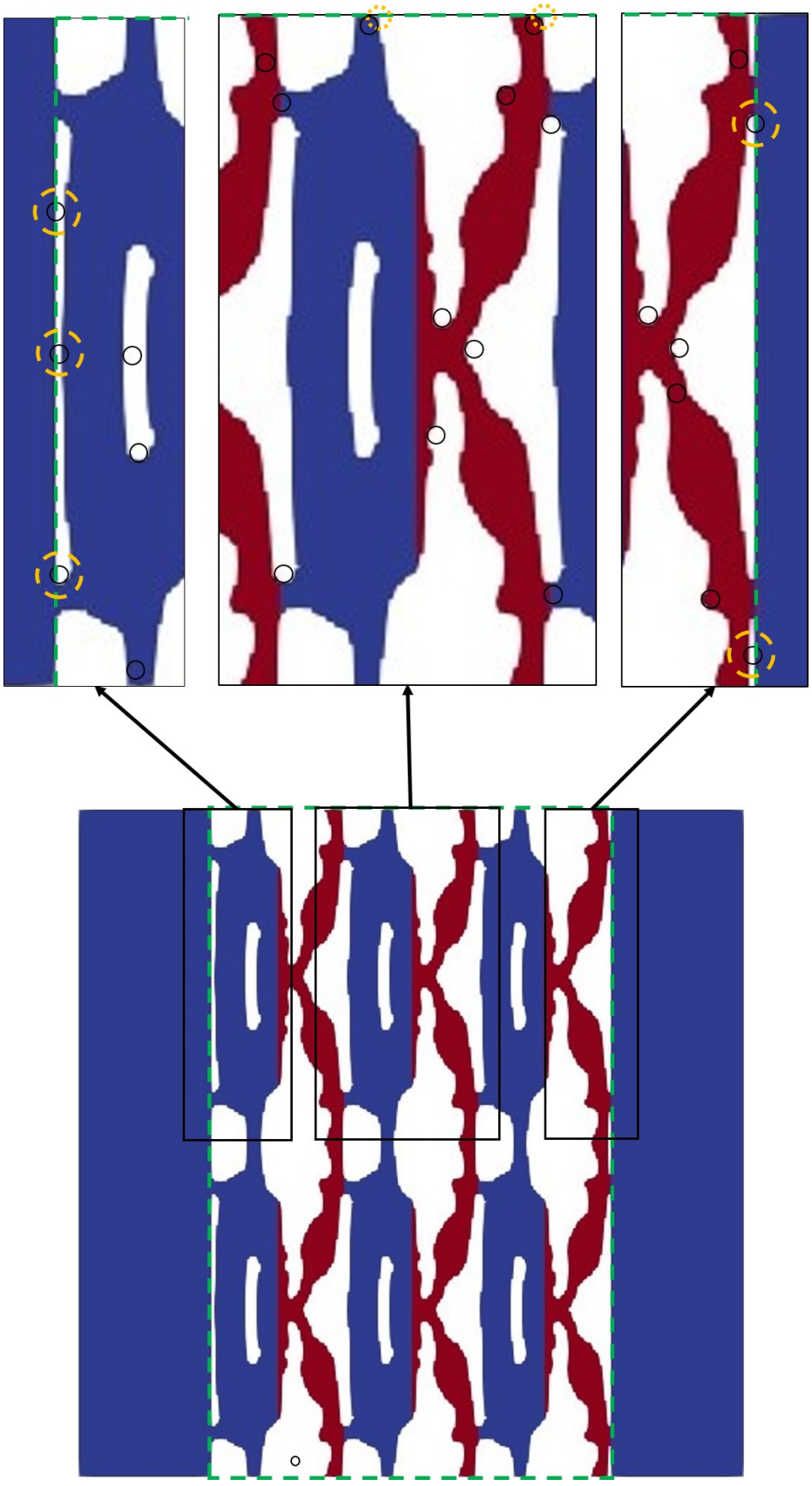

Figure 4-2: Intermediate projected density field for the optimized design ($x_0 = 0.25$) from aluminium (blue) and steel (red) material, using a threshold of 0.5 on the projected density field for the visualization. The outer boundary of the unit cell array is marked with a green dashed line. The black circles visualize a length scale of $2\,\mathrm{mm}$. The dashed orange circles highlight locations where the minimum length scale is not satisfied.

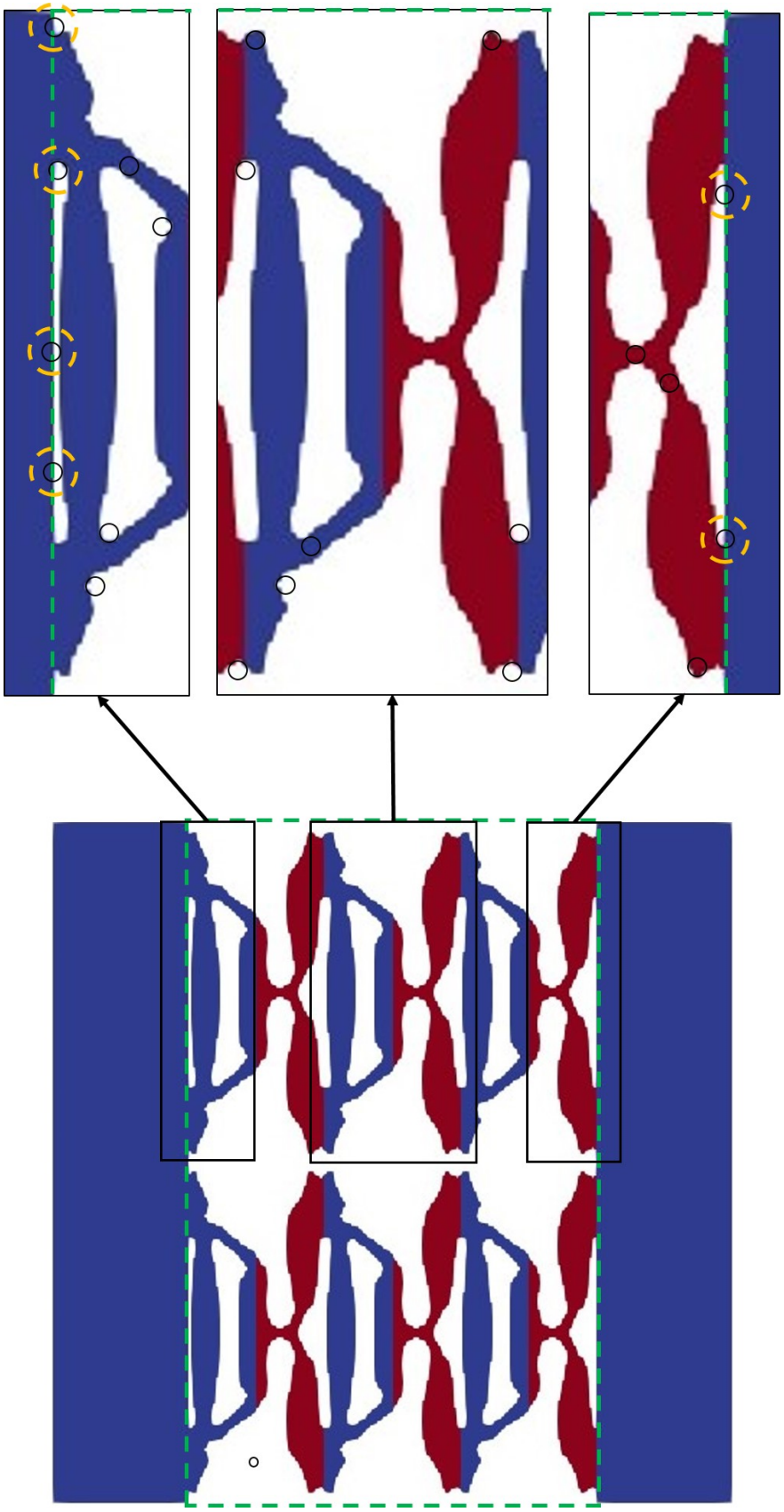

Figure 4-3: Intermediate projected density field for the optimized design ($x_0 = 0.50$) from aluminium (blue) and steel (red) material, using a threshold of 0.5 on the projected density field for the visualization. The outer boundary of the unit cell array is marked with a green dashed line. The black circles visualize a length scale of $2\,\mathrm{mm}$. The dashed orange circles highlight locations where the minimum length scale is not satisfied.

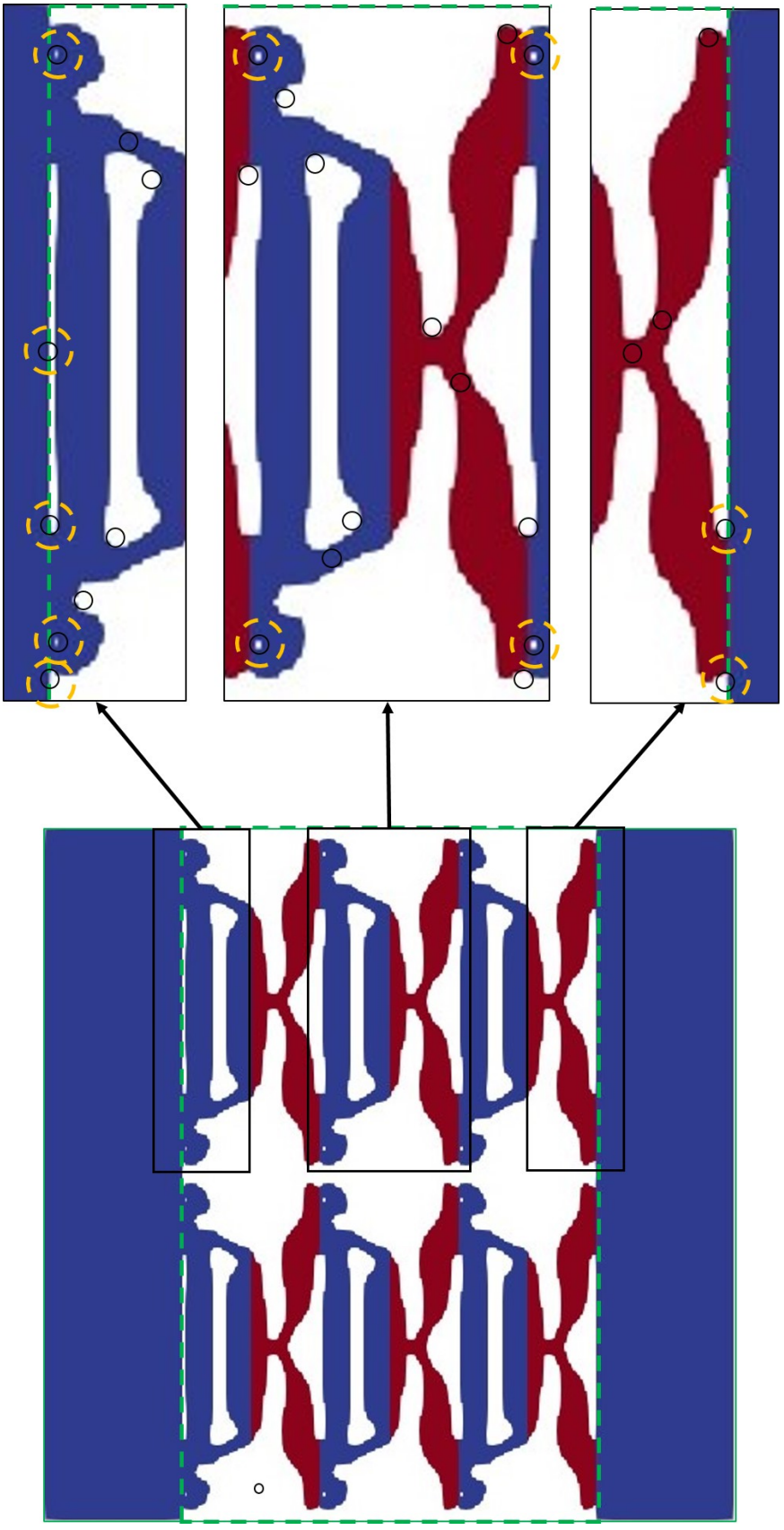

Figure 4-4: Intermediate projected density field for the optimized design ($x_0 = 0.75$) from aluminium (blue) and steel (red) material, using a threshold of 0.5 on the projected density field for the visualization. The outer boundary of the unit cell array is marked with a green dashed line. The black circles visualize a length scale of $2\,\mathrm{mm}$. The dashed orange circles highlight locations where the minimum length scale is not satisfied.

4-4 Physical testing simulation

4-4-1 Topology selection

As elaborated in Section 4-3, minimum length scale control and robustness are not obtained for the verification cases initialized using $x_0 = 0.50$ and $x_0 = 0.75$. Nevertheless, the topology resulting from the verification case initialized using $x_0 = 0.75$ will be used for experimental validation of the TO framework. The relatively small contact area between the material layers in the topology of the verification case initialized using $x_0 = 0.25$, will introduce a risk of failure during experimental validation due to the used adhesive connection. Improvements on the TO framework, presented in Section 6-2, address this problem. The final iteration of the verification case initialized using $x_0 = 0.50$ does not meet the MSE constraint. Therefore, experimental validation is performed using the case initialized with $x_0 = 0.75$.

4-4-2 Method

In order to simulate the behaviour of the optimized topology during the experiment, a 3D FEA is performed. The post-processed optimized topology of the verification case initialized using $x_0 = 0.75$ is used for this purpose, which has been extruded 15 mm, since the physical sample will be given this thickness. In contrast to the analysis used during the optimization, an adhesive bonding will be modelled between the different material layers. Symmetry is used for the 3D FEA, in order to reduce the computational costs. The Boundary Conditions (BCs), mesh and material properties used in the FEA are provided in Appendix D. The topology is subjected to a uniform temperature increase from 22 °C to 45 °C. The same analysis is repeated for a steel block of similar size. The results of both 3D FEA will be compared.

4-4-3 Results

The displacement contours visualizing the vertical displacement of the optimized topology and the reference steel block are given in Figure 4-5. The vertical displacement of the top boundary of both samples are visualized in Figure 4-6. From both figures it can be seen that the vertical thermal displacement for the top boundary of the optimized sample varies only slightly over the sample's width. The minimum, maximum and average top displacements of both samples are presented in Table 4-3. It can be seen that the vertical thermal expansion is much smaller for the optimized topology than for the reference steel sample, hence it is expected that a clear difference between the vertical thermal expansion of both samples can be observed in the experiment, assuming that the quality of the manufactured samples is adequate. Furthermore, it is observed from the 3D FEA that the obtained stresses are well below the yield stresses for the materials. The strain in the adhesive layers is also well below the adhesive's strain at break. Hence, no failure is expected for the optimized sample for the load case used in the experiment. Stress and strain contour plots are given in Appendix D.

Table 4-3: Vertical thermal top displacements obtained from the 3D FEAs.

	Average [µm]	Minimum [µm]	Maximum [µm]
Optimized topology	0.976	0.955	1.007
Steel reference	41.0	41.0	41.0

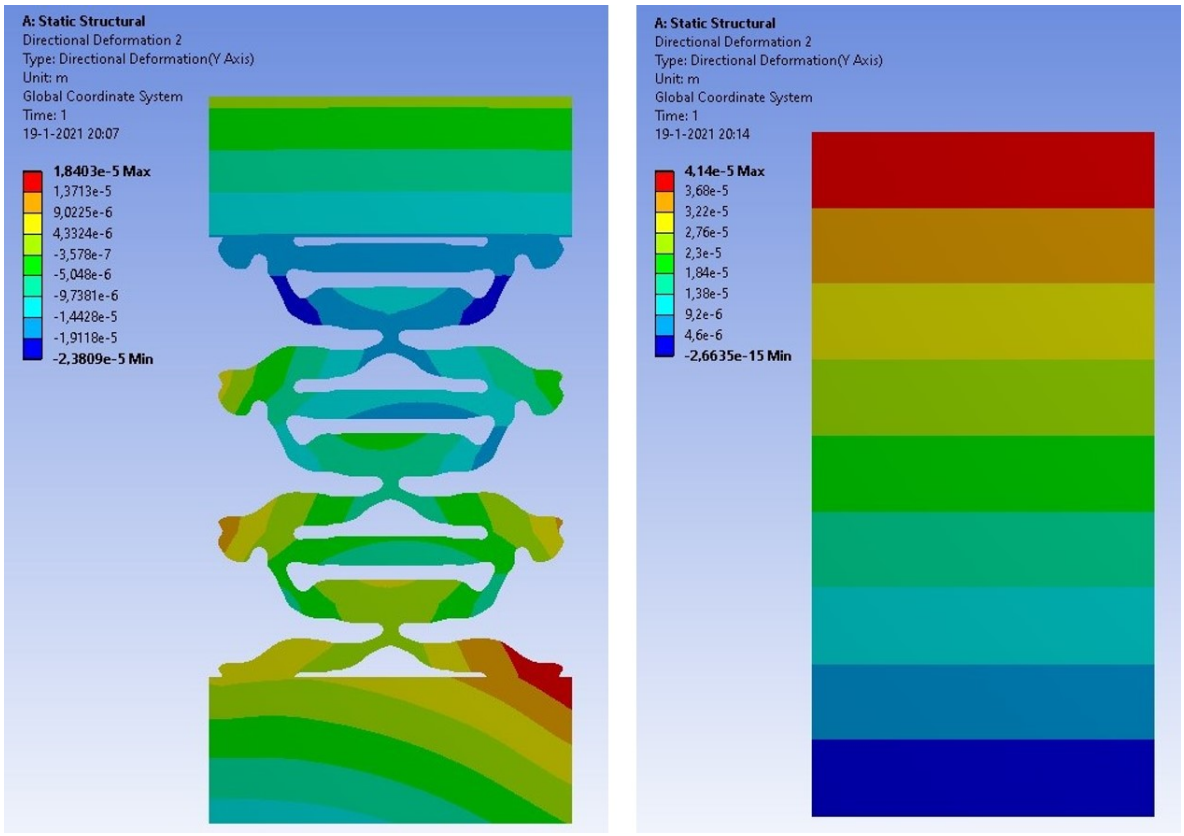

Figure 4-5: Displacement contours projected on the undeformed geometry, visualizing the vertical thermal displacement for the loadcase modelling the physical experiment. The contours are projected only on one half of the samples, since symmetry conditions are used in the analysis. Given displacement values are in meters. More details on the FEA are provided in Appendix D.

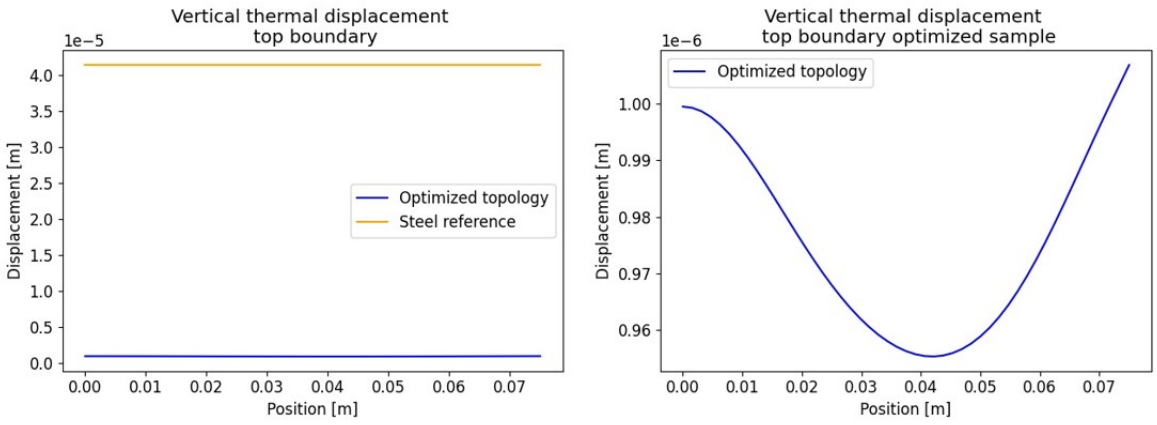

Figure 4-6: Vertical thermal displacement of the top boundaries for the optimized topology and the steel reference, resulting from the 3D FEA. Vertical thermal displacement of the top boundary of the steel reference is constant over its width.

4-5 Conclusions

The conclusions which can be drawn from the numerical validation, will be presented by answering the research questions introduced in Section 4-1.

RQ1. How does the thermal behaviour of a finite thermoelastic unit cell array relate to the number of periodic unit cells used in the thermoelastic structure?

From the results presented in Section 4-2, it can be seen that the vertical thermal top displacement of a finite unit cell arrays is clearly dependent on the number of unit cells used. For a unit cell array consisting of 2 x 3 unit cells, the number of unit cells used in the verification cases, the vertical thermal top displacement computed using the superelement method differs significantly from the displacement obtained using the commonly applied homogenization method and is more than 100 % lower. For a larger number of unit cells, the computed displacement using the superelement method moves towards the displacement computed using the homogenization method. Utilizing extrapolation, it is however observed that the difference between the maximum vertical thermal displacement of the top boundary of the unit cell array, computed using both the homogenization method and the superelement method, is not smaller than 5 % for a unit cell array size smaller than 120 x 180. Concluding, the number of unit cells used in a thermoelastic unit cell array influences the thermal behaviour of the structure significantly. Only small thermoelastic unit cell arrays are often manufactured. Especially for a small number of unit cells, the superelement method is more suitable for the analysis of the structure compared to the commonly used homogenization method, since it takes into consideration the number of unit cells used, whilst still maintaining acceptable computational costs.

RQ2. Are black and white solutions obtained in the newly proposed TO framework?

From the results presented in Section 4-3-2, it can be seen that near black and white solutions are obtained in the TO framework. Small transition regions between solid and void material can however still be seen, but their width is small compared to the typical width of the transition regions expected without the use of the robust formulation. Small gray areas are additionally observed at the locations where the eroded, intermediate and dilated designs differ.

RQ3. Is minimum length scale control obtained in the newly proposed TO framework?

It can be seen from the results presented in Section 4-3-2, that minimum length scale control has been established at the interior of the unit cell array for the verification case initialized using $x_0 = 0.25$. The cases initialized using $x_0 = 0.50$ and $x_0 = 0.75$ show locally varying topologies for the eroded, intermediate and dilated designs. For the case initialized using $x_0 = 0.75$, minimum length scale control has therefore not been established at the location where the topologies vary. Minimum length scale control is not obtained at the outer boundary of the unit cell array for the new TO framework, since the used filter domain extension approach is not valid for the outer boundary. Concluding, minimum length scale control can be established at the interior of the unit cell array for the proposed TO framework, although it requires the eroded, intermediate and dilated topologies to be the same. Minimum length scale control at the outer boundary of the unit cell array is not established.

RQ4. Are manufacturing tolerant designs obtained in the newly proposed TO framework?

In order to obtain manufacturing tolerant designs with the robust formulation, which is applied in the proposed TO framework, the eroded, intermediate and dilated designs should have the same topology [74]. As discussed in the conclusion of **RQ3**, this is not the case for all verification cases. The TO framework is thus able to obtain manufacturing tolerant designs, but manufacturing tolerant designs are not guaranteed when different eroded, intermediate and dilate topologies are obtained.

RQ5. What behaviour is expected for a manufactured 3D sample, given the available manufacturing techniques?

From the performed 3D FEA presented in Section 4-4, it is observed that the vertical thermal expansion of the optimized topology is expected to be considerably lower than the vertical thermal expansion of a steel reference sample. Assuming adequate production of the optimized topology is established, it is therefore expected that a considerable difference in thermal expansion can be observed in the experiment for the optimized topology compared to the steel reference sample. The stress and strain values obtained from the 3D FEA of the optimized topology are furthermore well below critical values and hence no failure of the optimized topology due to thermal loads is expected during the experiment.

Chapter 5

Experimental validation

In order to experimentally validate the newly proposed TO framework, the unidirectional thermal expansion of a physical sample of the optimized design is quantified and compared to the thermal expansion of a steel reference sample. First, the motivation and research questions for the experimental validation are presented in Section 5-1. Then, the manufacturing process and the resulting manufactured physical sample of the optimized design will be discussed in Section 5-2. Next, the experimental procedure and setup will be described in Section 5-3. Finally, the results of the experimental validation are presented in Section 5-4 and conclusions are given in Section 5-5. In conclusion, it is shown that the optimized design is manufacturable and that its unidirectional thermal expansion is lower than the CTE of its constituents.

5-1 Motivation

As has been introduced in Section 1-3, existing TO frameworks for thermoelastic metamaterials often do not take into account manufacturability in the TO formulation. The proposed TO framework has been designed to account for manufacturability restrictions in the optimization procedure, which have been discussed in Chapter 2 and Chapter 3. Numerical analysis, presented in Chapter 4, has shown that the unidirectional thermal expansion of the optimized topology using the new TO framework should be considerably lower than the thermal expansion of its constituents. Since manufacturability is the main focus of this research, it should be validated that the optimized design can be manufactured and furthermore that its functionality is as intended. The research questions, that are drafted for the experimental validation of the TO framework, are as follows:

RQ1. Is the optimized design manufacturable?
RQ2. Is the unidirectional thermal expansion of the manufactured optimized design significantly lower than the (unidirectional) thermal expansion of its constituents?

5-2 Fabrication

5-2-1 Process

The production facilities necessary to perform UAM, which was unidentified to be a suitable manufacturing method for thermoelastic metamaterials in Section 1-2-5, were not available for this research. Therefore, an alternative method for the the fabrication of the optimized topology has been chosen, described in Figure 5-4. Similar to the UAM production process used in Parsons [69], a layered solid multi-material block is first manufactured. Subsequently, a substractive manufacturing technique is used to create the voids and to obtain the final topology.

A water and heat resistant adhesive named Araldite ® 2019 has been used to bond the individual material layers. The adhesive has been applied according to manufacturer's instructions and surfaces have been degreased before the adhesive was applied. The adhesive is cured for 1 hour at 130 °C, in a KM-series curing oven of the brand Snijstaal.

Waterjet cutting has been used for the subtracting manufacturing step in the production process, using an OMAX MicroMax® waterjet cutting machine. Opposed to many other subtractive manufacturing techniques, waterjet cutting does not introduce localized heat in the work piece, which prevents the introduction of thermal stresses and warping. Furthermore, waterjet cutting is able to cut sufficiently small features at a relatively fast production rate and is readily available at the TU Delft.

5-2-2 Physical sample

The manufactured physical sample is visualized in Figures 5-1, 5-2 and 5-3. It can be seen that the topology has been manufactured successfully, although the following imperfections are present in the manufactured optimized topology:

- A slight misalignment of the layered solid multi-material block in the waterjet cutting machine has been encountered. An offset of the layered solid multi-material block compared to the outer contour of the topology cut by the waterjet cutting machine is observed, resulting in wrongly situated material in the manufactured sample. This can most clearly be seen by the wrongly situated steel, indicated in Figure 5-1 with red arrows. Additionally, an angular misalignment of the layered solid multi-material block with the outer contour of the topology is observed, as visualized in Figure 5-2. The angular misalignment again results in wrongly situated material in the manufactured sample.
- The finish of the cutting surface is not entirely smooth. The front of the manufactured sample, from which the waterjet perforates the layered solid multi-material block, has a relatively smooth cutting edge. For the rear of the sample, the finish of the cutting edge is however rougher, as can be seen in Figure 5-3.
- Excess adhesive, which squeezed out of the unsolidified material layer bonds during the manufacturing process, is cured on the front and rear of the manufactured samples. The cured adhesive is indicated with a green arrow in Figure 5-1.

It should be noted that the imperfections presented in the bullet points above could influence the thermal response of the metamaterial structure. Especially the misalignment of the outer contours with respect to the material layers might compromise the thermal response of the design, since the working principle of the design is based on the positioning of the different materials in the topology.

It is believed that the encountered imperfections might however be preventable. The alignment of the layered solid multi-material block in the waterjet cutting machine could be done more accurately. Furthermore, since waterjet cutting machines are known to cut steel slabs with thicknesses larger than the cut thickness of 15 mm for our sample, it is believed that a smoother finish could possibly be obtained by adjusting the machine's operating settings or by using a different waterjet cutting machine.

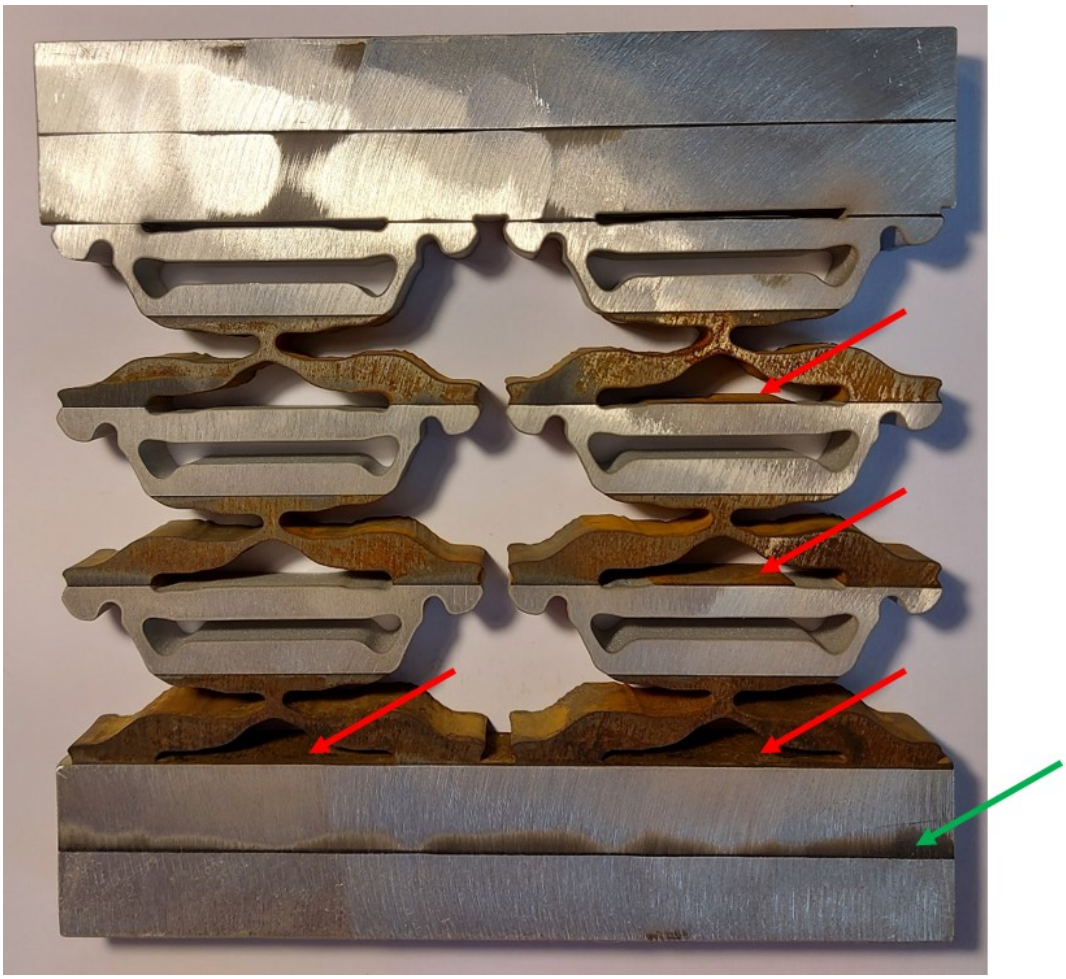

Figure 5-1: Front view of the manufactured thermoelastic metamaterial structure. The front of the sample is the side from which the waterjet perforated the sample. Red: Wrongly situated steel, due to a misalignment of the solid layered multi-material block in the waterjet cutting machine; Green: Excess cured adhesive.

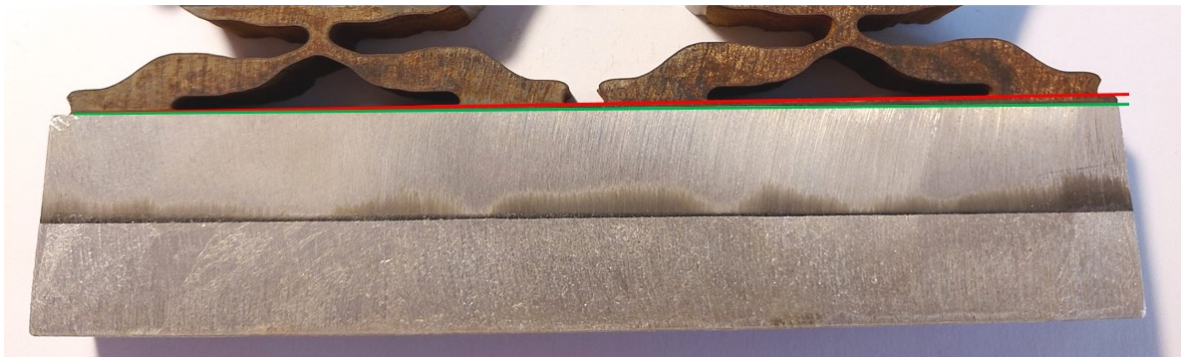

Figure 5-2: Visualization of the misalignment of the solid layered multi-material block in the waterjet cutting machine. Green: Alignment of the material layers in the solid layered multi-material block. Red: Alignment of the outer contour, cut using the the waterjet cutting machine.

Figure 5-3: Visualization of the difference between the surface finish at the front (top) and rear (bottom) of the manufactured sample. The front of the sample is the side from which the waterjet perforated the sample.

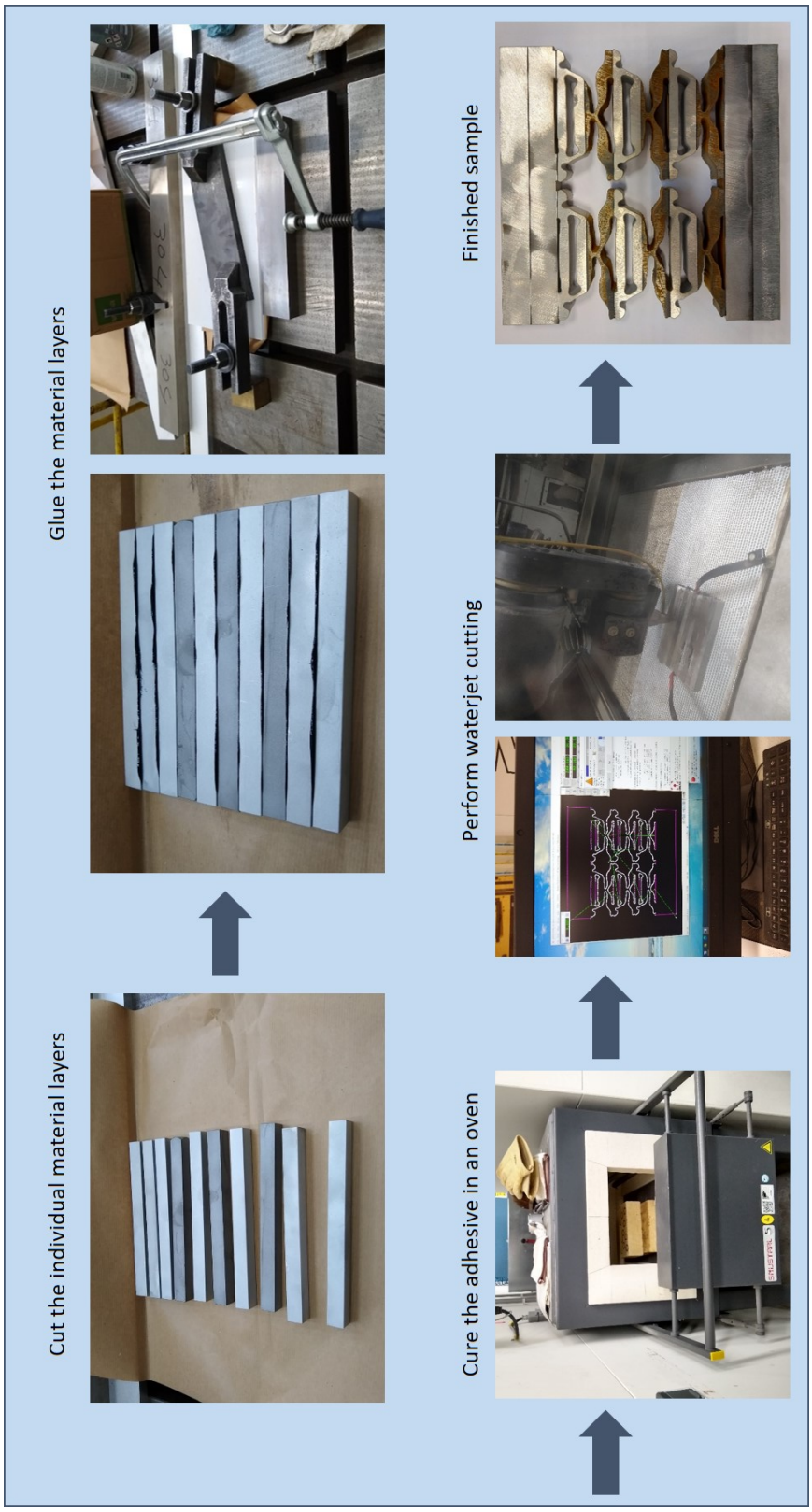

Figure 5-4: Visualization of main components of the fabrication process used for the optimized thermoelastic metamaterial.

5-3 Experiment

Principle

The CTE of the steel constituent is lower than the CTE of the aluminium and adhesive constituents used in the manufactured thermoelastic metamaterial. Therefore, if the unidirectional thermal expansion of the manufactured optimized topology is low compared to the thermal expansion of the steel reference sample, the thermoelastic behaviour of the manufactured sample is tailored successfully. Since the CTE of the steel sample is known, the unidirectional thermal expansion of the optimized sample can furthermore be determined quantitatively.

5-3-1 Setup and process

A schematic and real-world overview of the setup used to quantify the unidirectional thermal expansion of the manufactured optimized topology is given in Figures 5-5 and 5-7. Both samples are placed in a custom made measurement frame, in which the gaps between the top surface of the samples and the sensor heads are measured. The measurement frame and the samples are submerged in hot water, which is left to cool down slowly. The temperature of both the samples and the measurement frame will thus decrease during the measurement. By comparing the change in the sensor gaps for both samples, their unidirectional thermal expansion can be compared qualitatively. The shrinkage of the sample with the lowest CTE will namely be the smallest and hence, the shrinkage of the gap between the sensor attached to the aluminium measurement frame and the sample with the lowest CTE will be the largest.

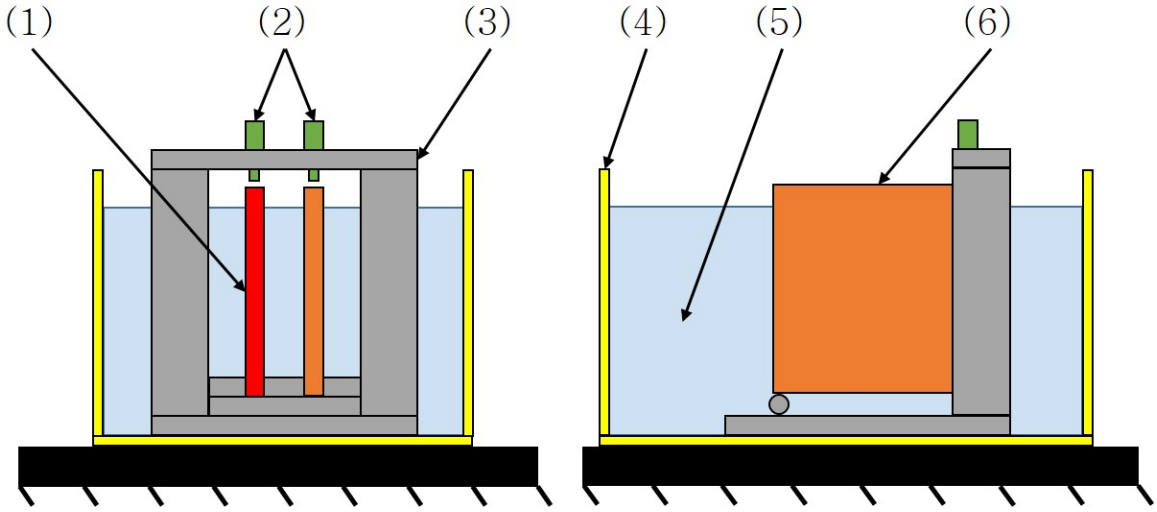

Figure 5-5: Schematic overview of the experimental setup used to determine the unidirectional thermal expansion of the optimized sample. (1) Optimized sample; (2) Fiber optic sensor heads; (3) Custom made aluminium measurement frame; (4) Container; (5) Water; (6) Steel sample.

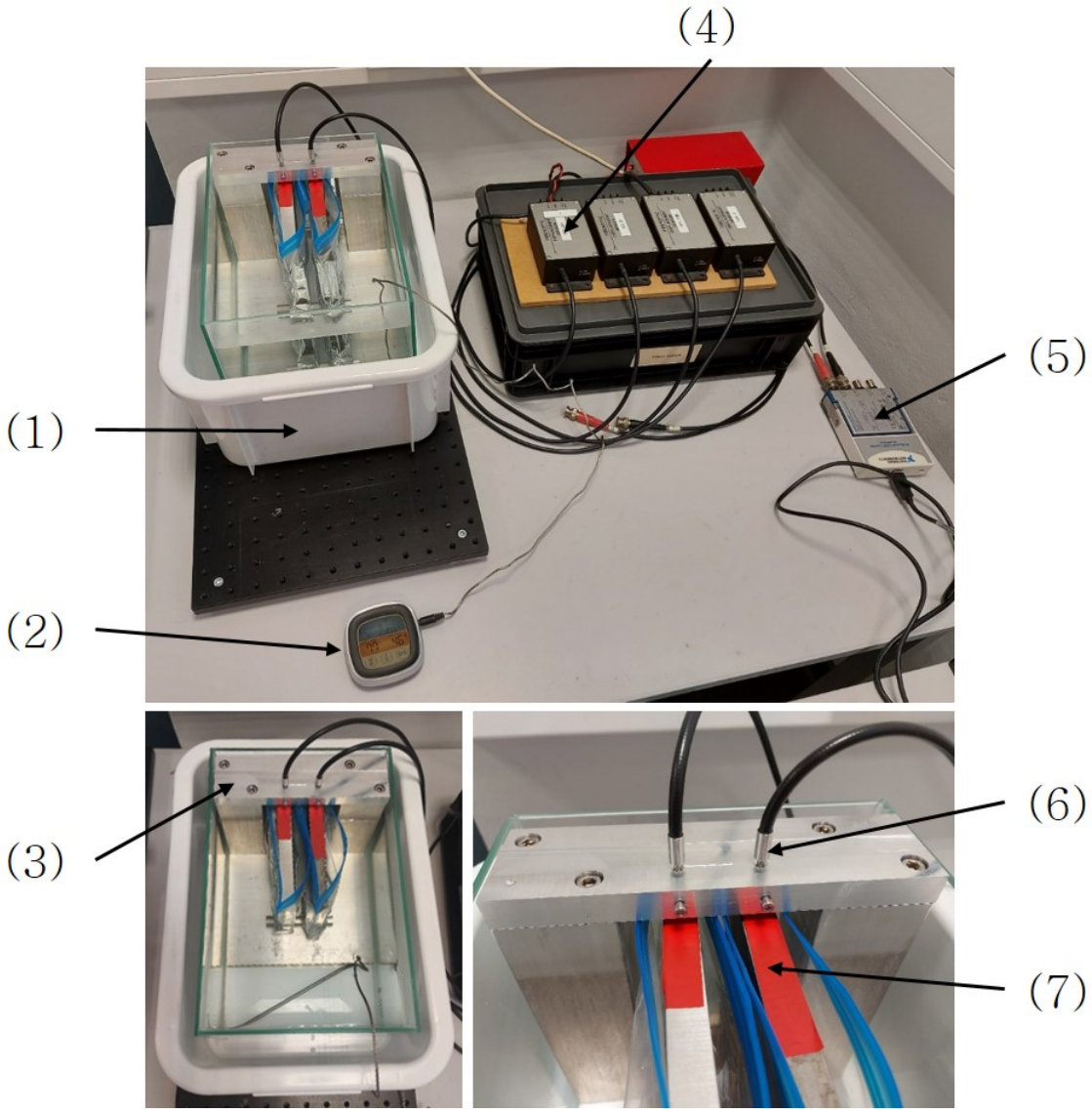

Figure 5-6: Overview of the experimental setup used to determine the unidirectional thermal expansion of the optimized sample. (1) Container; (2) Thermometer; (3) Custom made aluminium measurement frame; (4) Fiber optic sensor amplifier; (5) NI-9215 data acquisition system; (6) Fiber optic sensor head; (7) Tape.

The thermal expansion of both samples is not only compared qualitative, but the unidirectional thermal expansion of the optimized sample is also quantified, which is possible since the CTE of the steel reference sample is known. The following expression is derived for the unidirectional thermal expansion of the manufactured optimized sample, in which we compensate for the parts of both samples that protrude above the water and are therefore possibly not subjected to the temperature change:

$$\alpha_{\text{opt}} = \alpha_{\text{steel}} - \frac{G}{H\Delta T} + \frac{(\alpha_{\text{alu}} - \alpha_{\text{steel}})d_{\text{error}}}{H} \tag{5-1}$$

in which α_{steel} and α_{alu} are the CTE of steel and aluminium, respectively. H is the sample height and ΔT is the temperature change during the experiment. d_{error} is the height of the part of the samples that is not subjected to the temperature change ΔT during the measurement, since it is not submerged in the hot water. Finally, G is the measured difference between the change in the sensor gap for the optimized sample compared to the steel sample. The derivation of Eq. (5-1) is presented in detail in Appendix F.

The measurement frame is custom made from aluminium. The thermal conductivity of aluminium is high, such that a uniform temperature distribution in the measurement frame can be obtained and warping is prevented. The distance sensors are directly mounted to the stiff measurement frame, such that displacements due to the tolerance and creep of mounting components are prevented. The supports for the samples used in the measurement frame are furthermore designed such, that BCs similar to the numerical BCs presented in Figure 3-2 are obtained in the experiment and the positioning of the samples in the measurement frame is reproducible. The custom made aluminium measurement frame is visualized in Figure 5-7.

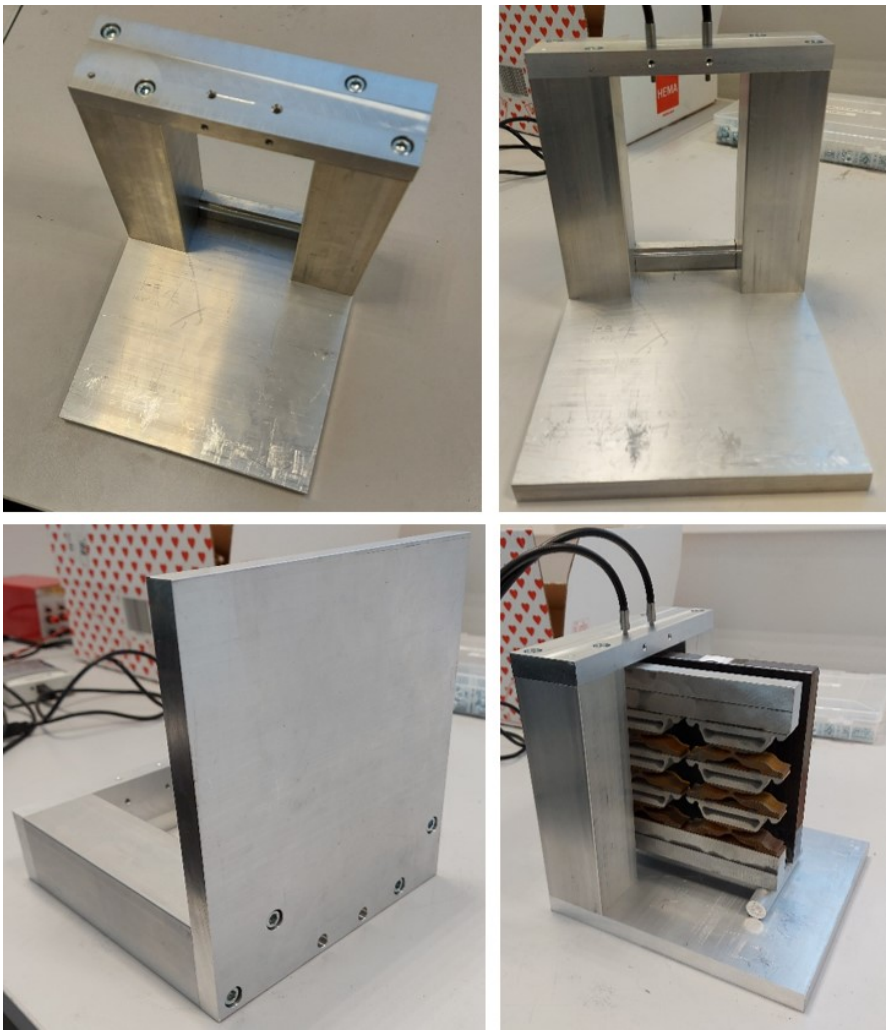

Figure 5-7: Custom made aluminium measurement frame used to determine the unidirectional thermal expansion of the optimized sample.

The aluminium measurement frame is an iteration of a previously used measurement frame, which had multiple unforeseen flaws that caused unreliable and non-repeatable measurements. Measurements were found to be dominated by the tolerance and creep in linear stages, which were used to mount the distance sensors. Therefore, these mounting components are eliminated in the improved measurement frame. The thermal stability of the previously used measurement frame could furthermore be improved. The used measurement frame therefore is entirely made of the same high conductivity material and furthermore is submerged as much as possible in the heated water environment, to establish a uniform temperature throughout the measurement frame. Finally, the measurement frame is placed within the container to further reduce the effects of instabilities on the performed measurements. The plastic container might for example deform due to rising temperatures and the weight of the water. The measurements will not be influenced by these instabilities, since the measured samples are directly placed on the custom made aluminium measurement frame. A more detailed explanation on the flaws of the initial measurement setup and the validation of the new setup is given in Appendix E.

Non-contact fiber optic sensors (Philtec D63-T) are used to measure the gaps between the sensors and the samples. The linear range of the far side of the fiber optic sensors is used, which has a resolution of less than 1 µm. The sensors are connected to a National Instruments 9215 data acquisition system, such that the analog output signals can be processed and stored on a computer. From the analog output signals of the fiber optic sensors, the change in the gaps between the sensors and the samples can be determined.

The calibration of the used sensors is validated before each measurement is conducted. The analog output of the fiber optic sensors is dependent on the target's reflectively. The reflectively of both targets however varies slightly from point to point due to imperfections on the measurements surfaces. Tape is therefore applied on the measurement surface, to obtain a constant reflectively for the measurement targets. In order to obtain accurate measurements, the analog output value of the sensor at its optical peak should be set to exactly 5 V. This can be done using adjustment screws placed on the sensor amplifier. In order to identify the optical peak, the calibration stage visualized in Figure 5-8 is used, in which a linear stage is used to change the distance between the sensor and the calibration target.

After the calibration of the sensors is finalized, the samples are placed on the measurement frame in plastic bags, to prevent contact between the adhesive bonds and water. Hot water of approximately 50 °C is poured into the container housing the measurement frame and samples. The measurement is started when the water reaches a temperature of approximately 40 °C. The measurement is not started right away, such that the setup and samples have sufficient time to heat up and stabilize before the measurement is started. The cooling rate of the hot water between 40 °C and 30 °C is furthermore relatively low, such that influences caused by differences in thermal conductivity of the samples are decreased and uniform temperature distributions is the samples are obtained. Before the measurement is started at 40 °C, the distance between the sensors and the samples is adjusted, such that the sensors operate in their linear operating range. The measurement is terminated when a water temperature of approximately 30 °C has been reached, which took approximately two hours.

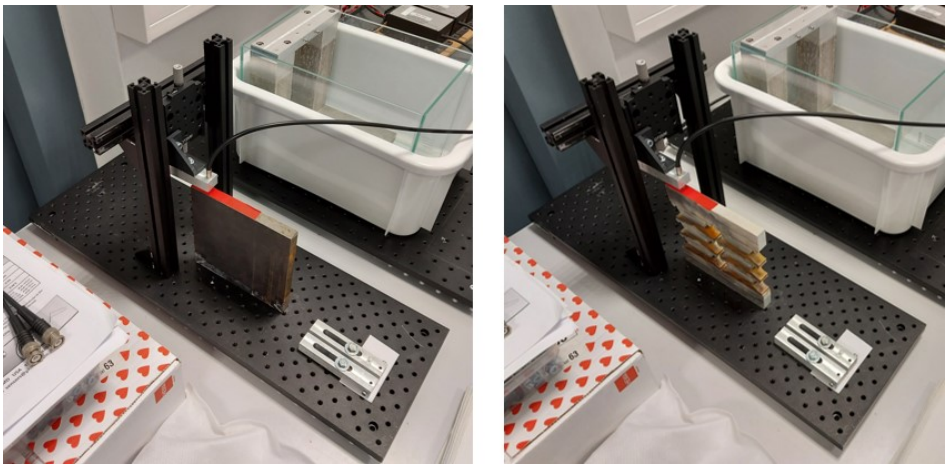

Figure 5-8: Calibration stage for the used fiber optic sensors, in which the fiber optics sensor is mounted to a linear stage.

5-4 Results

The results of the measurements described in Section 5-3, are presented in Figure 5-9. The measured change in the sensor gaps for the final measurement point of the performed measurements are given in Table 5-1.

Table 5-1: Measured change and computed difference for the sensor gaps of the optimized and steel sample, in which positive values indicate an increase of the sensor gap.

Measurement	$\Delta_{\text{gap,opt}}$ [m]	$\Delta_{\text{gap,steel}}$ [m]	G [m]
M1 - 19/02/2021	-34.2×10^{-6}	-9.0×10^{-6}	-25.2×10^{-6}
M2 - 19/02/2021	-35.0×10^{-6}	-9.2×10^{-6}	-25.8×10^{-6}
M1 - 22/02/2021	-31.7×10^{-6}	-6.8×10^{-6}	-24.9×10^{-6}
M2 - 22/02/2021	-34.0×10^{-6}	-5.0×10^{-6}	-29.0×10^{-6}

It can be seen that the sensor gap for the optimized sample $\Delta_{\text{gap,opt}}$ shrinks more than the sensor gap for the steel sample $\Delta_{\text{gap,steel}}$, for all measurements. The unidirectional thermal expansion for the optimized sample, is therefore lower than the unidirectional thermal expansion of the steel sample. The temperature of the samples namely decreases during the measurements. The shrinkage of the sample with the lowest CTE will be the smallest, resulting in a larger decrease of its sensor gap compared to the sample gap of the sample with the highest CTE.

Using the expression presented in Eq. (5-1), which is derived in Appendix F, the unidirectional thermal expansion of the optimized sample can be quantified. For the values and corresponding uncertainties presented in Table 5-2, an effective unidirectional thermal expansion of the optimized sample of $(-4 \pm 8)\,\mu\text{m}/(\text{m}^\circ\text{C})$ is obtained. The values presented in Table 5-2 and their corresponding uncertainties are discussed in Appendix F.

Table 5-2: Parameter values and uncertainty used for the computation of α_{opt}.

Parameter	Value	Description
α_{steel}	$12.0 \times 10^{-6}\,\text{m/(m°C)}$	CTE steel
α_{alu}	$23.6 \times 10^{-6}\,\text{m/(m°C)}$	CTE aluminium
ΔT	$(-10 \pm 1)\,°\text{C}$	Temperature change
H	$(0.150 \pm 0.001)\,\text{m}$	Sample height
d_{error}	$(0.02 \pm 0.02)\,\text{m}$	Height non-heated sample section
G	$(-26 \pm 6) \times 10^{-6}\,\text{m}$	Difference in change of sensor gaps

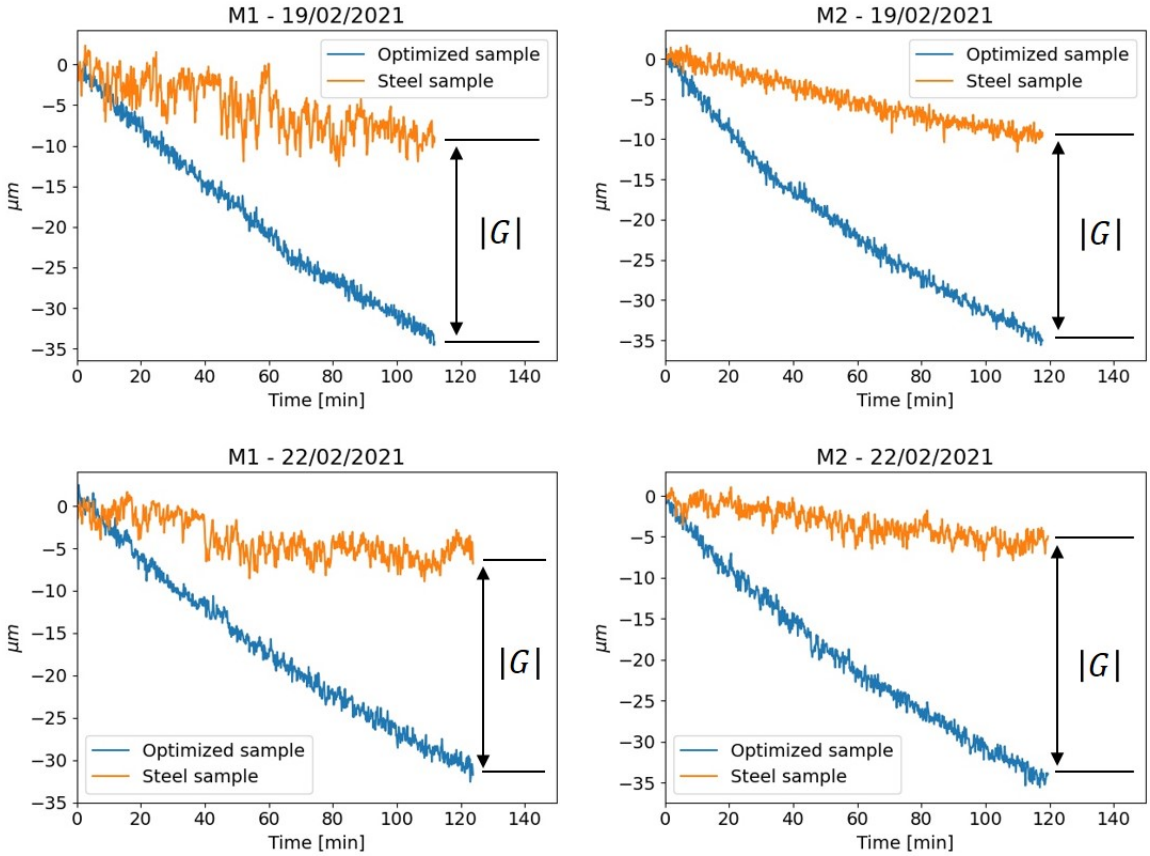

Figure 5-9: Measured change in the sensor gaps for a temperature decrease from $40\,°\text{C}$ to $30\,°\text{C}$. G is the difference between the change in the sensor gaps, for the final measurement point of the measurements.

5-5 Conclusions

The conclusions which can be drawn from the experimental validation, will be presented by answering the research questions introduced in Section 5-1.

RQ1. Is the optimized design manufacturable?

The optimized design has not been manufactured using UAM. Instead an alternative manufacturing method has been used, in which the material layers are bonded using adhesive. The adhesive bonds are however not included in the TO formulation. The small voids in the interior of the optimized unit cell array, highlighted in Figure 4-4, are furthermore not manufactured. Besides these deviations, the optimized design has been manufactured successfully. Multiple imperfections have been identified for the manufactured sample as presented in Section 5-2-2. It is however believed that these imperfections possibly could have been prevented.

RQ2. Is the unidirectional thermal expansion of the manufactured optimized design lower than the (unidirectional) thermal expansion of its constituents?

The constituent with the lowest CTE used in the manufactured optimized design is steel. A measurement setup has been built and verified, used to determine the unidirectional thermal expansion of the optimized sample. For a temperature range between approximately 40 °C and 30 °C, the unidirectional thermal expansion of the optimized sample is lower than the unidirectional thermal expansion of the steel sample. A negative unidirectional thermal expansion of $(-4 \pm 8)\,\mu m/(m°C)$ is obtained for the optimized topology. The newly proposed TO framework thus successfully optimized a manufacturable thermoelastic metamaterial design, with a unidirectional thermal expansion lower than that of its constituents.

Chapter 6

Conclusions and Recommendations

6-1 Conclusions

The aim of this research was the following:

> **The development and validation of a TO framework for the design of (metallic) thermoelastic metamaterials with tuneable thermal expansion, manufacturable by automated manufacturing methods, without the need for extensive post-processing of the optimized design.**

A TO framework is presented in this research, which uses multiple different techniques to improve the manufacturability of the optimized designs. The following techniques were applied in the newly proposed TO framework, aimed at improving the manufacturability of the optimized thermoelastic metamaterial structures:

- The superelement method
- The robust formulation
- A filter domain extension approach

Utilizing these techniques, the following improvements regarding manufacturability are obtained and numerically validated:

- Size effects on the thermoelastic response are accounted for in the new TO framework, which is not done in existing TO frameworks for thermoelastic metamaterials. For small unit cell arrays, the thermoelastic response defers more than 100 % for the used superelement method compared to the commonly used homogenization method. The difference for the computed maximum vertical thermal top displacement of the unit cell array for both methods, is smaller than 5 %, only for array sizes larger than 120 x 180 unit cells. For small thermoelastic unit cell arrays, the superelement method used in the proposed TO framework is therefore more suitable, compared to the commonly used homogenization method, which is not able to account for the large influences of size effects and is therefore inaccurate when analysing small unit cell arrays.

- Realistic boundaries are modelled for the optimized thermoelastic metamaterial structure using the new TO framework, by implementing adjacent solid strips, opposed to assuming disconnected infinite unit cell arrays, as done in the homogenization method.
- Finite thermoelastic unit cell arrays can be optimized for realistic user defined BCs using the proposed TO framework, due to the used superelement method. Frameworks using the homogenization method can only optimize the effective material properties for an infinite unit cell array, for which no realistic user defined BCs can be specified.
- Thermoelastic metamaterial structures can be optimized with near black and white solutions, preventing intermediate densities which cannot be realized practically. It is however not guaranteed that intermediate densities are prevented for the optimized design.
- Minimum length scale control can be performed on the optimized thermoelastic metamaterial structures. The minimum length scale can be chosen based on the intended manufacturing method. It is however not guaranteed that minimum length scale control is obtained for the optimized design. Minimum length scale control is furthermore not enforced for each phase individually and is not established at the outer boundaries of the unit cell array, where the unit cells do not adjoin to other unit cells.
- Manufacturing tolerant thermoelastic metamaterial structures can be optimized, such that robustness of the thermoelastic response towards erosion or dilation during manufacturing is obtained. It is however not guaranteed that manufacturing tolerant designs are obtained.
- Thermoelastic metamaterial structures can be optimized having uniform material layers, such that fabrication using UAM is possible.

The optimized finite thermoelastic structure is manufactured and experimentally validated, from which the followings conclusions can be drawn:

- The finite optimized thermoelastic unit cell array is manufacturable, without extensive post-processing of the optimized design. A few discrepancies were observed for the manufactured design, which most likely could have been prevented.
- A functional thermoelastic structure is optimized and manufactured, exhibiting a unidirectional thermal expansion of $(-4 \pm 8)\,\mu\text{m}/(\text{m}^\circ\text{C})$, which is lower than the unidirectional thermal expansion of its constituents.

It is thus shown that optimized finite thermoelastic structures can be obtained with uniform material layers using the new TO framework, with a unidirectional thermal expansion lower than that of its constituents. The optimized structures can be manufacturing tolerant, near black and white and can have features satisfying a minimum length scale. A functional sample of the optimized structure is manufactured successfully. In conclusion, manufacturable and functional finite thermoelastic metamaterial structures can be designed using the newly proposed TO framework, which require only limited post-processing and are potentially manufacturable using automated manufacturing methods.

6-2 Future work

With respect to the formulation used in the TO framework, the following improvements and extensions could be considered in future work:

- Manufacturing tolerant, black and white optimized designs satisfying a minimum length scale were not obtained for every optimization, due to locally varying eroded, intermediate and dilated topologies. Ideally, the formulation itself should be made more robust, such that robust designs are obtained for every optimization. Otherwise, alternative formulations serving the same purpose might be developed and implemented.
- Minimum length scale control is not established at the outer boundary of the unit cell array. The minimum length scale at the outer boundary can be satisfied by taking a larger minimum length scale for the interior, but this is not desirable. Therefore, a method should be developed to control the same minimum length scale at the interior and outer boundary of the unit cell array simultaneously. A simple but nonideal solution would be to define non-design areas at the boundary of each unit cell.
- Small contact areas at the interface of the different material layers should be prevented, to ensure sufficient contact area for the adhesive connection. This can again be done by using non-design areas, although it considerably limits the design space.
- Minimum length scale control enforced on the individual material phases is desired. This is not as relevant when the manufacturing of the thermoelastic metamaterial is done using UAM or using the method used in this research. However, when a thermoelastic metamaterial structures should be manufactured using DED, length scale control on the individual phases is required to obtain manufacturable optimized designs.
- Designs manufacturable using DMD could be optimized. Besides length scale control on the individual phases, overhang-free designs should furthermore be obtained. This can be done by using a AM filter for print-ready designs presented in Langelaar [93].
- The TO framework can be extended to 3D, which is especially interesting when designs are optimized for DED, since UAM is only suitable for the fabrication of planar designs.
- Optimization of thermoelastic metamaterial structures can be included in the TO framework, for thermal load cases different than the uniform temperature change considered in the current work, such as linear temperature gradients.
- The position and height of the uniform material layers are currently predetermined and could additionally be optimized in the TO.

For the manufacturing of the optimized thermoelastic metamaterial structure, the following topics could be addressed in future work:

- The optimized design is not fabricated using UAM. It would be interesting to practically verify the manufacturability of the optimized design using UAM.
- For the manufacturing method used in this research, multiple processes could be improved to prevent discrepancies between the optimized design and the manufactured design. First of all, the alignment of the layered solid multi-material block in the waterjet cutting could be done more accurately. Furthermore, a study on cutting parameters and machine settings could be conducted, to obtain a smoother finish for the cutting surface on the rear of the sample. Finally, excess adhesive squeezing out of the material bonds could be prevented or removed.

Appendix A

2D Assumptions

Comparison plane-stress and plane-strain assumptions

Since a 2D FEA is used for the analysis of the topology during the TO, either plane-stress or plane-strain assumptions have to be specified. Since only a relatively thin demonstrator will be fabricated of the optimized unit cell array, plane-stress assumptions might be a logical choice. However, since initial results and literature shows that hinges are expected in the optimized topology, the choice for plane-stress conditions is not as obvious. The thickness of the demonstrator can namely be relatively large, compared to the size of the hinge areas. This suggests that for the hinge areas plane-strain conditions might be more accurate. The choice between plane-stress and plane-strain conditions will therefore be based on the analysis of a provisional optimization result. The thermal deformation of the provisional optimized result will be studied for both plane-stress and plane-strain conditions, using the same mesh as used in the TO procedure. Furthermore, a 3D FEA will be performed on the optimized results using a fine mesh. Comparison of the results will show which assumption is most accurate, for the computation of the thermal deformations of the unit cell array.

The unit cell array resulting from the provisional optimization is presented in Figure A-1, together with the 3D model generated for the unit cell array. The temperature change and the BCs used in the analysis are the same as used in the TO, which have been presented in Chapter 3. The unit cell array thus will be subjected to $\Delta T = 1\,^{\circ}\mathrm{C}$ and will be fixed in the left-bottom corner, whilst for the right-bottom corner only the vertical displacement is constrained. The materials used in the provisional unit cell array are however aluminium and titanium, instead of the aluminium and steel material used in the TO discussed in Chapter 3.

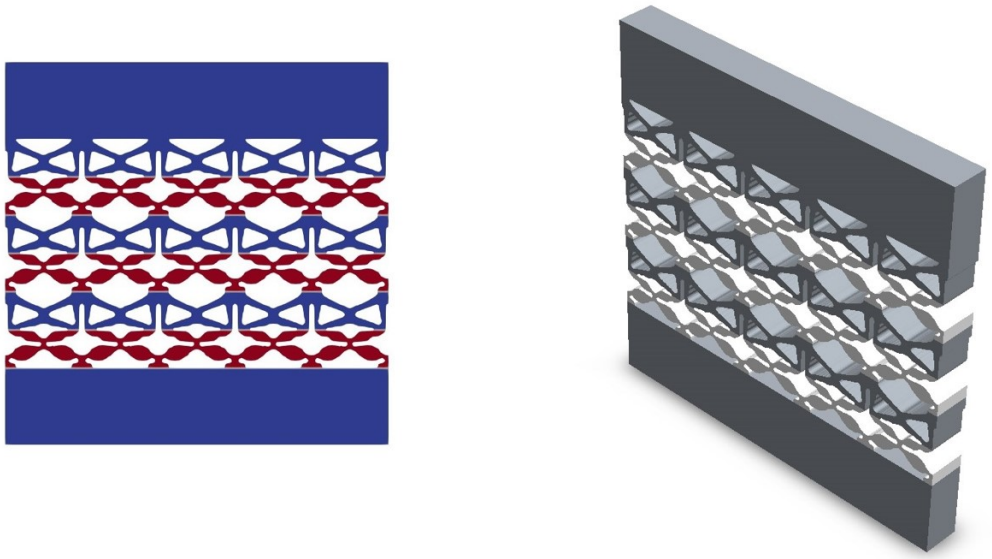

Figure A-1: Unit cell array used in the presented analysis to choose between plane-stress and plane-strain conditions. Left: 2D unit cell array design resulting from the provisional TO, consisting of aluminium (blue) and titanium (red); Right: 3D model generated from the provision unit cell array design, consisting of aluminium (dark grey) and titanium (light grey).

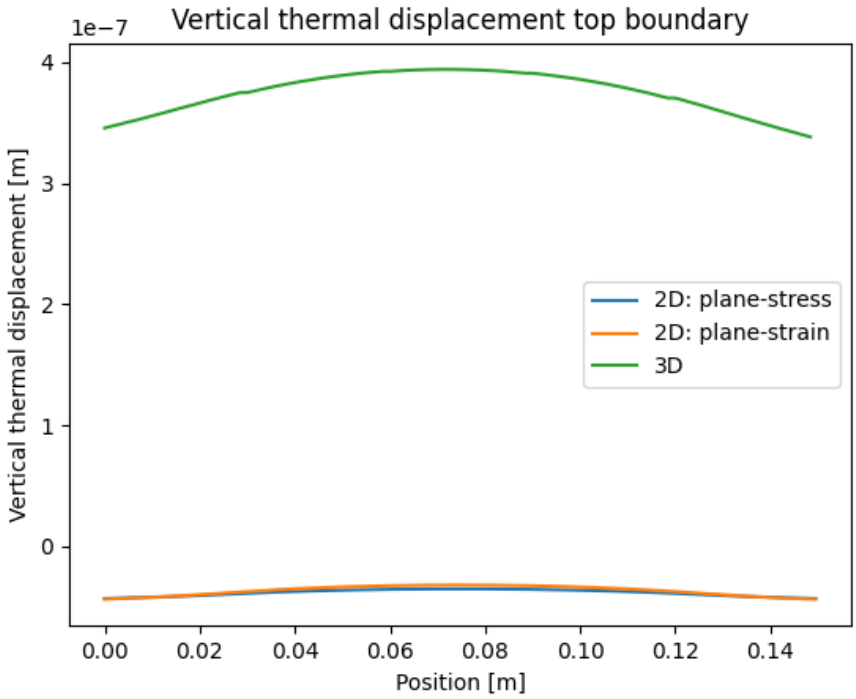

Figure A-2: Vertical thermal displacements for the top boundary of the unit cell array, obtained using 2D FEAs with plane-stress and plane-strain assumptions and a 3D FEA.

The vertical thermal displacements of the unit cell array for the top boundary is plotted in Figure A-2. Figure A-2 shows a discrepancy between the vertical thermal displacements for the top boundary obtained using the 2D models and the 3D model. However, it can also be seen that the vertical thermal displacements of the unit cell array for the top boundary is very similar for both plane-stress and plane-strain conditions. Since the results for plane-stress and plane-strain assumptions are very similar, it is chosen to use plane-stress assumptions since these are also used in Sigmund and Torquato [25].

Appendix B

Outline case parameters

Parameter definition

The following parameters are defined for the optimization formulation:

s_{x} :	Number of superelements in x-direction
s_{y} :	Number of superelements in y-direction
n_{x} :	Number of FE in x-direction for unit cell discretization
n_{y} :	Number of FE in y-direction for unit cell discretization
l_{x} :	Total width unit cell array in meters
l_{y} :	Total height unit cell array in meters
z_{nr} :	Number of uniform material layers per unit cell
z_{seq} :	Sequence of uniform material layers top to bottom
E_i :	Young's modulus for phase i in GPa
ν_i :	Poisson's ratio for phase i
α_i :	CTE for phase i in µm/(m°C)
$V_{\mathrm{max}}^{(i)}$:	Maximum volume fraction for phase i
c_{MSE} :	MSE constraint value vertical thermal top displacements
R :	Filter radius expressed in elements
β_{init} :	Initial continuation parameter
f_β :	Growth factor continuation parameter
β_{max} :	Maximum continuation parameter
η :	Threshold parameter intermediate topology
δ :	Threshold parameter dilated topology
it_{max} :	Maximum number of optimization iteration
x_{tol} :	Minimum change design variables

$ob_{\max}$: Maximum number of consecutive iterations meeting ob_{tol}
ob_{tol} : Minimum change objective in percent
$x_{\min}$: Minimum value density variables
O_{scale} : Scaling factor objective
x_0 : Initial density variables design vector

Parameter overview

Table B-1: Complete parameter overview for the performed validation cases.

	Case 1	Case 2	Case 3
s_{x}	2	2	2
s_{y}	5	5	5
n_{x}	150	150	150
n_{y}	60	60	60
l_{x}	0.15	0.15	0.15
l_{y}	0.15	0.15	0.15
z_{nr}	2	2	2
z_{seq}	$1+2$	$1+2$	$1+2$
E_1	69	69	69
ν_1	0.33	0.33	0.33
α_1	23.6	23.6	23.6
E_2	210	210	210
ν_2	0.33	0.33	0.33
α_2	12.0	12.0	12.0
$V_{\max}^{(1)}$	0.40	0.40	0.40
$V_{\max}^{(2)}$	0.25	0.25	0.25
c_{MSE}	2.43×10^{-10}	2.43×10^{-10}	2.43×10^{-10}
R	5.33	5.33	5.33
β_{init}	1	1	1
f_β	1.05	1.05	1.05
$\beta_{\max}$	20	20	20
η	0.5	0.5	0.5
δ	0.35	0.35	0.35
$it_{\max}$	250	250	250
x_{tol}	1×10^{-4}	1×10^{-4}	1×10^{-4}
$Ob_{\max}$	3	3	3
Ob_{tol}	0.01	0.01	0.01
$x_{\min}$	1×10^{-10}	1×10^{-10}	1×10^{-10}
O_{scale}	0.1	0.1	0.1
x_0	0.25	0.50	0.75

Appendix C

Convergence verification cases

Figures C-1, C-2 & C-3 presented in this appendix visualize the evolution of the objective function, the MSE constraints for the vertical thermal displacement of the top boundary of the unit cell array and the volume constraints for the aluminium and steel phases, for the verification cases presented in Section 3-2, initialized using uniform density variables 0.25, 0.50 and 0.75, respectively.

Case x_0=0.25

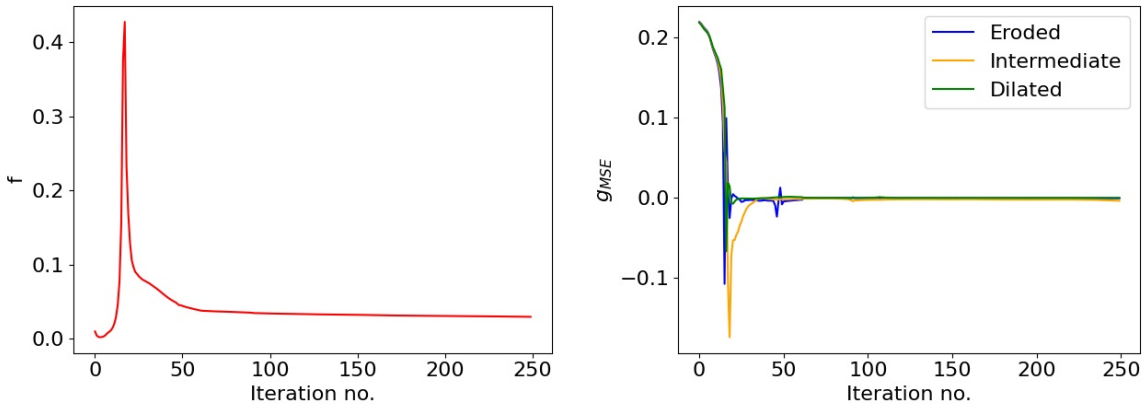

(a)

(b)

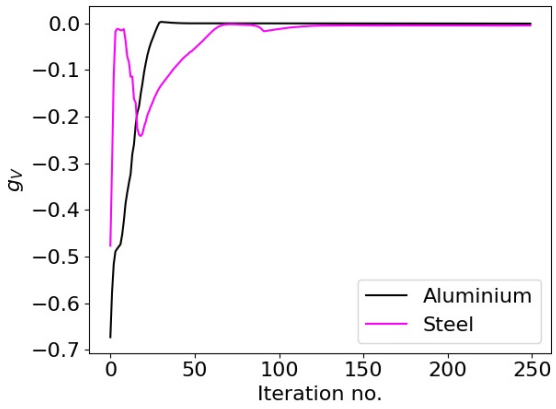

(c)

Figure C-1: Convergence plots for the verification case initialized using $x_0 = 0.25$. (a): Evolution of the objective function; (b): Evolution of the MSE constraint for the vertical thermal displacement of the top boundary of the unit cell array; (c): Evolution of the volume constraints for the aluminium and steel phase.

Case x_0=0.50

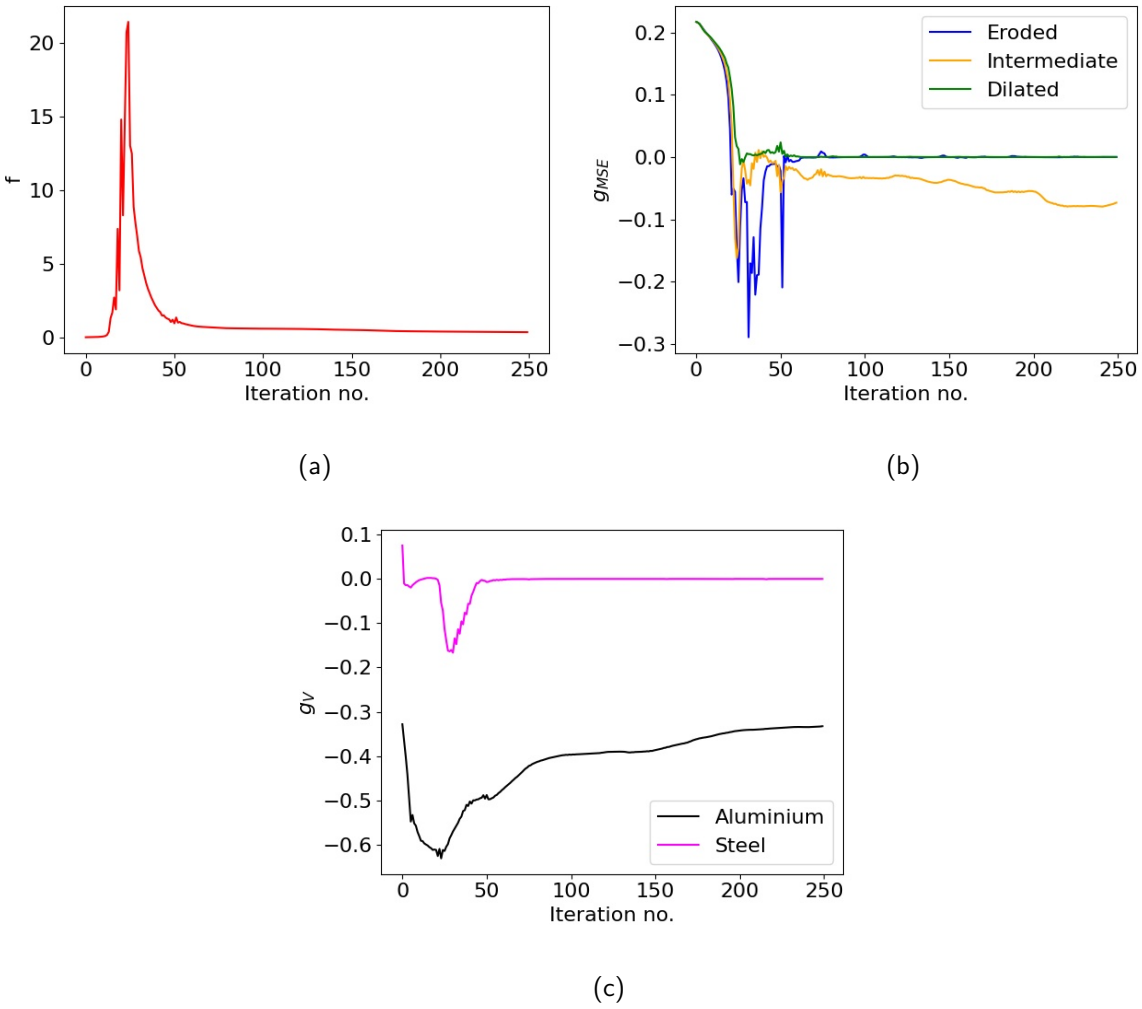

Figure C-2: Convergence plots for the verification case initialized using $x_0 = 0.50$. (a): Evolution of the objective function; (b): Evolution of the MSE constraint for the vertical thermal displacement of the top boundary of the unit cell array; (c): Evolution of the volume constraints for the aluminium and steel phase.

Case x_0=0.75

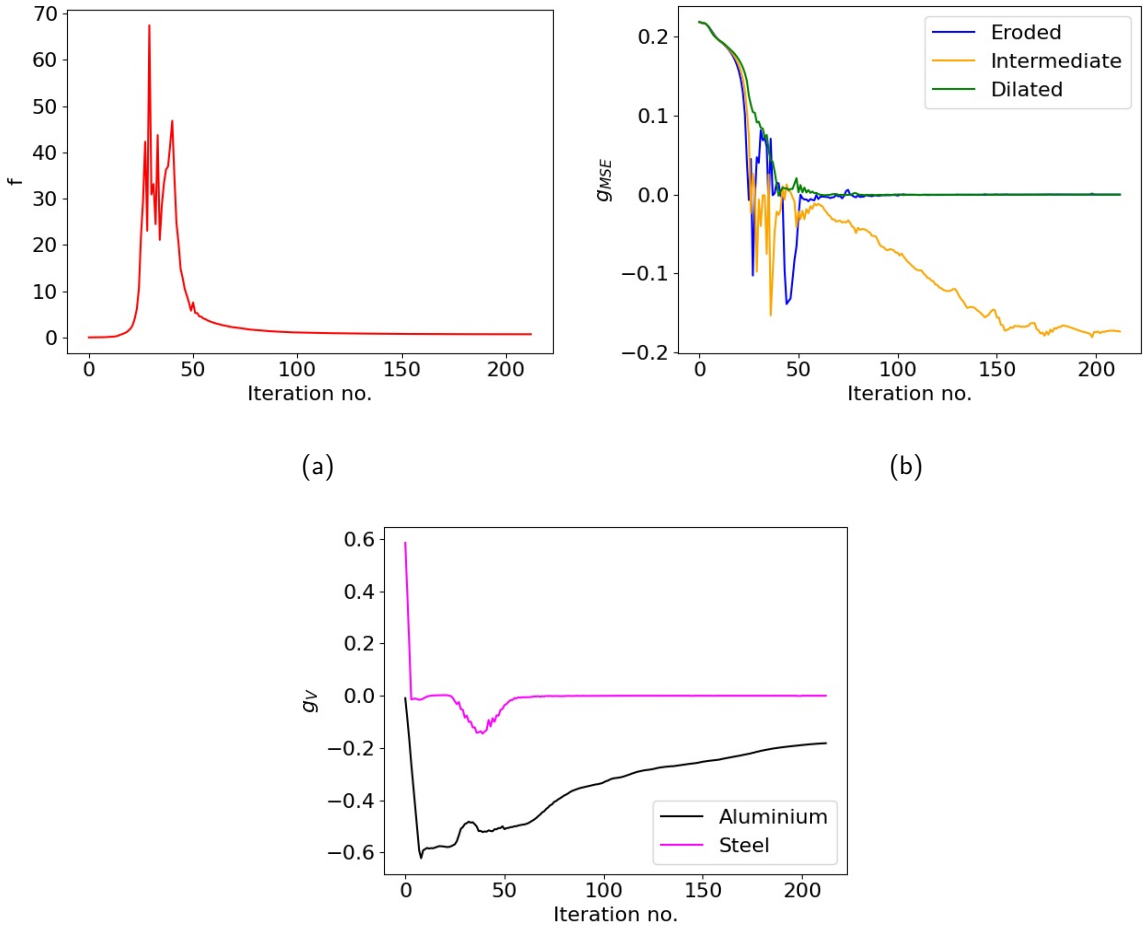

Figure C-3: Convergence plots for the verification case initialized using $x_0 = 0.75$. (a): Evolution of the objective function; (b): Evolution of the MSE constraint for the vertical thermal displacement of the top boundary of the unit cell array; (c): Evolution of the volume constraints for the aluminium and steel phase.

Appendix D

Details 3D Finite Element Analysis

Boundary conditions

The unconstrained design is visualized in Figure D-1. The BCs used in the 3D FEA are visualized in Figure D-2. As can be seen in Figure D-2, the two symmetry planes of the 3D design are utilized to decrease the computational cost. A roller support is used for the edge at the right-bottom corner of the design. The displacements transverse to the symmetry planes are furthermore constrained. Body forces are applied to the design for a temperature increase from 22 °C to 45 °C, which approximately is the temperature range examined during the experiment.

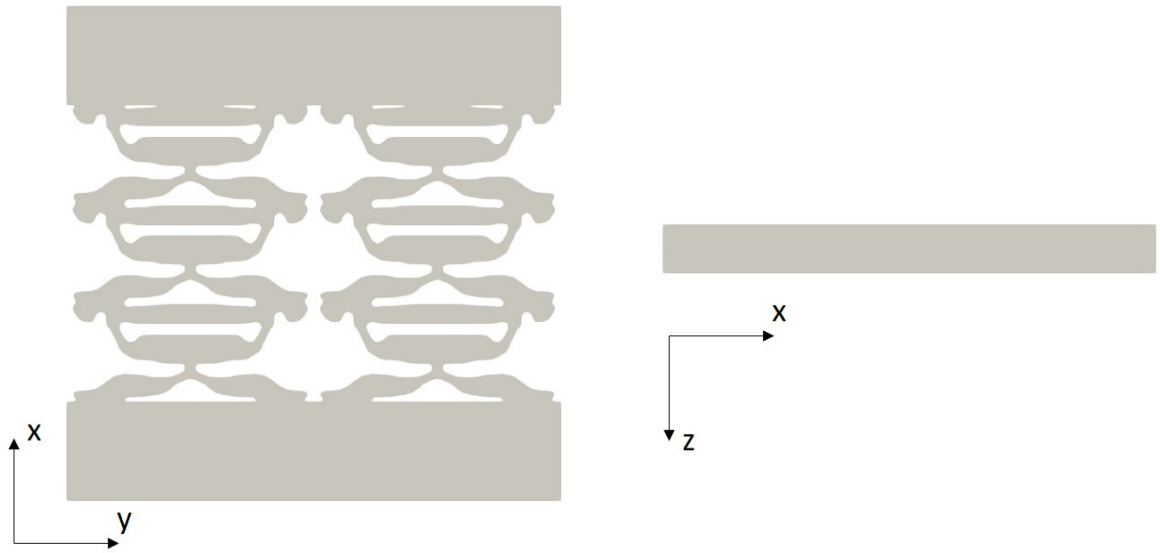

Figure D-1: Front (left) and top (right) views of the unconstrained topology which is experimentally verified. The allocation of the different material phases is not visualized in this figure.

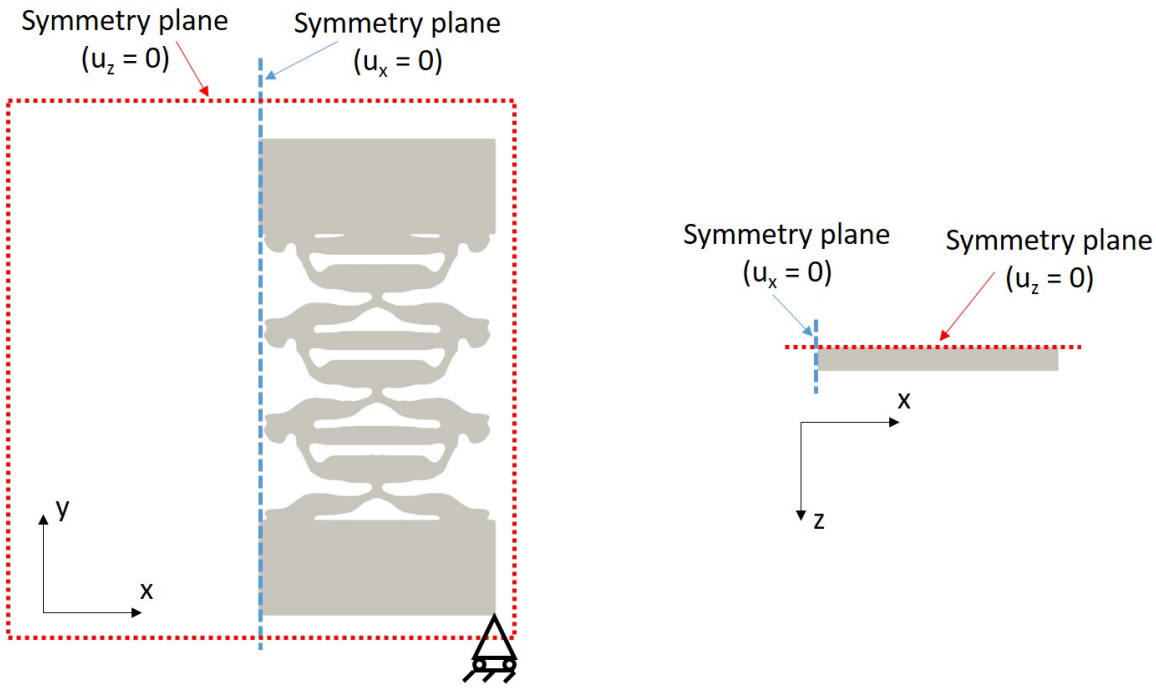

Figure D-2: BCs used in the 3D FEA of the topology which is experimentally verified. Both front (left) and top (right) view are provided. The allocation of the different material phases is not visualized in this figure.

Material properties

The material properties for the materials used in the 3D FEA are given in Table D-1. Linear elastic material models are assumed for all materials. Note that the material properties for the steel and aluminium material are assumed constant throughout the studied temperature range. The adhesive material (Araldite ® 2019) is modelled temperature dependent. A linear interpolation between the two displayed material points is used in the FE software. Temperature dependent shear modulus values for the adhesive were provided by the manufacturer, combined with the Young's modulus for a single temperature point. Therefore, an estimation of the temperature dependent Young's modulus is made by assuming a constant Poisson's ratio.

Table D-1: Material properties for the materials used in the 3D FEA of the optimized topology.

	T [°C]	E [GPa]	ν	G [GPa]	α [µm/m°C]
Steel	25 - 45	200	0.33	75.19	12.0
Aluminium	25 - 45	69	0.33	25.94	23.6
Adhesive	23	1.60	0	0.8	55
	60	0.98	0	0.49	55

Mesh

The mesh used in the 3D FEA is visualized in Figure D-3. Solid hexahedral elements are used throughout. In thickness direction, corresponding to the z-direction in Figure D-2, two elements are used in the model. Note that the adhesive layers are modelled by solid elements, with each adhesive layer being one element high. A mesh convergence study has not been performed due to license limitations on the system size, which did not allow to model the problem with smaller elements.

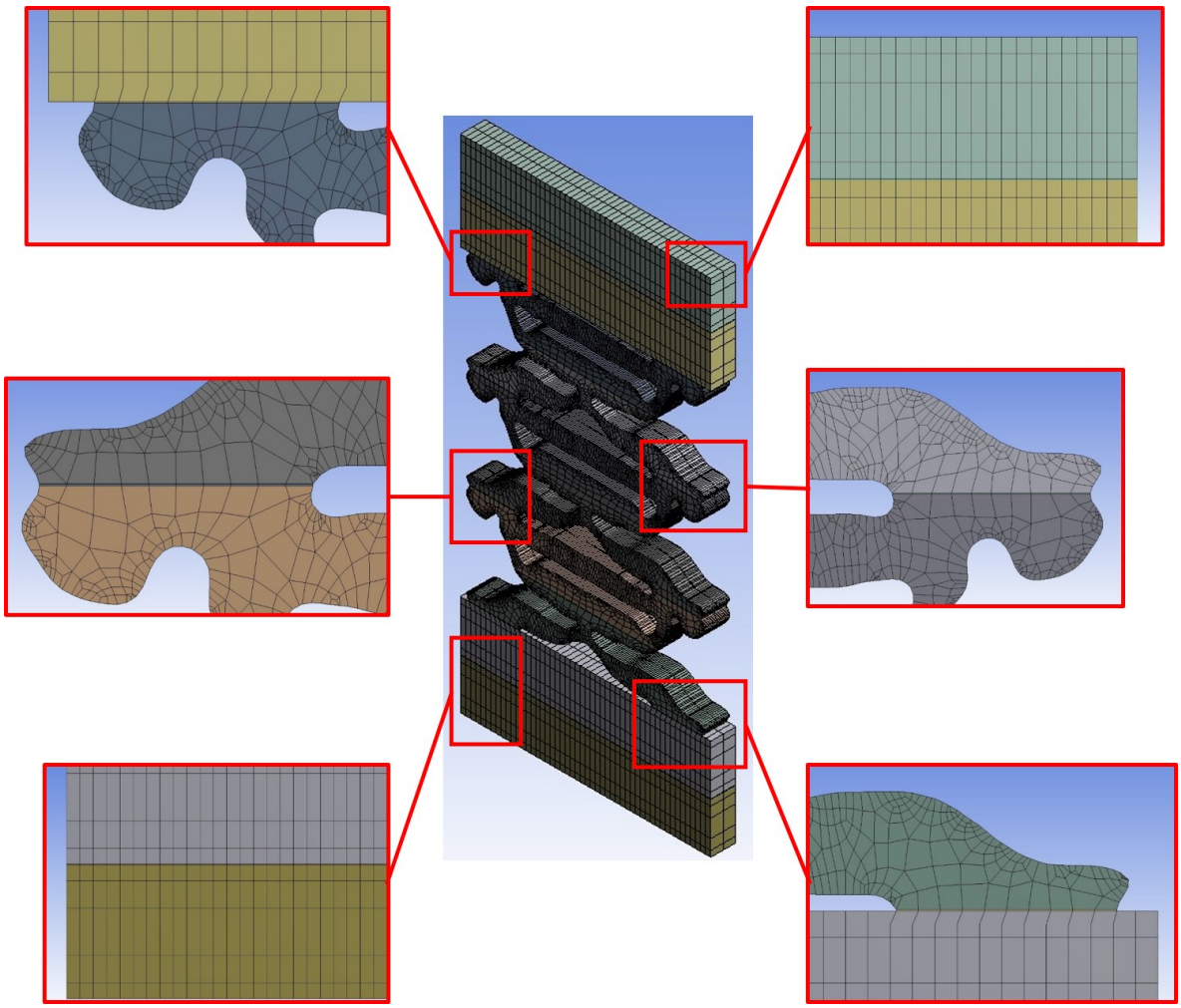

Figure D-3: Visualization of the FE mesh used in the 3D FEA of the optimized topology. Adhesive bonds are meshed using one layer of solid elements.

Stress and strain contours

The equivalent von-Mises stress and equivalent strain, obtained for the FEA, are presented in Figure D-4 and Figure D-5. The obtained maximum stress is 75 MPa, which is well below the yield stress for aluminium and steel. The stress in the adhesive layers is furthermore very small. The strain in the aluminium and steel sections is very low and is therefore not visualized. The maximum strain occurs in the adhesive layers and is equal to 0.26 %, which is well below the elongation at break specified by the manufacturer of 4.3 %.

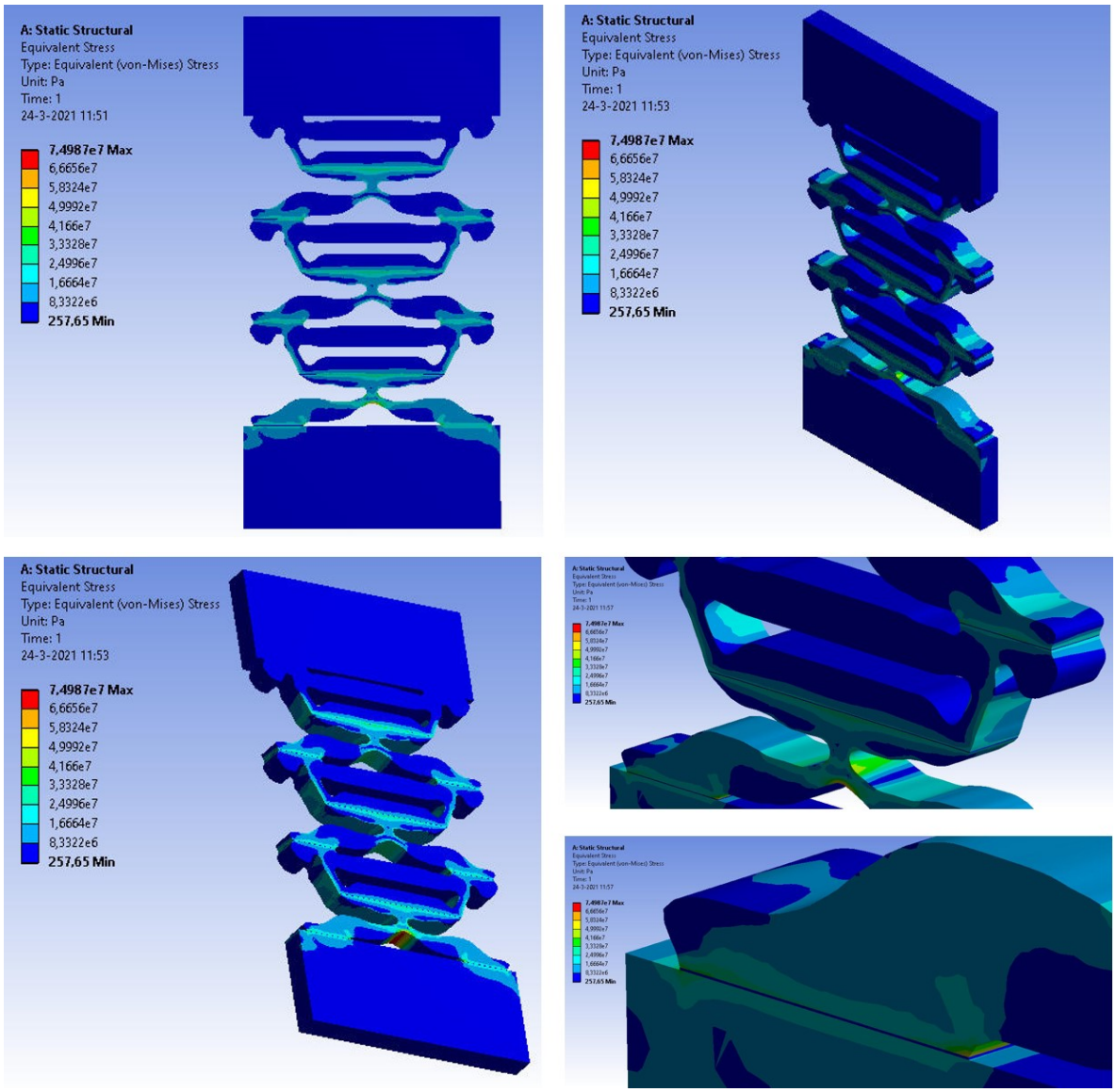

Figure D-4: Equivalent von-Mises stress contour of the optimized design for the thermal load case in Pa. Maximum stress occurs at the hinge area of the steel part of the lower unit cell and is equal to 75 MPa.

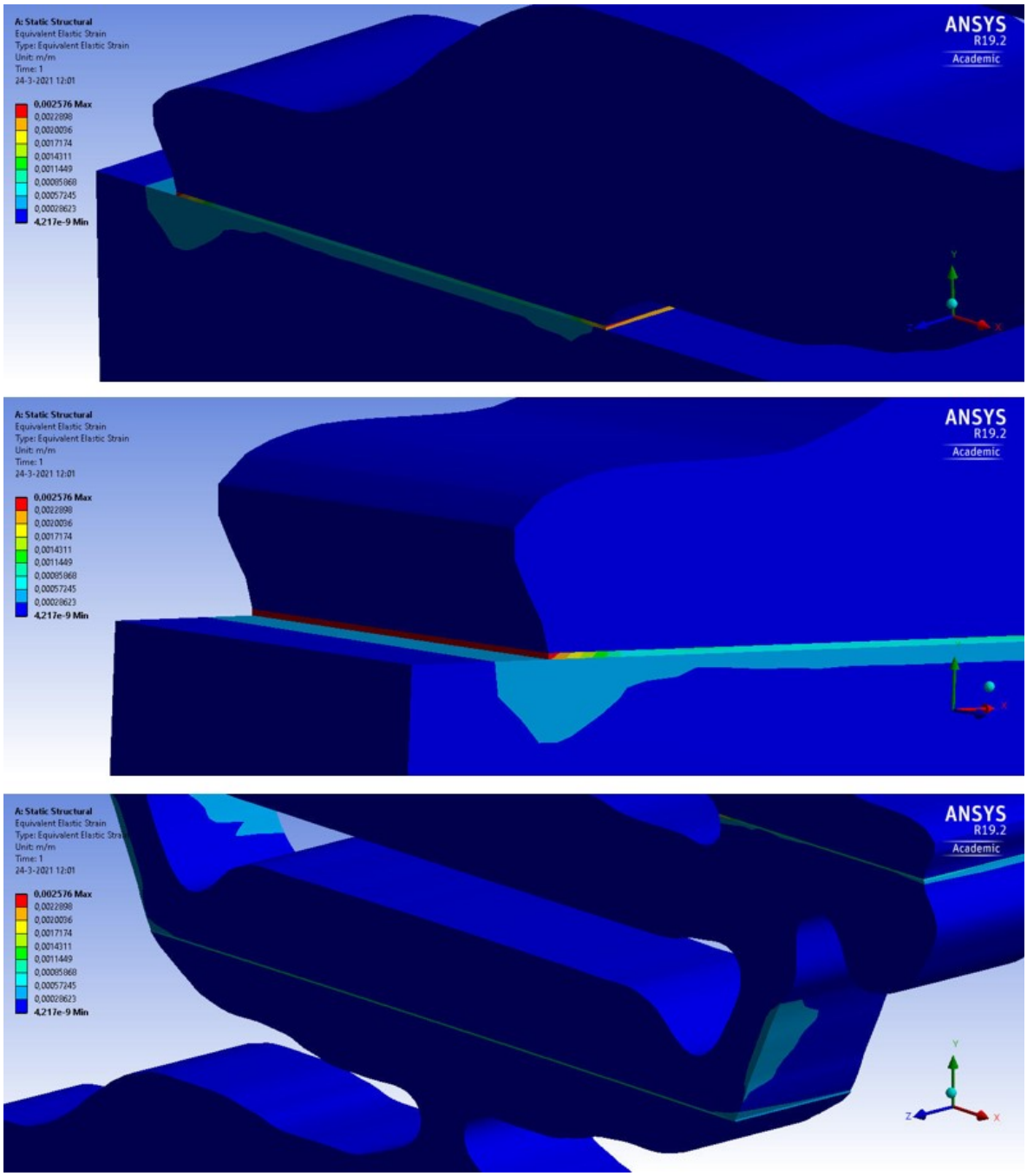

Figure D-5: Equivalent elastic strain contour of the optimized design for the thermal load case. Maximum strain occurs in the bottom adhesive layers and in equal to $0.26\,\%$.

Appendix E

Revision experimental setup

Initial setup

Laser sensor setup

Initially, the setup given in Figure E-1 was build for the experimental validation of the thermoelastic metamaterial structure, in which laser distance sensors were used. Unfortunately, one of the cables needed to connect the sensor heads to the sensor controller was not available. Therefore, no useful measurement were performed using the given setup and no further elaboration will be given.

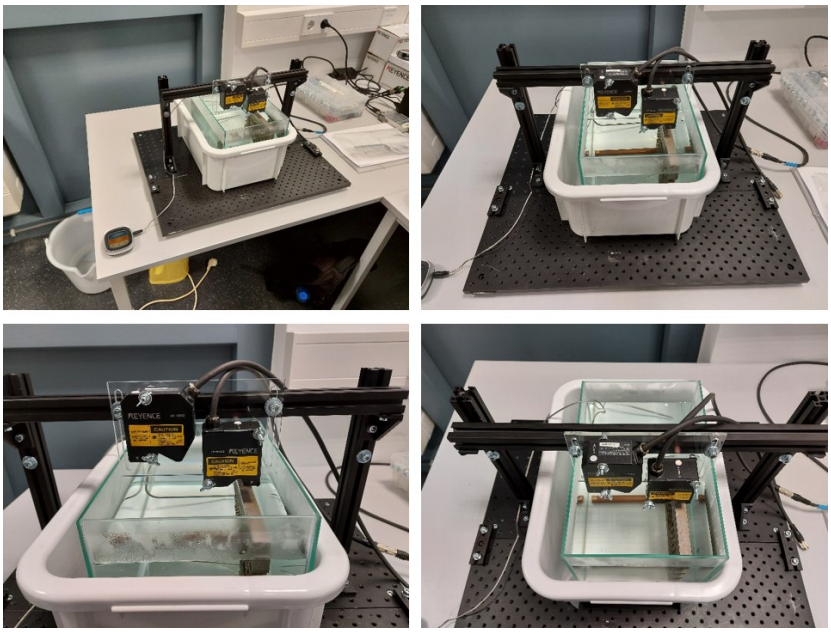

Figure E-1: Initial experimental setup for the experimental validation of the thermoelastic metamaterial structure, in which laser distance sensors are used.

Fiber optic sensor setup

Alternative sensors were sought-after to replace the incomplete laser sensor system. The resolution of the sensors has to be smaller than a few micrometers, since for $\Delta T = 10$ °C a thermal expansion smaller than 20 µm is expected for the steel sample and support, hence the difference between the thermal expansion of both samples is even smaller. Furthermore, ideally contactless sensors should be used, to prevent deformations caused by Hertzian contact stresses. Philtec D63-T fiber optic sensors were found, which met these conditions.

The setup given in Figure E-1 has been changed to accommodate the implementation of the fiber optic sensors. The setup using the fiber optic sensors in given in Figure E-2. The used fiber optic sensors need to be calibrated before each measurement. The optical peak of the sensors namely is dependent on the target's reflectively. The reflectively of the measurement surfaces vary from point to point due to small inconsistencies and imperfections. The optical peak should be identified and calibrated such that a value of exactly 5 V is obtained. Linear stages were introduced between the measurement frame and the sensors, to allow for easy detection of the optical peak.

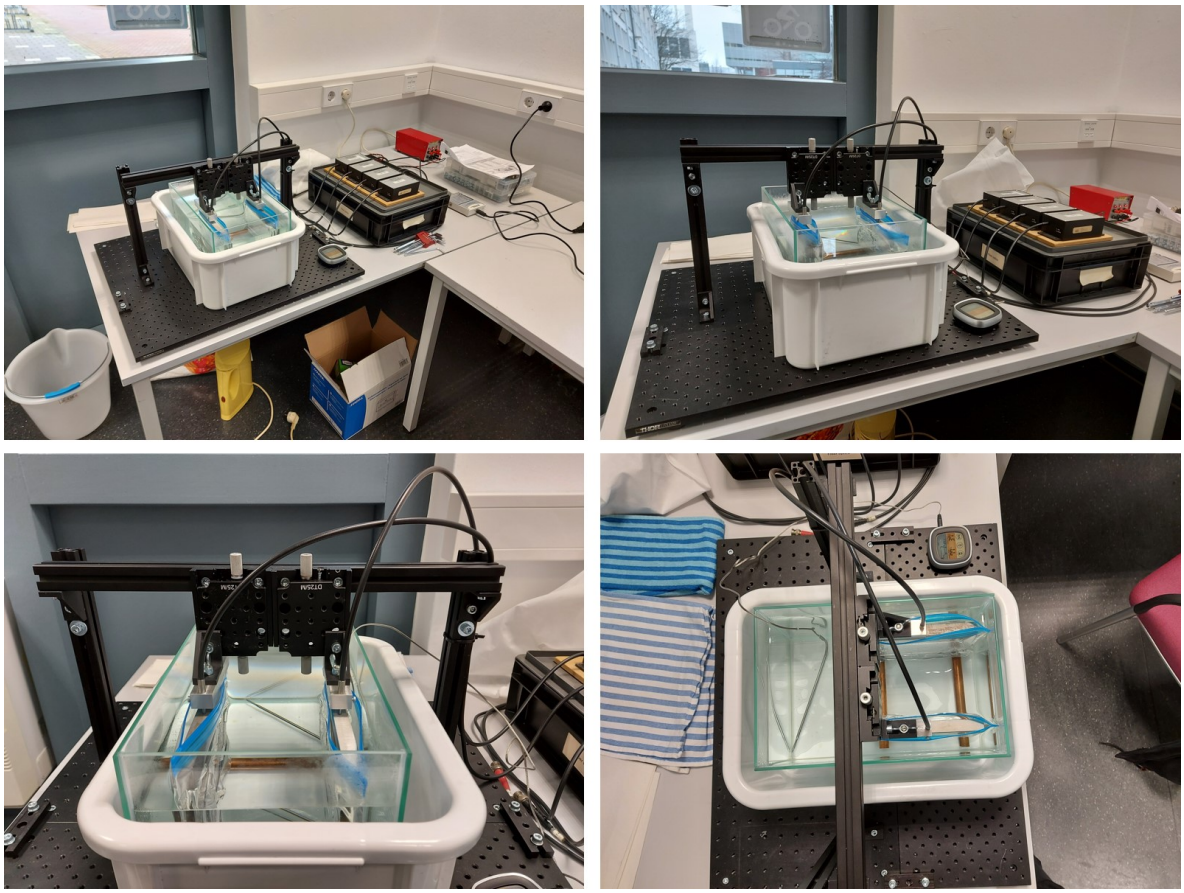

Figure E-2: Experimental setup used for the experimental validation of the thermoelastic metamaterial structure, in which fiber optics sensors were used.

Measurements

Results

Multiple measurements have been performed, in which the change of the gaps between the sensors and both samples are measured simultaneously. The results of these measurements are presented in Figure E-3. After each measurement it is verified that the calibration of the fiber optic sensors is still correct. Measurements in which the calibration verification failed are not presented. Furthermore, measurements in which the plastic bags surrounding the samples are broken are not presented as well.

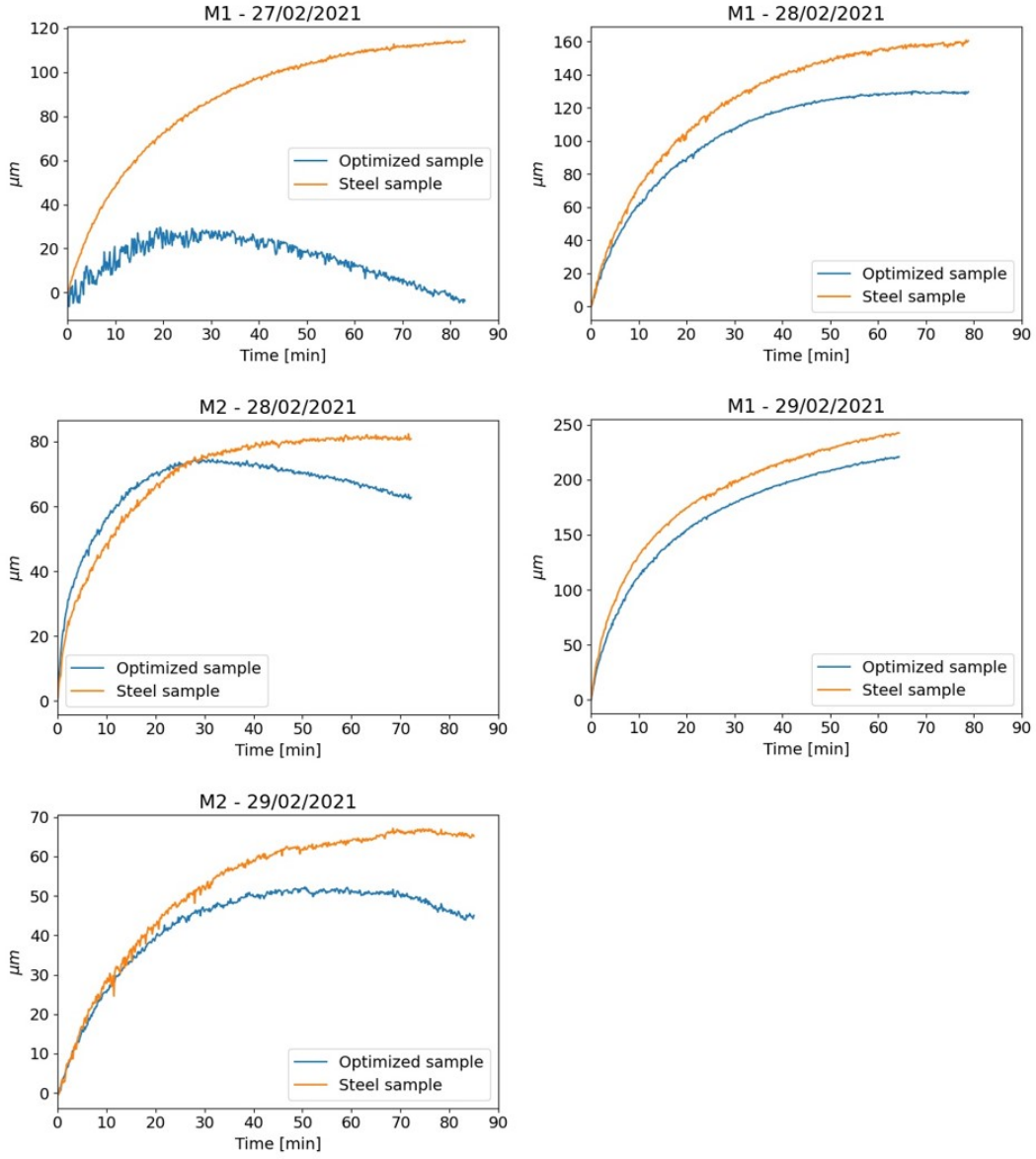

Figure E-3: Measured change in the sensor gaps using the setup given in Figure E-2. Measurements are initialized at $46\,^{\circ}\mathrm{C}$ and are ended at $35\,^{\circ}\mathrm{C}$.

Discussion

A few remarkable observation were made from the obtained measurement results presented in Figure E-3. First of all, the magnitudes of the change in the gaps measured during the performed experiment are significantly larger than the expected change. Furthermore, it can be seen that inconsistent results are obtained for the different measurements. Both the magnitude, trend and ratio between the change in the gaps differ in each measurement. In this section, it will be explained why the obtained results are remarkable.

The notice that we obtain unusually high magnitudes for the change is the measured gaps, is based on studying the change in the gap for the steel sample, for which the approximate CTE is known. The linear thermal expansion of the steel sample can be approximated by the following formula:

$$\delta L = \alpha L_0 \Delta T. \tag{E-1}$$

Approximating the linear thermal expansion of the steel sample and the copper support pipes, gives a thermal expansion for ΔT = 11 °C of approximately 22 µm. From the measurement results it can be seen that the change in the gap between the sensor and the steel sample is a factor 3 till 10 times higher. Hence either unreliable measurements from our sensors are obtained or the change in the gap is actually this large, caused by for example deformations or instabilities of the measurement setup.

Besides the unexpectedly large magnitudes for the change of the gaps, it can furthermore be seen that very different results are obtain for the different measurements. Most measurements show very different magnitudes and trends for the change in the gaps during the experiment. Furthermore, the ratio between the change of the gaps for the steel and the optimized samples diverges largely for each measurement. A couple of factors can be pinpointed that are known to cause slight differences between the different measurements:

- The initial water temperature of the hot water poured into the container housing the samples is not exactly the same for each measurement, but varies from approximately 50 °C to 55 °C.
- The temperature at which the measurement is started and ended are approximately, but not exactly, the same for each measurement.
- The cooling rate of the water and samples is not controlled in the experiment. The water is left to cool down and different external factors for each measurement could influence the cooling rate of the water.
- The temperature history of the samples and measurement setup is not exactly controlled. The initial temperatures of the samples and measurement setup before they are exposed to the hot water might differ for each measurement, due to prior measurements or different external influences.
- The exact position of the samples and supports relative to the measurement frame is not accurately controlled. Therefore, the measurement points on the samples might slightly differ for each measurement.

Although the bullet points listed above are known to cause differences between the individual measurements, they are not expected to be the cause of the large differences and inconsistencies observed in the measurement results. The inconsistencies are expected to be caused either by unreliable sensor measurements or by instabilities in the measurement setup.

Troubleshooting

In order to pinpoint the main cause or causes of the inconsistencies seen in the measurement results, different possibilities are ruled out systematically. First, it is verified that we obtain reliable sensor measurements, by mounting the sensors directly to the breadboard and studying the measurement data. Then, a measurement is performed on two identical steel samples using the setup from Figure E-2. No heat in introduced to both the samples and the measurement setup. Furthermore, the linear stages mounted between the measurement frame and the sensors are eliminated from the measurement setup. Finally, the same measurement is repeated but now with the steel samples subjected to the hot water, similar as in the measurements presented in Figure E-3. The results and discussion for these measurements are presented in this section.

The measurement setup and results used to verify reliable sensor data are presented in Figure E-4. It can be seen that the sensors produce reliable data. Over a time period of approximately 40 minutes the maximum variation in the measured sensor gap is approximately 2.5 µm. The inconsistencies seen in the measurement results presented in Figure E-3 are therefore not caused by unreliable sensor data.

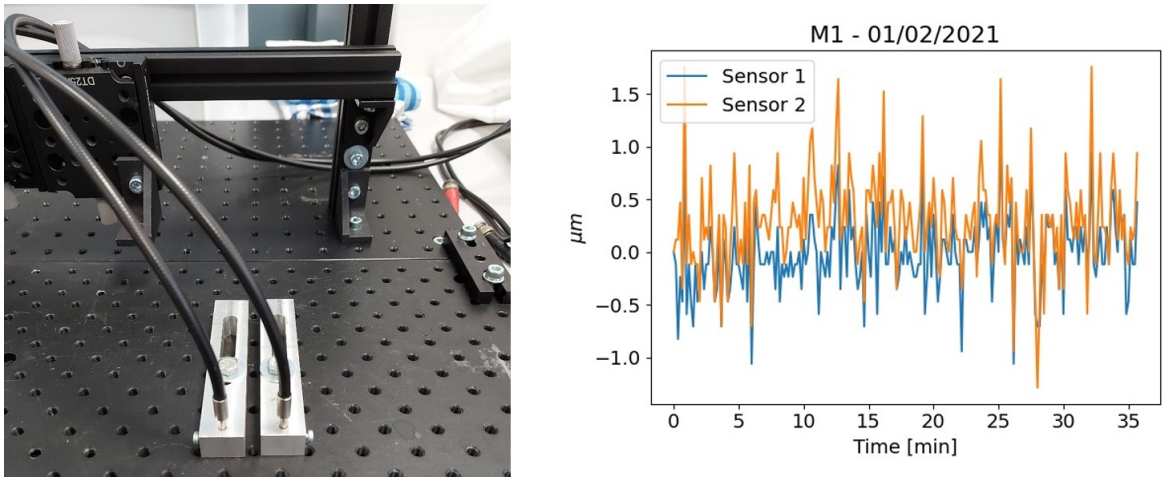

Figure E-4: Setup and measurement data for the measurement used to verify reliable sensor measurements.

In order to identify instabilities in the measurement setup presented in Figure E-2, a measurement is performed with a modified setup presented in Figure E-5. The measurement is performed without subjecting the steel samples to hot water, to exclude the possible influence of thermal instabilities in the setup. Furthermore, the linear stages are deleted between the measurement frame and the sensors. Since the linear stages are deleted, a new calibration method has been introduced. The sensors are calibrated on an external calibration stage, for a white paper target. The same paper is attached to the samples, to ensure that the reflectively of the measured target is the same as the reflectively of the target used during calibration.

From the measurement data presented in Figure E-5, it can be seen that the measurement is not entirely stable, but a maximum change in the gaps of approximately 4 µm is obtained.

Nevertheless, the measurement is considerably more stable than the measurements presented in Figure E-3. Hence, either the linear stages or thermal influences cause the instabilities seen in the measurements presented in Figure E-3. The instabilities can also still be caused by both the linear stages and the thermal influences.

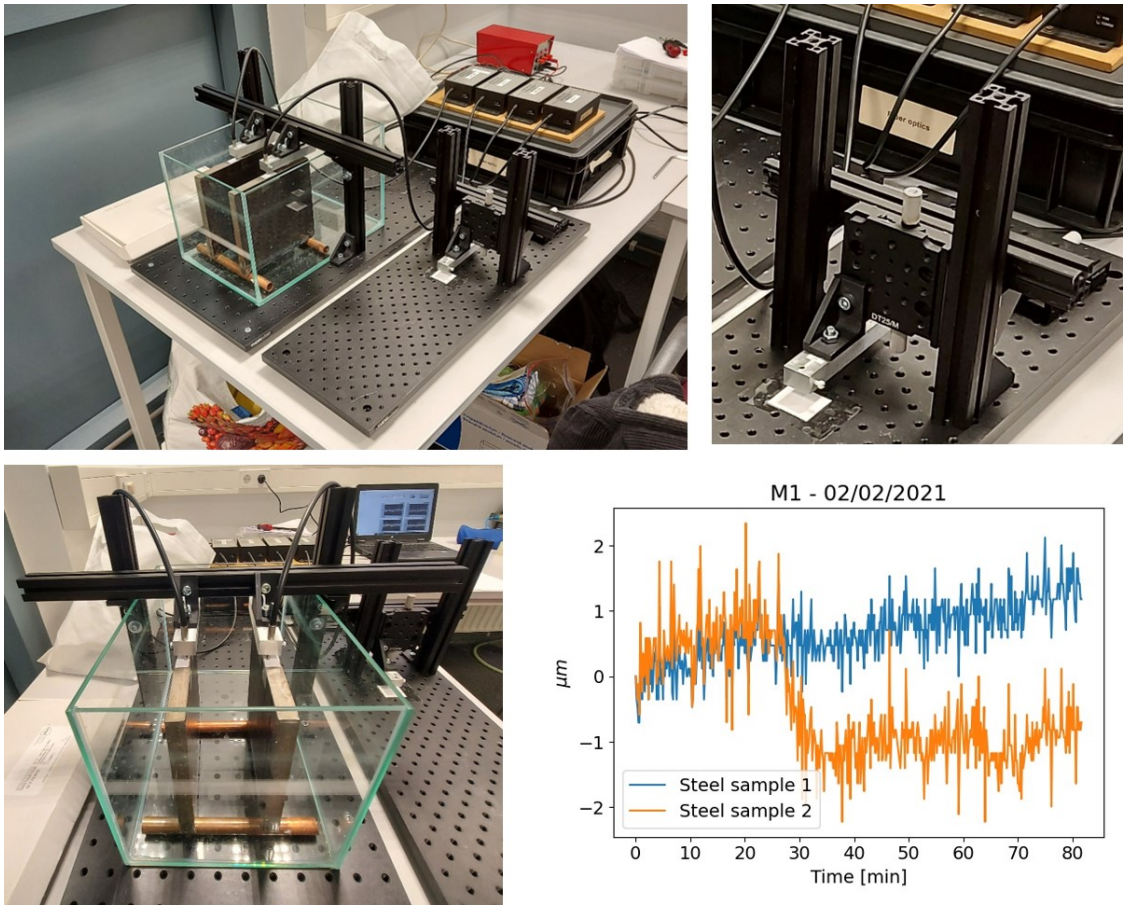

Figure E-5: Setup and measurement data for the measurement used to detect setup instabilities.

In order to determine if the instabilities are caused by the linear stage, the thermal influences ,or both, the same measurement is repeated but now with the samples subjected to the hot water. The same measurement setup as presented in Figure E-5 is used for the measurement. The measurement data is given in Figure E-6.

From the measurement data presented in Figure E-6, it can be seen that the change in the gap between the sensor and steel sample 2 is larger than the change in the gap between the sensor and steel reference sample 1. Studying the change in the gaps starting from the measurement taken after 20 minutes, it can however be seen that the change in the gaps is almost identical for both steel samples. The magnitudes of the change in the gaps are reasonably close to the expected linear thermal expansion for the given temperature change. From the performed troubleshooting measurements it is concluded that the linear stages between the measurement frame and the sensors were the main cause of the observed instabilities. The thermal stability of the measurement frame should ideally however also be improved, to prevent the initial instable thermal response as seen in Figure E-6.

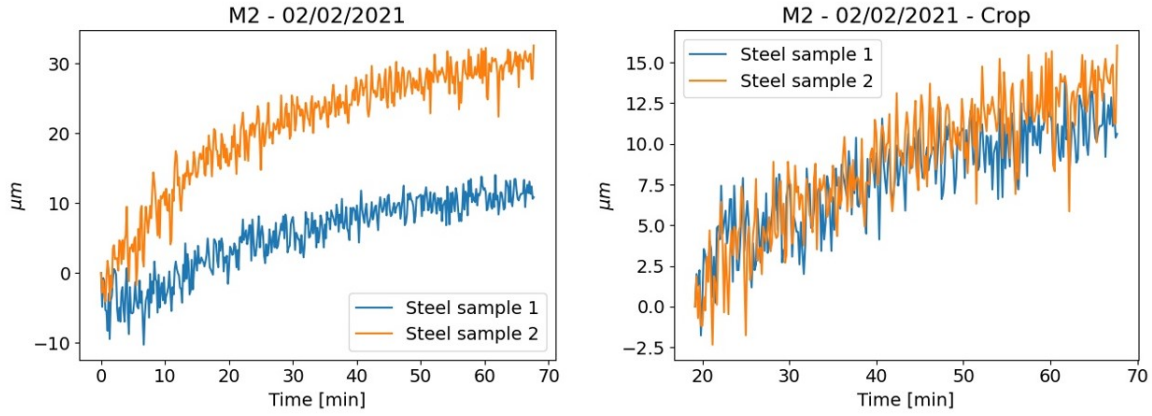

Figure E-6: Measurement data for the measurement used to detect thermal setup instabilities of the setup given in Figure E-5. Measurements initialized at $40\,^{\circ}\mathrm{C}$ and ended at $30\,^{\circ}\mathrm{C}$. Left: Full measurement; Right: Change sensor gaps with reference point at 20 minutes.

Conclusion

In conclusion, the performed measurements presented in Figure E-3 are believed to be dominated by instabilities in the measurement setup. Since the measurements are non-repeatable, no conclusions can be drawn from the measurements.

Based on the performed troubleshooting measurements, the instabilities are believed to be mainly caused by the tolerances and play in the used linear stages. Furthermore, the thermal stability of the measurement frame should ideally be improved, to obtain measurements stable enough to determine the unidirectional thermal expansion of the optimized sample quantitatively.

A new measurement setup, presented in Section 5-3-1, is designed to eliminate these problems. The linear stages are removed and the sensors are directly mounted to a stiff measurement frame. The measurement frame is furthermore made entirely of aluminium, which has a high thermal conductivity to help establishing a uniform thermal deformation and to prevent warping. The measurement frame is placed within the container housing the hot water, to eliminate instabilities from the container itself and to ensure uniform heating. Finally, the measurement location of the sensors in the new setup is closer to the supports for the samples, in order to reduce a possible Abbe error [94] caused by an angular positioning error.

Verification

In order to verify that the new setup is stable, multiple verification measurements have been performed. First of all, measurements have been performed on two identical steel samples, in which the controlled variables are not changed. Subsequently, verification measurements have been performed in which the identical steel samples are subjected to heat. The controlled variable for the experiment is the environmental temperature for the samples. In the first verification measurement, the environmental temperature is not actively changed. No hot

water is thus poured in the container housing the samples. The change of the gaps between the sensors and the samples is measured. Assuming that uncontrolled parameters and the environmental temperature are not changing, the gaps between the sensors and the samples should remain the same. Any changes in uncontrolled parameters, assuming that these do not vary locally, should influence both sensor gaps equally. The measurement setup for the verification measurement is presented in Figure E-7.

Figure E-7: Experimental setup used to verify the stability of the final measurement setup.

The measurement results are given in Figure E-8. It can be seen that for all measurements except one, the difference between the change in the sensor gaps for both samples is smaller than 5 µm. Only for measurement 'M1 - 15/02/2021', it can be seen that the change in the sensor gap for the steel samples varies largely and that especially the sensor gap for steel sample 2 changes considerably compared to the other measurements. No cause is verified for the large change in the sensor gap for steel sample 2, although it is expected that the sensor might not have been clamped sufficiently. Nevertheless, it can be seen that the majority of the measurements is stable and show only small differences for the change in the sensor gaps for both samples. The improved setup is therefore confirmed to be sufficiently stable for nearly constant temperatures, although the uncertainty resulting from the slight setup instabilities should be addressed when quantitatively determining the unidirectional thermal expansion of the optimized sample.

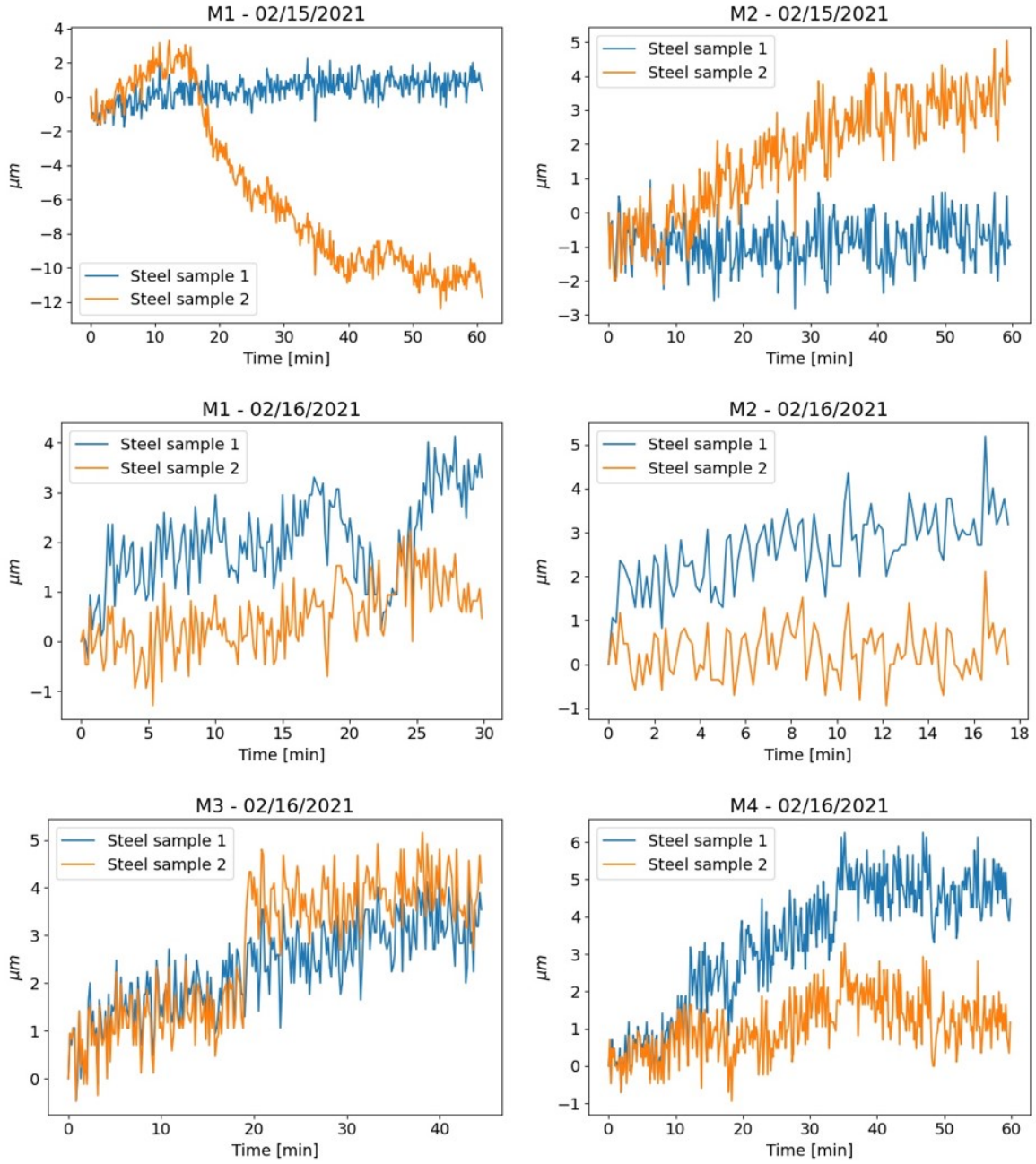

Figure E-8: Measurement data for the measurements used to detect setup instabilities in the final measurement setup. Controlled parameters are not actively changed.

In order to verify that the measurement setup is also thermally stable, additional verification measurements are performed. The same measurement setup is used, but the environmental temperature for the steel samples is now controlled by subjecting the samples and measurement setup to hot water, as can be seen in Figure E-9.

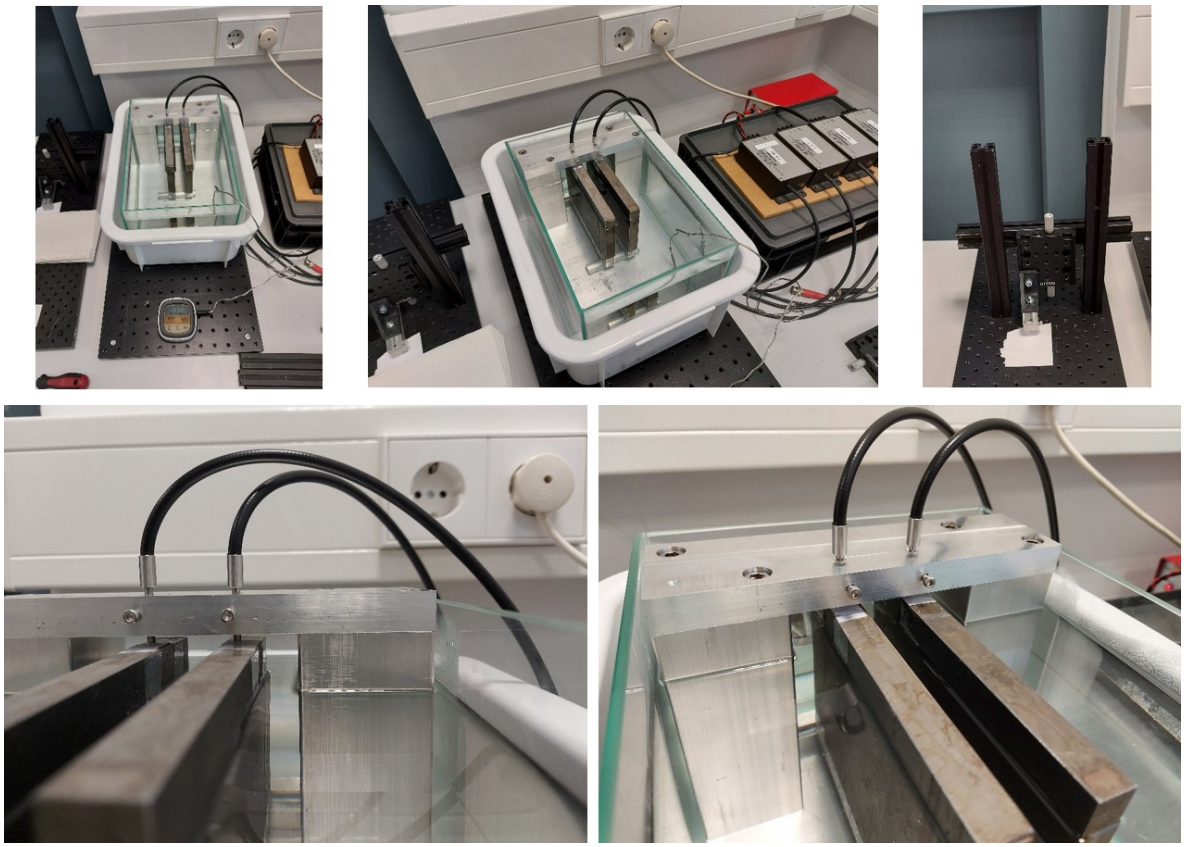

Figure E-9: Experimental setup used to verify the thermal stability of the final measurement setup.

The water is left to cool down slowly and the change in both sensor gaps is measured. Since both samples are identical, the change in both sensors gaps should ideally be the same. The results for the verification measurements are presented in Figure E-10.

The results of the verification measurements show that the change is the sensor gaps for both samples is almost identical. Furthermore, the absolute value of the measured change in the sensor gaps corresponds roughly to the change expected from the linear thermal expansion of the measurement setup and the samples. From the following expression:

$$\delta_{\text{gap}} = L_0(\alpha_{\text{alu}} - \alpha_{\text{steel}})(T_1 - T_0), \tag{E-2}$$

the expected change in the sensor gaps is calculated to be $-15.08\,\mu\text{m}$ for $L_0 = 0.13\,\text{m}$, $\alpha_{\text{alu}} = 23.6\,\mu\text{m}/(\text{m}^\circ\text{C})$, $\alpha_{\text{steel}} = 12.0\,\mu\text{m}/(\text{m}^\circ\text{C})$, $T_0 = 40\,^\circ\text{C}$ and $T_1 = 30\,^\circ\text{C}$. The measured change in the sensor gaps for 'M1 - 17/02/2021' are $-13.68\,\mu\text{m}$ and $-13.35\,\mu\text{m}$. For 'M2 - 17/02/2021' the measured change in the sensor gaps is $-13.33\,\mu\text{m}$ and $-14.99\,\mu\text{m}$. Hence the maximum deviation of the measured change in the sensor gaps compared to the expected change is the sensor gaps is smaller than $12\,\%$.

It can however be seen that large and abrupt peaks appear in measurement 'M1 - 17/02/2021'. The faces of the steel samples are cut using a waterjet cutting machine. These faces are therefore not nicely smooth, causing especially steel sample 2 to be a bit wobbly, explaining the large abrupt peaks in the first measurement. For measurement 'M2 - 17/02/2021', special attention is paid to the stable positioning of both steel samples.

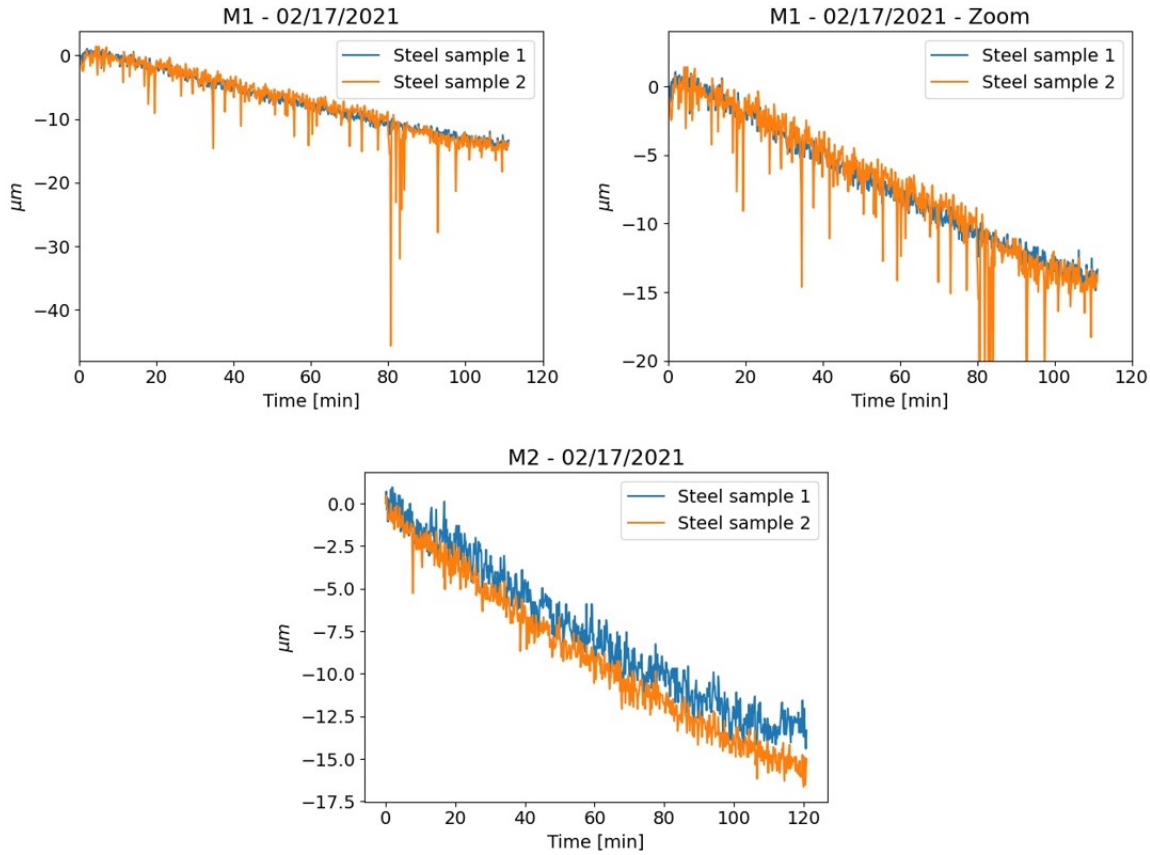

Figure E-10: Measurement data for the measurements used to detect thermal setup instabilities in the final measurement setup. Measurements initialized at 40 °C and ended at 30 °C.

In conclusion, it is verified that the measurement setup is sufficiently stable to quantitatively determine the unidirectional thermal expansion of the optimized sample. Influences of uncontrolled variables cause only small differences between the change in the sensor gaps. The resulting uncertainty should however be addressed for the quantitative determination of the unidirectional thermal expansion of the optimized sample. The thermal stability of the experimental setup is furthermore found to be sufficient. For a controlled environmental temperature change, the change in the sensor gaps for two identical steel samples was found to be almost identical and the observed maximum deviation from the expected value was smaller than 12 %. Special attention should however be paid to the clamping force with which the sensors are held in place. Furthermore, it should be verified before starting a measurement that both samples are positioned sufficiently stable on the measurement setup.

Appendix F

Experimental thermal expansion

Derivation expression α_{opt}

In order to determine the experimentally obtained unidirectional thermal expansion of the optimized sample, an expression should be derived which relates the measured change in the sensor gaps to a measure for its unidirectional thermal expansion. For the derivation, the definitions presented in Figure F-1 are used.

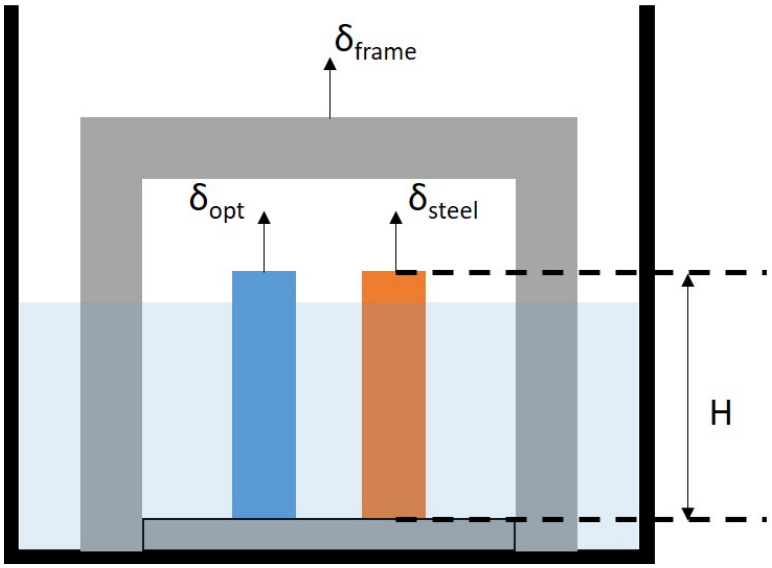

Figure F-1: Definitions used for the derivation of the measured unidirectional thermal expansion, visualized on a simplified schematic overview of the experimental setup.

The measured change in the sensor gaps can be expressed as follows, in terms of the definitions presented in Figure F-1:

$$\Delta_{\text{gap,opt}} = \delta_{\text{frame}} - \delta_{\text{opt}}, \tag{F-1}$$

$$\Delta_{\text{gap,steel}} = \delta_{\text{frame}} - \delta_{\text{steel}}, \tag{F-2}$$

in which $\Delta_{\text{gap,opt}}$ and $\Delta_{\text{gap,steel}}$ are the measured change in the sensor gaps for the optimized and steel sample, respectively, in which positive values indicate increasing sensor gaps. The difference between the measured change in both sensor gaps can therefore be expressed as follows, assuming that the entire samples are subjected to the temperature change introduced for the experiment:

$$\begin{aligned} G = \Delta_{\text{gap,opt}} - \Delta_{\text{gap,steel}} &= \delta_{\text{frame}} - \delta_{\text{opt}} - (\delta_{\text{frame}} - \delta_{\text{steel}}), \\ &= \delta_{\text{steel}} - \delta_{\text{opt}}, \end{aligned} \tag{F-3}$$

which can be rewritten as:

$$\delta_{\text{opt}} = \delta_{\text{steel}} - G. \tag{F-4}$$

The unidirectional thermal expansion of the optimized sample can now be expressed as follows in terms of the thermal expansion of the steel sample:

$$\alpha_{\text{opt}} = \frac{\delta_{\text{opt}}}{H\Delta T} = \alpha_{\text{steel}} - \frac{G}{H\Delta T}. \tag{F-5}$$

Both samples are however not fully submerged in the hot water, as visualized in Figure F-1. The temperature change for a part of the sections of the samples that protrudes above the water, might therefore be lower than for the remainder of the samples. The expression for the unidirectional thermal expansion of the optimized sample should therefore be compensated, for the parts of the samples that are not subjected to the temperature change during the experiment. The protruding sections are of solid aluminium and steel, for the optimized and steel sample, respectively. Introducing a compensation term for the expansion that would have occurred if the entire samples were heated, therefore gives the following compensated expression for Eq. (F-1) and Eq. (F-2):

$$\Delta_{\text{gap,opt}} = \delta_{\text{frame}} - (\delta_{\text{opt}} - \alpha_{\text{alu}} d_{\text{error}} \Delta T), \tag{F-6}$$

$$\Delta_{\text{gap,steel}} = \delta_{\text{frame}} - (\delta_{\text{steel}} - \alpha_{\text{steel}} d_{\text{error}} \Delta T), \tag{F-7}$$

$$\tag{F-8}$$

in which $\Delta_{\text{gap,opt}}$ and $\Delta_{\text{gap,steel}}$ are still the measured change in the sensor gaps for the optimized and steel sample, respectively. The distance d_{error} is the part of the samples, that is not subjected to a temperature change during the experiment. Accounting for the compensation terms, the measured change in both sensor gaps is now given by:

$$G = \Delta_{\text{gap,opt}} - \Delta_{\text{gap,steel}} = \delta_{\text{steel}} - \delta_{\text{opt}} + (\alpha_{\text{alu}} - \alpha_{\text{steel}}) d_{\text{error}} \Delta T, \tag{F-9}$$

which can be rewritten as:

$$\delta_{\text{opt}} = \delta_{\text{steel}} - G + (\alpha_{\text{alu}} - \alpha_{\text{steel}}) d_{\text{error}} \Delta T. \tag{F-10}$$

The unidirectional thermal expansion of the optimized sample, compensated for the parts of the samples that are not subjected to the temperature change during the experiment, is now expressed as:

$$\alpha_{\text{opt}} = \alpha_{\text{steel}} - \frac{G}{H\Delta T} + \frac{(\alpha_{\text{alu}} - \alpha_{\text{steel}})d_{\text{error}}}{H} \tag{F-11}$$

Derivation expression uncertainty α_{opt}

The uncertainty of the unidirectional thermal expansion of the optimized sample, is dependent on the uncertainty of the parameters used to determine the unidirectional thermal expansion. The general formula for error propagation can be used to compute the uncertainty of the unidirectional thermal expansion of the optimized sample, in terms of the uncertainty of the parameters used to determine its value [95]. Applying the general formula for error propagation on the expression of the unidirectional thermal expansion of the optimized sample given in Eq. (F-11), results in:

$$\begin{aligned}
\delta\alpha_{\text{opt}} =& \left\{ \left(\frac{\partial \alpha_{\text{opt}}}{\partial G}\delta G \right)^2 + \left(\frac{\partial \alpha_{\text{opt}}}{\partial H}\delta H \right)^2 + \left(\frac{\partial \alpha_{\text{opt}}}{\partial \Delta T}\delta \Delta T \right)^2 + \left(\frac{\partial \alpha_{\text{opt}}}{\partial d_{\text{error}}}\delta d_{\text{error}} \right)^2 \right\}^{1/2} \\
=& \left\{ \left(\frac{-1}{H\Delta T}\delta G \right)^2 + \left(\left(\frac{G}{H^2\Delta T} - \frac{(\alpha_{\text{alu}} - \alpha_{\text{steel}})d_{\text{error}}}{H^2} \right) \delta H \right)^2 + \right. \\
& \left. \left(\frac{G}{H\Delta T^2}\delta \Delta T \right)^2 + \left(\frac{\alpha_{\text{alu}} - \alpha_{\text{steel}}}{H}\delta d_{\text{error}} \right) \right\}^{1/2}
\end{aligned} \tag{F-12}$$

Values

In this section, we will discuss the values and corresponding uncertainties for the parameters used to determine the unidirectional thermal expansion of the optimized sample. An overview of the parameter values and uncertainties is given in Table 5-2.

Temperature change ΔT

The temperature of the hot water is cooled down from 40 °C to 30 °C during the experiment. A temperature change ΔT of -10 °C is therefore observed and an uncertainty of 1 °C is enforced. The uncertainty is dominated by the uncertainty of the thermometer, which has a limited accuracy and furthermore is subjected to a rounding error, since only whole numbers are displayed. Furthermore, the uncertainty of the temperature change includes the uncertainty resulting from a possible difference between the water temperature and the temperature of the samples, although this uncertainty is assumed low due to the very slow cooling rate observed.

Sample height H and non-heated sample section d_{error}

The height of both samples H is equal to 0.150 m, with only a small uncertainty of 0.001 m to account for manufacturing discrepancies. The parameter d_{error} is used to compensate for the thermal expansion of the top parts of both samples, which might not have been subjected to the temperature change ΔT during the experiment, since the samples are not fully submerged. When assuming that the heat is perfectly conducted throughout the sample, a d_{error} of zero should be used and the entire height of the sample H is thus subjected to the temperature change. The water level has been filled approximately 0.02 m, but certainly not more than 0.04 m, below the top surface of the samples. In the worst case, the water level is 0.04 m below the top surface of the samples and the entire section protruding above the water is not subjected to the temperature change. In practise, the height of the section which is not subjected to the temperature change will lie between the presented best and worst case scenario and is therefore chosen as $d_{\text{error}} = (0.02 \pm 0.02)$ m.

Difference between the change in both sensor gaps G

The average value of the difference between the change in both sensor gaps, for the final time step of the performed measurements at which $\Delta T = -10\,^{\circ}\text{C}$, is equal to -26×10^{-6} m. The uncertainty of the difference between the change in both sensor gaps is a result of both the uncertainty for the mean of the measured values and the uncertainty resulting from the instabilities of the measurement setup.

Since only four measurements are performed, a Student's t-distribution is used estimate the probable error of the mean [96]. Using the Student's t-distribution, the mean can be expressed as $\overline{x} \pm ks$, with $\overline{x}$ the sample mean and s the sample standard deviation:

$$s = \sqrt{\sum_{i=1}^{n} \frac{(x_i - \overline{x})^2}{n-1}}. \tag{F-13}$$

For four measurements, a k of 3.182 should be used for a 95 % confidence interval [97]. Using the presented expression for the standard deviation, a mean of $(-26 \pm 6) \times 10^{-6}$ m is obtained, in which the uncertainty for the mean is determined based on a 95 % confidence interval.

Additionally, an uncertainty due to setup instabilities observed in the verification measurements presented in E-8, should be accounted for. The instabilities result in a maximum difference between the change in both sensor gaps of approximately 5×10^{-6} m for measurement which took one hour or less, where zero difference is expected. The measurement 'M1 - 02/15/2021' is ignored, since the sensors might not have been fastened sufficiently. Since the actual measurements take at least twice as long as the verification measurements, the uncertainty due to the measurement instabilities is estimated as 10×10^{-6} m.

Both uncertainties, indicated with δG_1 and δG_2, are combined using the root sum of squares:

$$\delta G = \sqrt{(\delta G_1)^2 + (\delta G_2)^2}, \tag{F-14}$$

which gives a combined uncertainty for the difference between the change in the sensor gaps of $\delta G = 12 \times 10^{-6}$ m.

Results

The unidirectional thermal expansion of the optimized sample is obtained using Eq. (F-11). The uncertainty of the determined unidirectional thermal expansion is computed using Eq. (F-12). Inserting the values presented in the previous section, gives an unidirectional thermal expansion of the optimized sample equal to $\alpha_{\text{opt}} = (-4 \pm 8)\,\mu\text{m}/(\text{m}^\circ\text{C})$.

Appendix G

Research Paper

A scientific paper has been written based on the work conducted in this thesis, titled "Topology Optimization for Manufacturable Thermoelastic Metamaterials with Tailored Unidirectional Thermal Expansion". The following twelve pages present this paper, which will be submitted to *11th Int. Conference on Coupled Problems in Science and Engineering (COUPLED 2021)*. The website of this conference, from which the conference proceedings can be downloaded, can be visited using the following url: https://congress.cimne.com/Coupled2021/frontal/default.asp. The thesis report uploaded to the TU Delft repository does not include the scientific paper for copyright reasons.

References

[1] Y. Liu and X. Zhang, "Metamaterials: A new frontier of science and technology," *Chemical Society Reviews*, vol. 40, no. 5, pp. 2494–2507, 2011.

[2] J. U. Surjadi, L. Gao, H. Du, X. Li, X. Xiong, N. X. Fang, and Y. Lu, "Mechanical metamaterials and their engineering applications," *Advanced Engineering Materials*, vol. 21, no. 3, p. 1800864, 2019.

[3] C. M. Spadaccini, "Mechanical Metamaterials: Design , Fabrication , and Performance," in *Fronteers of Engineering: Report on leading-edge engineering from the 2015 symposium*. Washington, DC: The National Academies Press, 2016, pp. 85–96.

[4] R. Lakes, "Foam structures with a negative Poisson's ratio," *Science*, vol. 235, no. 4792, pp. 1038–1040, 1987.

[5] O. Sigmund and S. Torquato, "Design of materials with extreme thermal expansion using a three-phase topology optimization method," *Journal of the Mechanics and Physics of Solids*, vol. 45, no. 6, pp. 1037–1067, 1997.

[6] R. S. Lakes, T. Lee, A. Bersie, and Y. C. Wang, "Extreme damping in composite materials with negative-stiffness inclusions," *Nature*, vol. 410, no. 6828, pp. 565–567, 2001.

[7] T. A. Schaedler, A. J. Jacobsen, A. Torrents, A. E. Sorensen, J. Lian, J. R. Greer, L. Valdevit, and W. B. Carter, "Ultralight metallic microlattices," *Science*, vol. 334, no. 6058, pp. 962–965, 2011.

[8] J. Bauer, S. Hengsbach, I. Tesari, R. Schwaiger, and O. Kraft, "High-strength cellular ceramic composites with 3D microarchitecture," in *Proceedings of the National Academy of Sciences of the United States of America*, vol. 111, no. 7, 2014, pp. 2453–2458.

[9] E. Andreassen, B. S. Lazarov, and O. Sigmund, "Design of manufacturable 3D extremal elastic microstructure," *Mechanics of Materials*, vol. 69, no. 1, pp. 1–10, 2014.

[10] Y. C. Zhang, Y. J. Liang, S. T. Liu, and Y. D. Su, "A new design of dual-constituent triangular lattice metamaterial with unbounded thermal expansion," *Acta Mechanica Sinica*, vol. 35, no. 3, pp. 507–517, 2019.

[11] A. Takezawa and M. Kobashi, "Design methodology for porous composites with tunable thermal expansion produced by multi-material topology optimization and additive manufacturing," *Composites Part B*, vol. 131, pp. 21–29, 2017.

[12] A. W. Sleight, "Isotropic negative thermal expansion," *Annual Review of Materials Research*, vol. 28, no. 1, pp. 29–43, 1998.

[13] Y. Xie, X. Pei, and J. Yu, "Double-layer sandwich annulus with ultra-low thermal expansion," *Composite Structures*, vol. 203, pp. 709–717, 2018.

[14] H. Xu and D. Pasini, "Structurally efficient three-dimensional metamaterials with controllable thermal expansion," *Scientific Reports*, vol. 6, pp. 34 924 – 34 932, 2016.

[15] X. Wu, Y. Su, and J. Shi, "Perspective of additive manufacturing for metamaterials development," *Smart Materials and Structures*, vol. 28, no. 9, p. 093001, 2019.

[16] M. Bendsøe and O. Sigmund, *Topology Optimization: Theoy, Methods and Applications*. Berlin: Springer-Verlag, 2003.

[17] M. Langelaar, "An additive manufacturing filter for topology optimization of print-ready designs," *Structural and Multidisciplinary Optimization*, vol. 55, no. 3, pp. 871–883, 2017.

[18] R. Lakes, "Cellular solid structures with unbounded thermal expansion," *Journal of Materials Science Letters*, vol. 15, no. 6, pp. 475–477, 1996.

[19] G. Blokland, "Topology Optimization of Metamaterials," Literature survey, Precision and Microsystems Engineering, Technical Univesity of Delft, Delft, 2019.

[20] J. A. Gallego and J. Herder, "Synthesis methods in compliant mechanisms: An overview," in *International Design Engineering Technical Conferences Computers and Information in Engineering Conference*, vol. 7, 2009, pp. 193–214.

[21] R. A. Schapery, "Thermal expansion coefficients of composite materials based on energy principles," *Journal composite materials*, vol. 2, no. 3, pp. 380–404, 1968.

[22] B. W. Rosen and Z. Hashin, "Effective thermal expansion coefficients and specific heats of composite materials," *International Journal of Engineering Science*, vol. 8, no. 2, pp. 157–173, 1970.

[23] L. V. Gibiansky and S. Torquato, "Thermal expansion of isotropic multiphase composites and polycrystals," *Journal of the Mechanics and Physics of Solids*, vol. 45, no. 7, pp. 1223–1252, 1997.

[24] S. Watts and D. A. Tortorelli, "Optimality of thermal expansion bounds in three dimensions," *Extreme Mechanics Letters*, vol. 12, pp. 97–100, 2017.

[25] O. Sigmund and S. Torquato, "Composites with extremal thermal expansion coefficients," *Applied Physics Letters*, vol. 69, no. 21, pp. 3203–3205, 1996.

[26] B. C. Chen, E. C. Silva, and N. Kikuchi, "Advances in computational design and optimization with application to MEMS," *International Journal for Numerical Methods in Engineering*, vol. 52, no. 1-2, pp. 23–62, 2001.

[27] A. Takezawa, M. Kobashi, and M. Kitamura, "Porous composite with negative thermal expansion obtained by photopolymer additive manufacturing," *APL Materials*, vol. 3, no. 7, 2015.

[28] E. Andreassen, J. J. Sondergaard, O. Sigmund, and T. J. Juel, "Optimal design of porous materials," Ph.D. dissertation, Department of Mechanical Engineering, DTU, Lyngby, 2015.

[29] X. Wang, Y. Mei, and M. Y. Wang, "Level-set method for design of multi-phase elastic and thermoelastic materials," *International Journal of Mechanics and Materials in Design*, vol. 1, no. 3, pp. 213–239, 2004.

[30] Y. Wang, Z. Luo, N. Zhang, and T. Wu, "Topological design for mechanical metamaterials using a multiphase level set method," *Structural and Multidisciplinary Optimization*, vol. 54, no. 4, pp. 937–952, 2016.

[31] M. Hirota and Y. Kanno, "Optimal design of periodic frame structures with negative thermal expansion via mixed integer programming," *Optimization and Engineering*, vol. 16, no. 4, pp. 767–809, 2015.

[32] L. Ai and X. L. Gao, "Three-dimensional metamaterials with a negative Poisson's ratio and a non-positive coefficient of thermal expansion," *International Journal of Mechanical Sciences*, vol. 135, pp. 101–113, 2018.

[33] T. Lim, "Anisotropic and negative thermal expansion behavior in a cellular microstructure," *Journal of Materials Science*, vol. 40, no. 12, pp. 3275–3277, 2005.

[34] G. Jefferson, T. A. Parthasarathy, and R. J. Kerans, "Tailorable thermal expansion hybrid structures," *International Journal of Solids and Structures*, vol. 46, no. 11-12, pp. 2372–2387, 2009.

[35] J. B. Hopkins, K. J. Lange, and C. M. Spadaccini, "Designing microstructural architectures with thermally actuated properties using freedom, actuation, and constraint topologies," *Journal of Mechanical Design*, vol. 135, no. 6, p. 061004, 2013.

[36] J. B. Hopkins, Y. Song, H. Lee, N. X. Fang, and C. M. Spadaccini, "Polytope sector-based synthesis and analysis of microstructural architectures with tunable thermal conductivity and expansion," *Journal of Mechanical Design*, vol. 138, no. 5, p. 051401, 2016.

[37] K. Wei, H. Chen, Y. Pei, and D. Fang, "Planar lattices with tailorable coefficient of thermal expansion and high stiffness based on dual-material triangle unit," *Journal of the Mechanics and Physics of Solids*, vol. 86, pp. 173–191, 2016.

[38] K. Wei, Y. Peng, Z. Qu, Y. Pei, and D. Fang, "A cellular metastructure incorporating coupled negative thermal expansion and negative Poisson's ratio," *International Journal of Solids and Structures*, vol. 150, pp. 255–267, 2018.

[39] L. Ai and X. L. Gao, "Metamaterials with negative Poisson's ratio and non-positive thermal expansion," *Composite Structures*, vol. 162, pp. 70–84, 2017.

[40] Z. H. Jin, "A microlattice material with negative or zero thermal expansion," *Composites Communications*, vol. 6, pp. 48–51, 2017.

[41] C. K. Ng, K. K. Saxena, R. Das, and E. I. Saavedra Flores, "On the anisotropic and negative thermal expansion from dual-material re-entrant-type cellular metamaterials," *Journal of Materials Science*, vol. 52, no. 2, pp. 899–912, 2017.

[42] R. Lakes, "Cellular solids with tunable positive or negative thermal expansion of unbounded magnitude," *Applied Physics Letters*, vol. 90, no. 22, 2007.

[43] C. S. Ha, E. Hestekin, J. Li, M. E. Plesha, and R. S. Lakes, "Controllable thermal expansion of large magnitude in chiral negative Poisson's ratio lattices," *Physica Status Solidi (B) Basic Research*, vol. 252, no. 7, pp. 1431–1434, 2015.

[44] C. S. Ha, M. E. Plesha, and R. S. Lakes, "Simulations of thermoelastic triangular cell lattices with bonded joints by finite element analysis," *Extreme Mechanics Letters*, vol. 12, no. 1, pp. 101–107, 2017.

[45] L. Wu, B. Li, and J. Zhou, "Isotropic negative thermal expansion metamaterials," *ACS Applied Materials and Interfaces*, vol. 8, no. 27, pp. 17 721–17 727, 2016.

[46] J. Qu, M. Kadic, A. Naber, and M. Wegener, "Micro-structured two-component 3D metamaterials with negative thermal-expansion coefficient from positive constituents," *Scientific Reports*, vol. 7, pp. 40 643–40 651, 2017.

[47] T. Lim, "2D metamaterial with in-plane positive and negative thermal expansion and thermal shearing based on interconnected alternating bimaterials," *Materials Research Express*, vol. 6, no. 11, p. 115804, 2019.

[48] N. M. Palumbo, C. W. Smith, W. Miller, and K. E. Evans, "Near-zero thermal expansivity 2-D lattice structures: Performance in terms of mass and mechanical properties," *Acta Materialia*, vol. 59, no. 6, pp. 2392–2403, 2011.

[49] L. Vandeperre, W. Clegg, and A. Howlett, "Application of negative thermal expansion to optical fibres," in *CIMTEC 2002: international conferences on modern materials and technologies*, Florence, 2002.

[50] L. J. Vandeperre and W. J. Clegg, "Tailoring strains through microstructural design," in *Materials Research Society Symposium - Proceedings*, vol. 785, 2004, pp. 389–394.

[51] J. N. Grima, P. S. Farrugia, R. Gatt, and V. Zammit, "A system with adjustable positive or negative thermal expansion," in *Proceedings of the Royal Society A: Mathematical, Physical and Engineering Sciences*, vol. 463, no. 2082, 2007, pp. 1585–1596.

[52] J. N. Grima, D. Attard, and R. Gatt, "Truss-type systems exhibiting negative compressibility," *Physica Status Solidi (B) Basic Research*, vol. 245, no. 11, pp. 2405–2414, 2008.

[53] W. Miller, D. S. Mackenzie, C. W. Smith, and K. E. Evans, "A generalised scale-independent mechanism for tailoring of thermal expansivity: Positive and negative," *Mechanics of Materials*, vol. 40, no. 4-5, pp. 351–361, 2008.

[54] C. A. Steeves, S. L. dos Santos e Lucato, M. He, E. Antinucci, J. W. Hutchinson, and

A. G. Evans, "Concepts for structurally robust materials that combine low thermal expansion with high stiffness," *Journal of the Mechanics and Physics of Solids*, vol. 55, no. 9, pp. 1803–1822, 2007.

[55] C. A. Steeves, C. Mercer, E. Antinucci, M. Y. He, and A. G. Evans, "Experimental investigation of the thermal properties of tailored expansion lattices," *International Journal of Mechanics and Materials in Design*, vol. 5, no. 2, pp. 195–202, 2009.

[56] M. M. Toropova and C. A. Steeves, "Bimaterial lattices with anisotropic thermal expansion," *Journal of Mechanics of Materials and Structures*, vol. 9, no. 2, pp. 227–244, 2014.

[57] M. M. Toropova and C. A. Steeves, "Adaptive bimaterial lattices to mitigate thermal expansion mismatch stresses in satellite structures," *Acta Astronautica*, vol. 113, pp. 132–141, 2015.

[58] J. Berger, C. Mercer, R. M. McMeeking, and A. G. Evans, "The design of bonded bimaterial lattices that combine low thermal expansion with high stiffness," *Journal of the American Ceramic Society*, vol. 94, no. 1, pp. 42–54, 2011.

[59] T. Lim, "Negative thermal expansion structures constructed from positive thermal expansion trusses," *Journal of Materials Science*, vol. 47, no. 1, pp. 368–373, 2012.

[60] T. Lim, "Negative thermal expansion in transversely isotropic space frame trusses," *Physica Status Solidi (B) Basic Research*, vol. 250, no. 10, pp. 2062–2069, 2013.

[61] K. Wei, Y. Peng, W. Wen, Y. Pei, and D. Fang, "Tailorable thermal expansion of lightweight and robust dual-constituent triangular lattice material," *Journal of Applied Mechanics*, vol. 84, no. 10, pp. 101 006–101 015, 2017.

[62] K. Wei, Y. Peng, K. Wang, S. Duan, X. Yang, and W. Wen, "Three dimensional lightweight lattice structures with large positive, zero and negative thermal expansion," *Composite Structures*, vol. 188, pp. 287–296, 2018.

[63] J. Lehman and R. Lakes, "Stiff lattices with zero thermal expansion," *Journal of Intelligent Material Systems and Structures*, vol. 23, no. 11, pp. 1263–1268, 2012.

[64] J. Lehman and R. Lakes, "Stiff, strong zero thermal expansion lattices via the Poisson effect," *Journal of Materials Research*, vol. 28, no. 17, pp. 2499–2508, 2013.

[65] J. Lehman and R. Lakes, "Stiff lattices with zero thermal expansion and enhanced stiffness via rib cross section optimization," *International Journal of Mechanics and Materials in Design*, vol. 9, no. 3, pp. 213–225, 2013.

[66] J. Lehman and R. S. Lakes, "Stiff, strong, zero thermal expansion lattices via material hierarchy," *Composite Structures*, vol. 107, pp. 654–663, 2014.

[67] E. Gdoutos, A. A. Shapiro, and C. Daraio, "Thin and thermally stable periodic metastructures," *Experimental Mechanics*, vol. 53, no. 9, pp. 1735–1742, 2013.

[68] N. Yamamoto, E. Gdoutos, R. Toda, V. White, H. Manohara, and C. Daraio, "Thin films with ultra-low thermal expansion," *Advanced Materials*, vol. 26, no. 19, pp. 3076–3080, 2014.

[69] E. M. Parsons, "Lightweight cellular metal composites with zero and tunable thermal expansion enabled by ultrasonic additive manufacturing: Modeling, manufacturing, and testing," *Composite Structures*, vol. 223, p. 110656, 2019.

[70] A. Bensoussan, J. L. Lions, and G. Papanicolaou, *Asymptotic Analysis for Periodic Structures*. Amsterdam: North-Holland Publishing Company, 1978.

[71] E. Sánchez-Palencia, *Non-homogeneous media and vibration theory*, ser. Lecture Notes in Physics. Berlin: Springer-Verlag, 1980.

[72] R. K. Oruganti, A. K. Ghosh, and J. Mazumder, "Thermal expansion behavior in fab-

ricated cellular structures," *Materials Science and Engineering A*, vol. 371, no. 1-2, pp. 24–34, 2004.

[73] J. Qi and J. W. Halloran, "Negative thermal expansion artificial material from iron-nickel alloys by oxide co-extrusion with reductive sintering," *Journal of Materials Science*, vol. 39, no. 13, pp. 4113–4118, 2004.

[74] F. Wang, B. S. Lazarov, and O. Sigmund, "On projection methods, convergence and robust formulations in topology optimization," *Structural and Multidisciplinary Optimization*, vol. 43, no. 6, pp. 767–784, 2011.

[75] A. Bandyopadhyay and B. Heer, "Additive manufacturing of multi-material structures," *Materials Science and Engineering R: Reports*, vol. 129, pp. 1–16, 2018.

[76] M. Miedzinski, "Materials for additive manufacturing by direct energy deposition," M.S. Thesis, Department of Materials and Manufacturing, Chalmers University of Technology, Gotenburg, 2017.

[77] Sciaky Inc, "Benefits of wire vs. powder metal 3d printing," Accessed on: Feb. 26, 2021. [Online]. Available: https://www.sciaky.com/additive-manufacturing/wire-vs-powder

[78] T. DebRoy, H. L. Wei, J. S. Zuback, T. Mukherjee, J. W. Elmer, J. O. Milewski, A. M. Beese, A. Wilson-Heid, A. De, and W. Zhang, "Additive manufacturing of metallic components – Process, structure and properties," *Progress in Materials Science*, vol. 92, pp. 112–224, 2018.

[79] K. Sojiphan, M. R. Sriraman, and S. S. Babu, "Stability of microstructure in Al3003 builds made by very high power ultrasonic additive manufacturing," in *21st Annual International Solid Freeform Fabrication Symposium – An Additive Manufacturing Conference*, 2010, pp. 362–371.

[80] Fabrisonic, "Soniclayer 7200 uam machine," Accessed on: Feb. 26, 2021. [Online]. Available: https://fabrisonic.com/3dprinting/wp-content/uploads/2018/04/soniclayer-7200.pdf

[81] Fabrisonic, "Fabrisonic's 3d metal printing design guide and frequently asked questions," Accessed on: Feb. 26, 2021. [Online]. Available: https://fabrisonic.com/3dprinting/wp-content/uploads/2018/03/FAQ-Design-Guide_S.pdf

[82] Fabrisonic, "How it works...fabrisonic's 3d printing technology," Accessed on: Feb. 26, 2021. [Online]. Available: https://fabrisonic.com/fabrication/wp-content/uploads/2016/03/How-it-works-inforgraphic-WEB.pdf

[83] Y. Zhang, L. Wu, X. Guo, S. Kane, Y. Deng, Y. G. Jung, J. H. Lee, and J. Zhang, "Additive manufacturing of metallic materials: A review," *Journal of Materials Engineering and Performance*, vol. 27, no. 1, pp. 1–13, 2018.

[84] K. Qiu, W. Zhang, M. Domaszewski, and D. Chamoret, "Topology optimization of periodic cellular solids based on a superelement method," *Engineering Optimization*, vol. 41, no. 3, pp. 225–239, 2009.

[85] E. Andreassen and C. S. Andreasen, "How to determine composite material properties using numerical homogenization," *Computational Materials Science*, vol. 83, pp. 488–495, 2014.

[86] R. J. Guyan, "Reduction of stiffness and mass matrices," *AIAA Journal*, vol. 3, no. 2, p. 380, 1965.

[87] O. Sigmund, "Manufacturing tolerant topology optimization," *Acta Mechanica Sinica/Lixue Xuebao*, vol. 25, no. 2, pp. 227–239, 2009.

[88] T. E. Bruns and D. A. Tortorelli, "Topology optimization of non-linear elastic structures and compliant mechanisms," *Computer Methods in Applied Mechanics and Engineering*,

vol. 190, no. 26-27, pp. 3443–3459, 2001.

[89] X. Qian and O. Sigmund, "Topological design of electromechanical actuators with robustness toward over- and under-etching," *Computer Methods in Applied Mechanics and Engineering*, vol. 253, pp. 237–251, 2013.

[90] K. Svanberg, "The method of moving asymptotes - a new method for structural optimization." *International Journal for Numerical Methods in Engineering.*, vol. 24, no. 2, pp. 359–373, 1987.

[91] K. Svanberg, "The Method of Moving Asymptotes - Modelling aspects and solution schemes," 1998. [Online]. Available: http://www.ingveh.ulg.ac.be/uploads/education/meca-0027-1/MMA_DCAMM_1998.pdf

[92] L. Xia and P. Breitkopf, "Design of materials using topology optimization and energy-based homogenization approach in Matlab," *Structural and Multidisciplinary Optimization*, vol. 52, no. 6, pp. 1229–1241, 2015.

[93] M. Langelaar, "Topology optimization of 3D self-supporting structures for additive manufacturing," *Additive Manufacturing*, vol. 12, pp. 60–70, 2016.

[94] E. Abbe, "Messapparate für physiker," *Zeitschrift für Instrumentenkunde*, vol. 10, 1890.

[95] H. Ku, "Notes on the use of propagation of error formulas," *Journal of Research of the National Bureau of Standards, Section C: Engineering and Instrumentation*, vol. 70C, no. 4, p. 263, 1966.

[96] Student, "The Probable Error of a Mean," *Biometrika*, vol. 6, no. 1, pp. 1–25, 1908.

[97] W. H. Beyer, *Handbook of Tables for Probability and Statistics 2nd Edition.* CRC Press, 2017.